Performance Prediction of Cavitating Hydrofoil Sections using CFD
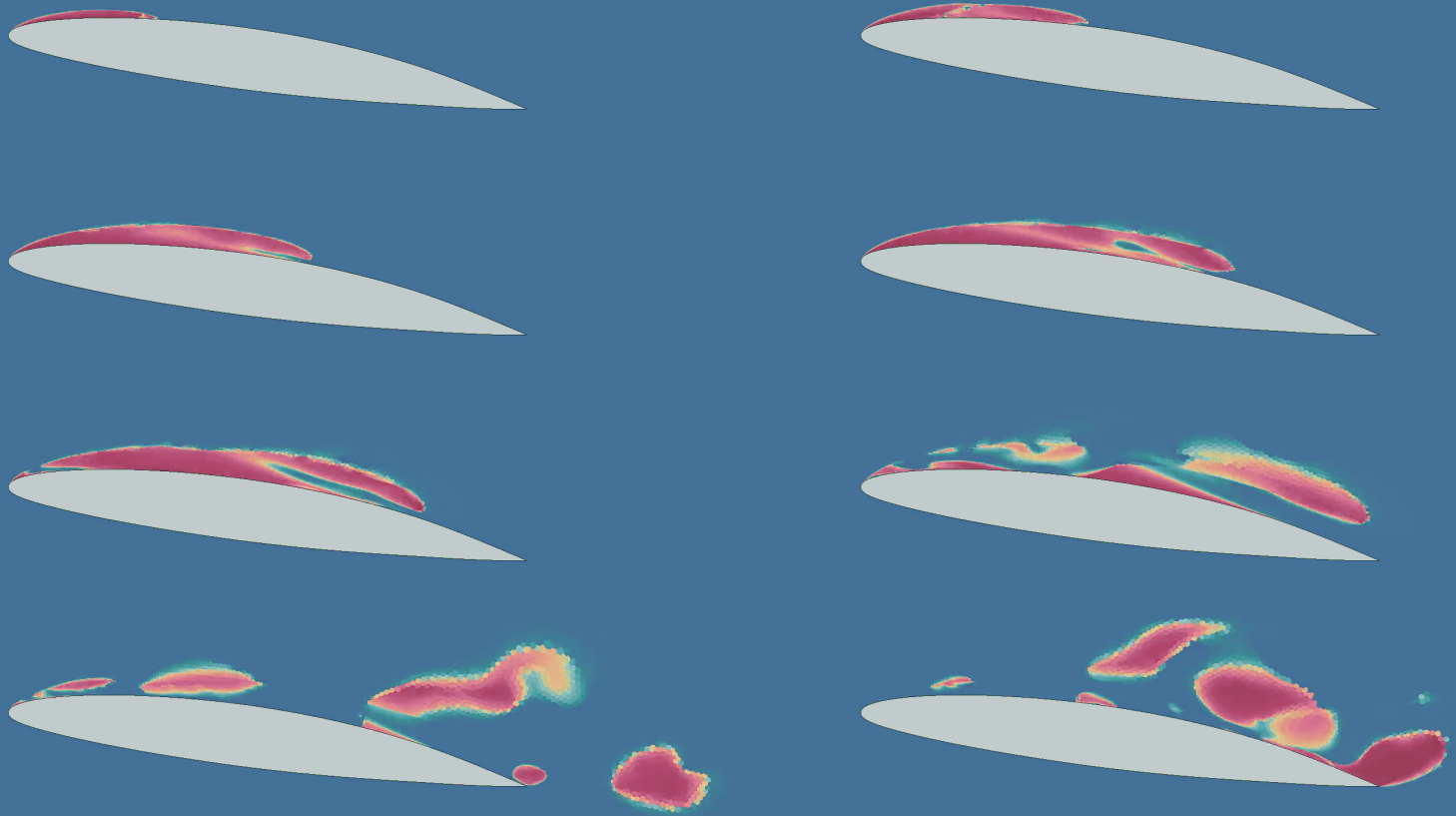
Msc Thesis Aerospace Engineering
Cyril Delaporte

Delft University of Technology

TUDelft

VPLP design

Performance Prediction of Cavitating Hydrofoil Sections using CFD

by

Cyril Delaporte

to obtain the degree of Master of Science
at the Delft University of Technology,
to be defended publicly on 30 August 2023 at 9:00.

An electronic version of this thesis is available at `http://repository.tudelft.nl/`.

T̃UDelft   **VPLP**_{design}

Abstract

Hydrofoils can under certain circumstances cause a phase change from liquid water to water vapor. This phenomenon is called cavitation and is caused by the low pressure over the hydrofoil when the vessel exceeds a certain velocity though the water. Cavitation can take different forms depending the angle of attack α and the flow conditions which are characterized with the cavitation number σ. The different types of cavitation can have different effects on flow and loads.

Computational Fluid Dynamics (CFD) is widely used in aero and hydrodynamic design, with (U)RANS most commonly used for CFD in the industry due to its relatively low computational cost while providing sufficiently accurate results. Cavitation models in URANS simulations need a multiphase framework in order to model the liquid/vapor interface of the cavitation bubbles. The Schnerr-Sauer cavitation model uses simplified bubble dynamics equations for relatively fast calculation while providing accurate results. In current project, a Volume of Fluid method is used the Schnerr-Sauer cavitation model is used with URANS CFD simulations to improve and enhance the behaviour and performance prediction of hydrofoils sections under cavitating conditions. Given the industrial context of this project, the simulations are conducted using constrained computational resources.

Validation is performed for a non-cavitating test case using a NACA-0012 section, followed by validation for a cavitating test case using a modified NACA-66 section. Mesh convergence studies have been performed, turbulence models have been compared and the turbulent viscosity has been modified. The final set-up uses the SST turbulence model with a modified turbulent viscosity exponent $n = 2.3$.

To assess the flow behavior and hydrofoil section performance under cavitating conditions, a comparison is made in CFD using cavitation models, relative to the current practice. This study shows that the lift and drag results for a simulation without cavitation model are underestimated compared to the simulation with cavitation model in conditions of stable cavitation. For conditions with unstable cavitation, strong unsteady disturbed flow and loads are found that are not captured by the simulation without cavitation model.

The transition from stable to unstable cavitation is studied by investigating cavitation bubble length and its corresponding fluctuation as a function of the stability parameter $p_s = \frac{\sigma}{2(\alpha - \alpha_0)}$. The conditions found for the transition from stable to unstable cavitation are consistent with reference value at about $p_s = 4$. The inception of stable cavitation is found at about $p_s = 7$ which is considered to be more optimized to delay the formation of cavitation compared to $p_s = 8.5$ for experimental observations on the NACA-0015.

The lift, drag and performance polars are studied for several values of σ. The lift and drag polars for lower σ, i.e. higher cavitation rate, show a stronger increase in both lift and drag for stable cavitation cases. The performance (or Lift over Drag) is slightly increased at $\alpha = 4°$ for $\sigma = 1.2$ and 1. For higher angles of attack, the increase in drag surpasses the increase in lift and the performance decreases. These finding only hold the stable cavitation cases ($\alpha < 8°$ for all tested σ, and $\alpha = 6°$ for $\sigma = 1$) since the unstable cavitation results are inconclusive.

The main limitation of the set-up developed in current project is that the predictions in cloud cavitation show significant discrepancies in capturing the unstable shedding characteristics with respect to the reference data. As a result, the cloud cavitation shedding frequency is not accurately captured, resulting in an inadequate representation of vibrations and loading due to cloud cavitation.

Contents

List of Figures

List of Tables

<div align="right">

1

</div>

Introduction

1.1. Background

Hydrofoils are lifting surfaces attached to waterborne vessels. Similar to the wings of an airplane, hydrofoils (or simply foils) generate a lifting force as the vessel increases speed due to the flow of the water around the foil. This force lifts the hull out of the water, reducing or eliminating the hull's contact with the water reducing drag, and further increasing speed and efficiency. Rising out of the water using hydrofoils is often referred to as foiling.

During the second half of the 20th century, extensive development of hydrofoil vessels was carried out by the USA and the Soviet Union. These developments were mainly for the purpose of making commercial passenger ships and military vessels [26] [40]. More recently, hydrofoils have been used in water sports and major sailing competitions like America's Cup since 2013. The America's Cup design teams have helped to integrate the use of more modern design methods such as Vortex Lattice Method (VLM), RANS Computational Fluid Dynamics (CFD) and Fluid-Structure Interaction (FSI) into high performance sailing [30] [11]. Standardizing these tools within the field of sailing has contributed to the increase of use of hydrofoils in water sports in general and has led, for example, to the inclusion of foiling disciplines in the Olympic Games [33] [23].

VPLP Design is a naval architecture firm renowned for many award-winning and revolutionary boat designs. They have been involved in America's Cup campaigns, record-breaking Ultime Trimaran designs and many other renowned projects in the sailing world. VPLP's racing division brings together naval architects, structural and performance engineers to create fast and efficient boats using tools such as VLM, CFD and FSI.

Figure 1.1: 36th America's Cup Team Luna Rossa Prada Pirelli foiling at high speed [Photo: Studio Borlenghi].

Unlike aeroplane wings, hydrofoils operate under water, which can cause complications under certain condi-tions. A phenomenon called cavitation occurs when hydrofoils exceed a certain speed, causing the water around the foil to form vapour bubbles that disrupt the flow around the foil and can cause damage when it collapses. Cavitation can take different forms depending on the angle of attack and the cavitation number (details of the physics of the phenomenon are given in the section 2.1). Incipient cavitation takes the form of small bubbles which convect with the flow and have little effect on the flow and foil performance. As cavitation increases due to an increase in velocity or a decrease in ambient pressure, a fixed cavitation bubble forms at the leading edge of the foil, changing the flow around the foil. This has been shown to alter foil performance [20] [18]. Increasing the cavitation rate further leads to an unsteady form of cavitation in which bubbles are periodically formed and shedded. This is called cloud cavitation and has been shown to cause vibration and erosion on propeller blades [44] [45] [24]. The surface erosion caused by the collapse of the cavitation bubbles is an active area of research and is particularly relevant to ship propellers, pumps and tidal stream turbines [42] [8]. These types of cavitation have negative effects and are best avoided or mitigated. If the rate of cavitation is further increased, a state of supercavitation can be achieved. Supercavitation can have beneficial effects in certain applications, such as the operation of torpedoes [2] [3] .

Figure 1.2: Cavitation at the tip of the blades and in the trailing vortices in the wake of a propeller in a water tunnel experiment at the David Taylor Model Basin [28].

In hydrofoil design, low fidelity tools such as VLM or panel methods are often used in the early stages of design where many design configurations and operating conditions are tested. Such tools are based on potential flow theory and perform inviscid linearised flow calculations, giving a rough qualitative overview of the aero/hy-drodynamic performance [17]. For many industrial applications, potential flow methods do not give sufficiently accurate results. For these cases other methods must be sought. Computational Fluid Dynamics (CFD) can pro-vide high fidelity results that have been shown to be consistent with experimental results and real life applications. CFD methods calculate the Navier-Stokes equations on a discretised computational domain. There are three main frameworks within CFD; Direct Numerical Simulations (DNS) solve the full range of spatial and temporal scales, requiring a large amount of computational resources. Large Eddy Simulations (LES) partially model the smallest length scales using filters, which significantly reduces the overall computational cost compared to DNS, although it still requires significant computational resources for most practical applications. Finally, (unsteady) Reynolds Averaged Navier-Stokes (RANS, or URANS for unsteady RANS) fully models the smallest length scale using averaged Navier-Stokes equations, resulting in the Reynolds stress term to be modelled. RANS requires the least computing power and is most commonly used in industrial applications.

One of the key quantities studied in the design of hydrofoil geometry using these numerical tools is the pres-sure distribution over the geometry. The forces on the geometry are derived from this pressure field. Knowing that cavitation occurs when the pressure falls below a certain critical pressure, it is reasonable to assume that

where the pressure distribution falls below this critical pressure, cavitation is likely to occur. However, the actual formation of cavitation bubbles is not captured in typical hydrodynamic potential flow or CFD simulations. Because of the flow disturbances due to the formation of cavitation bubbles, relying solely on a simulation that neglects the cavitation phenomenon will not accurately depict a cavitating flow. This potentially means that such a result may not capture the correct loading acting on the studied geometry. In order to account for real cases of cavitating flow, these numerical methods require some additional attention.

In early work on cavitation modelling, Tulin and Wu used linearized theory to calculate the drag analytically on steady, two dimensional cavity flows about slender bodies [39] [43]. Acosta and Watanabe extended this work for steady and unsteady partial cavities respectively and found an analytical relation between the cavity length, cavitation number and angle of attack of the hydrofoil [1] [41]. Moreover, potential flow solvers which consider cavitation have been developed using boundary element methods [5] [6] [7]. However these methods are still restricted within the assumptions of potential flow theory and only obtain low fidelity results.

In order to implement a cavitation model in CFD methods like (U)RANS or LES, a Volume of Fluid (VOF) multiphase simulation must be used in order to track the water/vapor interface [14]. For this, bubble dynamics equations known as the Rayleigh-Plesset Equations [29] need to be calculated in order for the cavitating flow to be solved. Several different different cavitation models have been proposed with models solving more or fewer terms in the Rayleigh-Plesset Equations and thus require less or more computing power. The Schnerr-Sauer cavitation model simplifies the original Rayleig-Plesset equation by eliminating several terms which makes it computationally relatively inexpensive. Still, using this cavitation model in URANS CFD simulations has shown to obtain robust simulations with accurate results [22].

For VPLP Design, it is important to keep innovating in order to remain competitive. One of the biggest obstacles to improving the top speed of foiling sailing vessels is cavitation. It is therefore important to evaluate the current methods of cavitation analysis and to incorporate the current state of the art knowledge and methods to the analysis of cavitating flows around hydrofoils. By enabling the prediction of cavitation, this will grant an advantage in hydrofoil design, ultimately leading to a methodology for optimizing hydrofoil geometry under cavitating conditions.

The operating conditions of fast foiling sailing vessels with a velocity up to about 50 $knts$ or about 26 m/s, with angles of attack up to about 8 degrees. Thus, these conditions should therefore be considered and studied. Moreover, as a company operating in the industry, VPLP must take into account the computational power and calculation time at their disposal. These restrictions should therefore also be taken into account in the choices of the models used. For these reasons, implementing the Schnerr-Sauer cavitation model in a URANS CFD simulation will be the starting point of this study.

1.2. Research Objectives

The main objective of this MSc Thesis Project is stated as follows:

> ***Assessment of using CFD to improve analysis and performance prediction of cavitating hydrofoil sections within an industrial setting, compared to current design practice.***

The cavitation analyses conducted and developed in this project are intended for industrial purposes, meaning the calculation time and processing power are limited. For the purpose of this project, the simulation time will be restricted to about 8 hours for a single run, and the total time for a series of simulations (e.g. polar plots) is limited to about 50 hours. These simulations will be conducted on a machine with about 20 CPU cores using a URANS solver from the commercial software Star-CCM+ and the Schnerr-Sauer cavitation model. Once the models have been implemented and the setup is validated and ready to be used, the following sub-questions will be addressed:

- *How do the results obtained from cavitation analysis on a hydrofoil section using a cavitation model compare with results obtained from analysis conducted without a cavitation model?*
- *How can the transition from stable to unstable cavitation on a hydrofoil section be predicted?*
- *How do the lift and drag coefficient and performance polars of a cavitating hydrofoil section depend on the cavitation number?*
- *What are the limitations of the final setup?*

1.3. Report Outline

This project consists of a section on the theory, the methodology, the results and a conclusion.

The theory chapter discusses the physics of cavitation and the equations that describe the bubble behavior. It also reviews CFD frameworks and the numerical models that are relevant for this project. Additionally, it discusses the analytical relation between the cavity length, cavitation number and angle of attack for a flat plate hydrofoil.

In the methodology, a suitable CFD framework and cavitation model will be chosen considering the frameworks presented in the Theory section and the restrictions stated in the research objectives. Next, the steps to perform a reliable and accurate CFD simulation are discussed. Furthermore, the geometry, operating conditions and experimental reference for the cases with and without cavitation are presented. These cases will be used to validate the model developed in this project. Moreover, a method comparison of cavitation analysis to evaluate the improvement the analysis. Also, a stability and polar analysis are proposed in order to study the performance of the cavitating hydrofoil sections.

The results chapter presents and discusses the results of the validation cases, analysis comparison, stability and polar studies.

The conclusion chapter summarizes the main findings and answers the research questions. It also includes some recommendations for further development.

2

Theory

In this chapter, the important physics of the cavitation phenomenon are discussed and the necessary equations are derived. Furthermore, a general overview of the CFD frameworks and numerical models is given. More emphasis and depth will go to the models relevant to the current study. The final section is dedicated to the linear theory concerning the relationship between operating conditions and cavity length.

2.1. Physics

The phase of a fluid is dependent on both temperature and pressure. Increasing the temperature of a liquid up to the boiling point will cause the liquid to vaporize. This phase change due to temperature is called boiling. Similarly, decreasing the pressure in a liquid up to a critical pressure, called the saturation vapor pressure, will cause the liquid to vaporize. This phenomenon is called cavitation. A phase diagram is shown in figure 2.1 where the phase of a liquid is shown as a function of temperature and pressure.
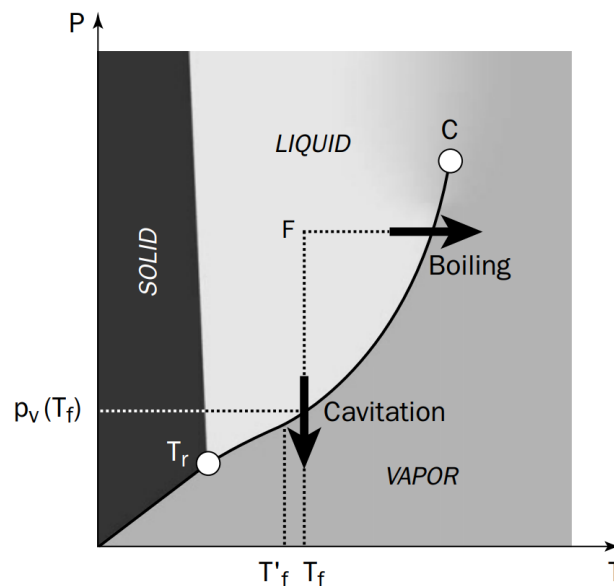
Figure 2.1: Phase Diagram [10]

Thus, cavitation occurs when the local static pressure falls below the saturation vapor pressure of the fluid which causes vapor bubbles to form in within the flow. Cavitation can come in different forms. It can come as transient isolated bubbles, as attached sheet cavities, cavitation vortices or even supercavitation [10]. The rate of cavitation is characterized using the cavitation number σ which is a dimensionless value defined as the difference between the local static pressure p and the saturation vapor pressure p_v divided by the dynamic pressure:

5

$$\sigma = \frac{p_\infty - p_v}{\frac{1}{2}\rho_l U_\infty^2}, \tag{2.1}$$

with liquid density ρ_l and free stream velocity U_∞.

In figure 2.2, the different cavitation regimes over a hydrofoil for increasing σ are illustrated [16]. In this illustration, it can be seen that for the highest value of σ for which cavitation occurs, it comes in the form of incipient bubbles which convect with the flow. As the value for σ decreases, by increasing the flow velocity or decreasing the ambient pressure, the cavitation comes in the form of a steady partial sheet cavity going from the leading edge of the foil to about half the chord length. As the cavitation number further decreases, cavitation comes in the form of unsteady partial cavitation sheets shedding off from the hydrofoil. This is also referred to as cloud cavitation. Decreasing σ further, the cavitation forms a large cavitation bubble encapsulating the whole suction side of the hydrofoil. This is referred to as supercavitation.
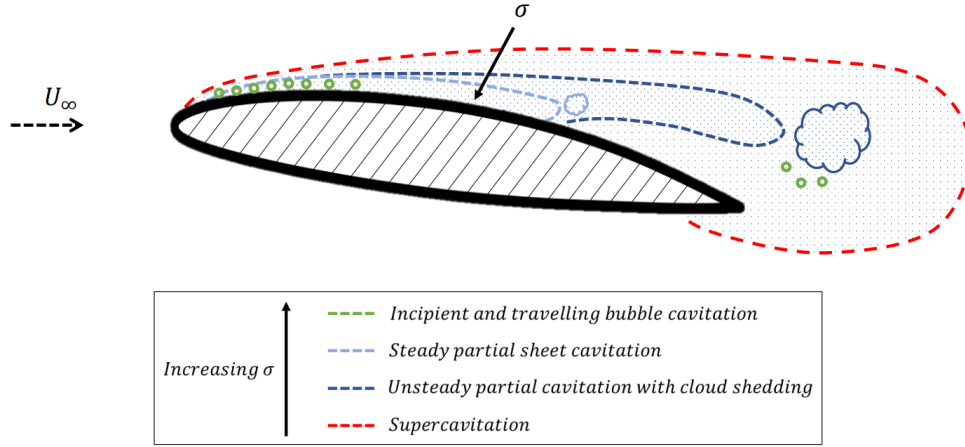
Figure 2.2: Cavitation Regimes for increasing σ [16].

2.1.1. Cavitation Nuclei

In order for cavitation to occur, apart from the pressure requirement, cavitation bubbles need a surface to nucleate on. This often comes in the form of impurities in the fluid. These small pre-existing bubbles in the fluid are called cavitation nuclei or seeds. The equilibrium state of these seeds require the following condition [10]:

$$p_\infty = p_g + p_v - \frac{2S}{R} \tag{2.2}$$

where p_g is the partial pressure, S the surface tension and R the bubble radius. Two mechanism are considered in the equation: (1) the internal pressure which increases the bubble radius, and (2) the surface tension, reducing the bubble radius. From this, we find the minimum bubble radius and pressure which are called the critical radius R_c and critical pressure p_c respectively:

$$R_c = R_0 \sqrt{\frac{3p_g R_0}{2S}} \tag{2.3}$$

$$p_c = p_v - \frac{4S}{3R_c} \tag{2.4}$$

with the initial bubble radius R_0.

When the minimum static pressure in the fluid falls below the vapor pressure, two scenarios have to be considered: $p_{min} > p_c$ and $p_{min} < p_c$. When $p_{min} > p_c$, the nucleus radius increases slightly and then returns to its initial radius. When $p_{min} < p_c$, the bubble becomes unstable and the bubble radius grows much larger than its initial size.

It is useful to consider the development of a bubble going though a Venturi nozzle for this unstable case. In figure 2.3 such a nozzle is illustrated with a seed going though it. The stages of development of the seed with

its associated pressure, surface tension and radius are depicted. While the seed is going though the throat of the nozzle, the pressure falls below the critical pressure p_c at which point the seed continues to grow while the pressure is already increasing. It grows until the local pressure has surpassed the vapor pressure, downstream from the throat, after which the bubble collapses.
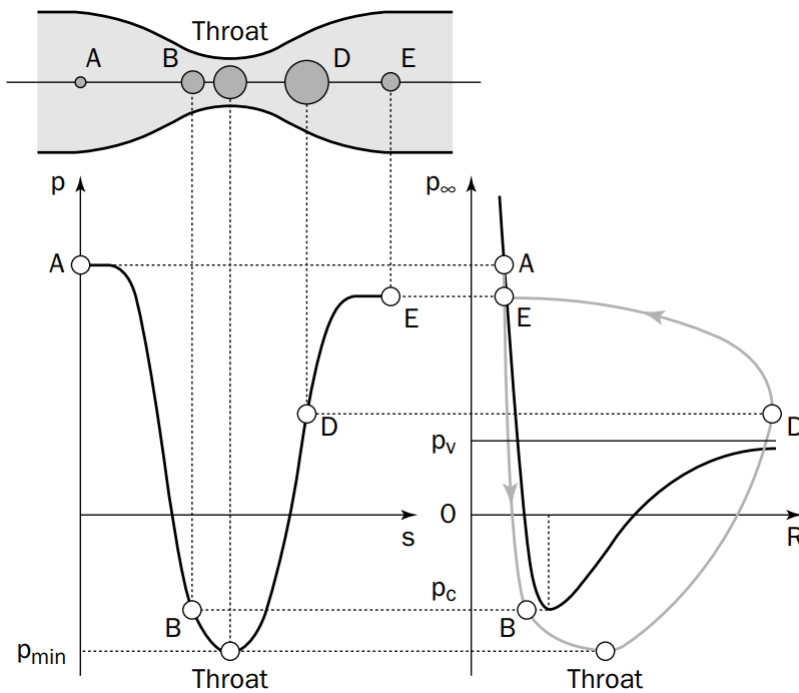
Figure 2.3: Unstable case ($p_{min} < p_c$) of a nucleus evolution in a Venturi nozzle[10].

The number of seeds, or the seed density, initially present in the fluid has an important influence on the response of the liquid to pressure variations and it is therefore important to measure this density in the fluid. The nucleus density is characterized the critical density p_c as show in figure 2.4. Figure 2.4 shows a measurement (dynamic measurement method) of the nuclei population as a function of the critical pressure minus the vapor pressure ($p_c - p_v$) with a fit though the measurement points.
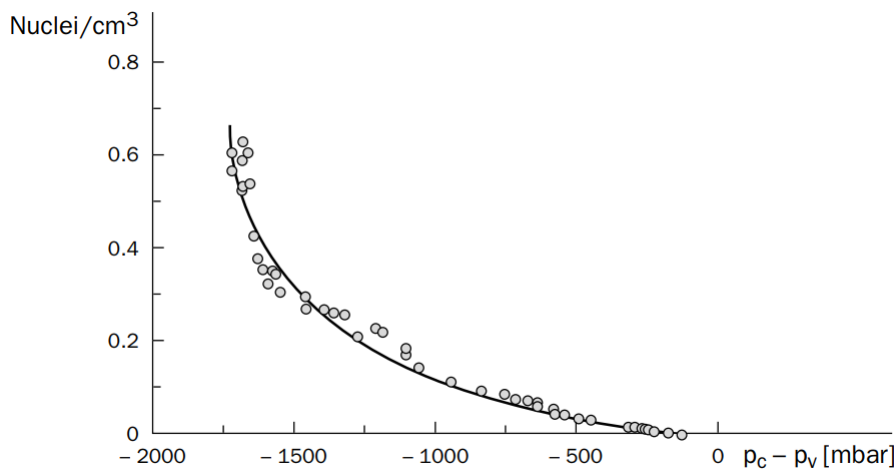
Figure 2.4: Typical histogram of nuclei population as a function of critical pressure (dynamic method of measurement) [10].

2.1.2. Rayleigh-Plesset Equation

One of the main equations in cavitation theory is the Rayleigh-Plesset equation which governs the dynamics of a bubble in a fluid. To derive this equation, consider a spherical bubble with time dependent radius $R(t)$ with a homogeneously distributed vapor and uniform pressure p_v. Moreover, an incompressible and either Newtonian or inviscid liquid is assumed and gravity is neglected [10].

Due to the pressure at the interface, kinematic viscosity μ and the surface tension S the normal stress at the bubble interface is found to be

$$\tau_{rr} = -p(R) + 2\mu \frac{\partial u}{\partial r}\bigg|_{r=R} + \frac{2S}{R}. \tag{2.5}$$

On the other hand from inside the bubble, the vapor pressure p_v and partial pressure p_g of the gas balance this out:

$$-\tau_{rr} = p_v + p_g. \tag{2.6}$$

Assuming an adiabatic transformation, the partial pressure is related to the initial pressure p_{g0} as follows:

$$p_g(t) = p_{g0} \left[\frac{R_0}{R(t)} \right]^{3\gamma}$$

with heat capacity ratio γ.

Using previous expressions, the pressure at the cavity interface can be written as follows:

$$p(R) = p_v + p_{g0} \left(\frac{R_0}{R} \right)^{3\gamma} - \frac{2S}{R} + 2\mu \frac{\partial u}{\partial r}\bigg|_{r=R} \tag{2.7}$$

The conservation laws of the fluid at the bubble interface are now analysed. Consider the flow at the bubble interface. From the continuity equation $\nabla \vec{u} = 0$ in spherical coordinates, the interface velocity gives

$$u(r,t) = \frac{R^2}{r^2} \dot{R}, \tag{2.8}$$

with $\dot{R} = \frac{dR}{dt}$. Now considering momentum conservation in spherical coordinates:

$$\rho_L \left(\frac{\partial u}{\partial t} + u \frac{\partial u}{\partial r} \right) = -\frac{\partial p}{\partial r} + \mu_L \left[\frac{1}{r^2} \frac{\partial}{\partial r} \left(r^2 \frac{\partial u}{\partial r} \right) - \frac{2u}{r^2} \right]. \tag{2.9}$$

The velocity in expression 2.8 is now substituted in the momentum equation (2.9), variables are separated and ∂p and ∂r are integrated from $r = R$ to $r \to \infty$. The viscous terms are cancelled out during substitution and we are left with:

$$\frac{p(R) - p_\infty}{\rho_L} = R \frac{d\dot{R}}{dt} + \frac{3}{2} \dot{R}^2 \tag{2.10}$$

The expressions for the pressure (2.7), velocity (2.8) and momentum (2.10) can be combined to obtain the general Rayleigh-Plesset Equation:

$$\rho \left[R\ddot{R} + \frac{3}{2} \dot{R}^2 \right] = p_v - p_\infty + p_{g0} \left(\frac{R_0}{R} \right)^{3\gamma} - \frac{2S}{R} - 4\mu \frac{\dot{R}}{R} \tag{2.11}$$

2.1.3. Bubble Collapse

With the Rayleigh-Plesset equation, some useful features of the vapor bubble can be described. In this section, the bubble collapse is analysed. For this, the viscosity, non-condensable gas and surface tension terms are neglected. Using these assumptions and rewriting the left hand side of the Rayleigh-Plesset equation 2.11 one obtains:

$$\frac{\rho}{2\dot{R}R^2}\frac{d}{dt}\left[\dot{R}^2R^3\right] = p_v - p_\infty \tag{2.12}$$

Integrating this expression yields:

$$\rho\dot{R}^2R^3 = \frac{2}{3}(p_v - p_\infty)(R^3 - R_0^3). \tag{2.13}$$

During collapse, the bubble radius velocity is negative. Thus the expression for velocity becomes:

$$\frac{dR}{dt} = -\sqrt{\frac{2}{3}\frac{p_\infty - p_v}{\rho}\left[\frac{R_0^3}{R^3} - 1\right]} \tag{2.14}$$

Separating variables and integration yields the characteristic collapse time:

$$\tau = \sqrt{\frac{3}{2}\frac{\rho}{p_\infty - p_v}}\int_0^{R_0}\frac{dR}{\sqrt{\frac{R_0^3}{R^3} - 1}} \tag{2.15}$$

Numerical integration of the expression radius velocity 2.14 allows the calculation of the radius $R(t)$ as a function of time. Figure 2.5 shows how the bubble radius tends to 0 during the characteristic collapse time while the radius velocity $|R(t)|$ asymptotically increases.
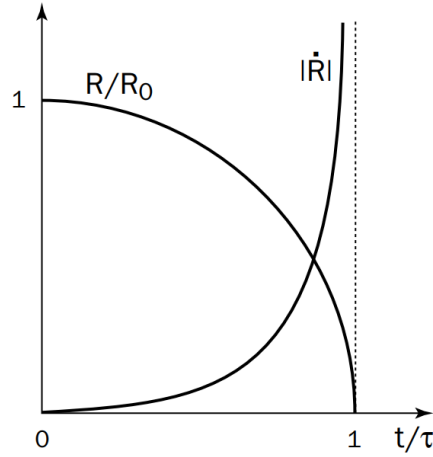
Figure 2.5: Evolution of bubble radius R and bubble radius velocity $\dot{R}$ during bubble collapse [10].

The value of τ is in good agreement with experimental results for a large range of initial bubble radii from about $1\,\mu m$ to about $1m$ [10]. For illustration, a water vapor bubble with an initial radius of $1\,cm$ collapses in approximately $1\,ms$ with an ambient pressure of $1\,bar$. Moreover, for a bubble radius of about $R/R_0 = 1/20$ one finds a radius velocity of about $|\dot{R}| \approx 720\,m/s$.

The high velocity values strongly indicate the need to consider compressibility during the final stages of collapse. Also note the fact that physical aspects such as the presence of non-condensable gas, the finite rate of vapor condensation, viscosity and surface pressure are not taken into account and will only slightly modify the bubble behaviour. Still, the Rayleigh-Plesset equations capture the main features of the bubble collapse process.

A Note on Surface Tension

When surface tension is taken into account, the bubble radius velocity (previously equation 2.14) becomes:

$$\frac{dR}{dt} = -\sqrt{\frac{2}{3}\frac{p_\infty - p_v}{\rho}\left[\frac{R_0^3}{R^3} - 1\right] + \frac{2}{\rho R_0}\frac{S}{R^3}\frac{R_0^3}{R^3}\left[1 - \frac{R^2}{R_0^2}\right]}.$$
(2.16)

The surface tension effects become non-negligible when the S term becomes relatively larger with respect to the pressure difference, yielding an expression for the initial bubble radius with significant surface tension effects:

$$\frac{2S}{\rho R_0} > \frac{2}{3}\frac{p_\infty - p_v}{\rho} \qquad \Rightarrow \qquad R_0 < \frac{3S}{p_\infty - p_v}$$
(2.17)

To put this in context, with a value of $S = 0.072\ N/m$ for water, assuming a pressure difference $(p_\infty - p_v) = 1\ bar$, surface tension effect will become significant for bubbles with an initial bubble radius of $R_0 = 2.2\ \mu m$. Values in this order of magnitude are exceptional in hydraulics.

2.1.4. Pressure Field

Before the integration over ∂r in expression 2.10 the momentum equation yields

$$\frac{p(r) - p_\infty}{\rho} = \ddot{R}\frac{R^2}{r} + 2\dot{R}^2\left[\frac{R}{r} - \frac{R^4}{4r^4}\right].$$
(2.18)

Having derived the bubble radius velocity from the *Rayleigh* model (expression 2.14), the bubble radius acceleration can also be calculated obtaining:

$$\ddot{R} = -\frac{p_\infty - p_v}{\rho}\frac{R_0^3}{R^4}.$$
(2.19)

Substituting the bubble velocity 2.14 and acceleration 2.19 in expression 2.18 we can obtain the non-dimensional pressure field $\Pi = \frac{p(r) - p_\infty}{p_\infty - p_v}$:

$$\Pi(r) = \frac{R}{3r}\left[\frac{R_0^3}{R^3} - 4\right] - \frac{R^4}{3r^4}\left[\frac{R_0^3}{R^3} - 1\right]$$
(2.20)
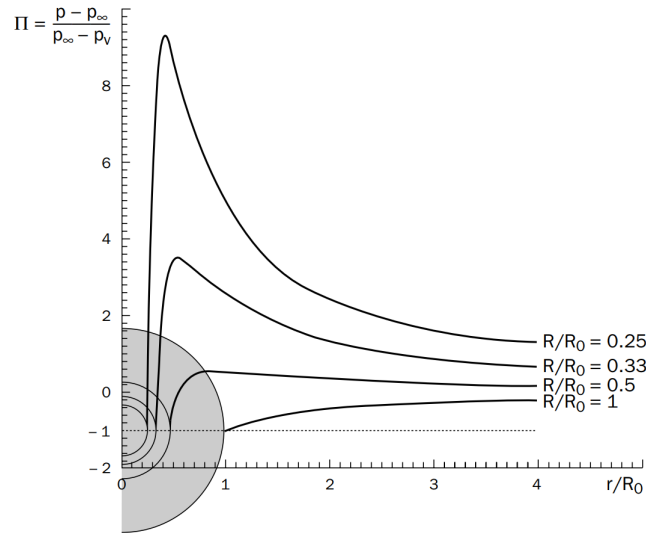
Figure 2.6: Evolution of the pressure field Π during bubble collapse [10].

In figure 2.6, the evolution of the pressure field is shown for several values of bubble radii. It can be seen that the pressure curve obtains an increasing peak as the bubble radius decreases. The pressure finds a maximum

in the fluid when the bubble radius becomes smaller than $R_0/\sqrt[3]{4} \approx 0.63\, R_0$. The maximum pressure Π_{max} then becomes:

$$\Pi_{\mathrm{max}} = \frac{p_{\mathrm{max}} - p_\infty}{p_\infty - p_v} = \frac{\left[\frac{R_0^3}{4R^3} - 1\right]^{4/3}}{\left[\frac{R_0^3}{R^3} - 1\right]^{1/3}}, \tag{2.21}$$

with the maximum pressure found at position:

$$\frac{r_{\mathrm{max}}}{R} = \left[\frac{\frac{R_0^3}{R^3} - 1}{\frac{R_0^3}{4R^3} - 1}\right]^{1/3} \tag{2.22}$$

During the bubble collapse, high pressures are found close to the bubble interface. For illustration, for a bubble radius $R/R_0 = 1/20$ with $(p_\infty - p_v) = 1\ bar$ a maximum pressure of $p_{max} = 1260\ bar$ is attained.

2.2. Numerical Modeling

In this section, numerical models relevant for current project are discussed. First the main CFD frameworks are discussed. Next, the available turbulence models for URANS simulations are reviewed. Furthermore, the Volume of Fluid (VOF) method and its implementation for a multiphase CFD simulation is elaborated. Next, cavitation modelling is discussed and the main cavitation models are reviewed.

All models reviewed in this section are available in the commercial CFD software Simcentre Star-CCM+.

2.2.1. CFD Frameworks

CFD is a broad term containing of different types of simulation methods. Commonly used approaches for aero and hydrodynamics problems are (Unsteady) Reynolds Averages Navier Stokes (U)RANS simulations which require eddy viscosity turbulence models, Large Eddy Simulations (LES) which require subgrid-scale turbulence models, and Detached Eddy Simulations (DES) which is a hybrid simulation framework combining (U)RANS and LES characteristics. In the rest of this section, some of the main general qualities of these CFD simulation methods are discussed.

(U)RANS

In RANS simulations, the Navier-Stokes equations are time averaged and thus the quantities are treated statistically with a mean and fluctuating component. As a result, an additional term, the Reynolds stress tensor, appears in the momentum transport equation. Consequently, this term needs to be solved for which several models have been developed. In Unsteady RANS (URANS), the temporary derivative of the velocity components is included and thus obtains transient solutions. The closure models used to solve the Reynolds stress term are discussed in section 2.2.2. Computationally, (unsteady) RANS simulations are generally less expensive compared with LES. This is one of the reasons it is widely used in the industry for practical applications. For cases of unsteady cloud cavitation, one would need to use URANS in order to capture the dynamics of the phenomenon. Also, in Star-CCM+, the VOF method cannot be used with steady RANS. Thus for the purpose of the current study, URANS is chosen both for steady cavitation cases as unsteady ones.

LES

In LES simulations, a spacial filter is applied which captures and solves all larges energetic scales and removes the small scales. The small scales should then be modelled with subgrid scale turbulence models. In this approach more of the actual turbulence is explicitly solved and less modelled and thus the error in the turbulence modelling should be less consequential and is often considered to be more accurate. On the other hand, for a LES simulation with a sufficiently refined filter, LES requires a much more refined grid and more iterations than RANS simulations and is therefore more computationally expensive than RANS. Furthermore, in LES the wall region is modelled which makes the model not very effective for shear driven flows with walls.

Hybrid model: DES

The Detached Eddy Simulation (DES) is a hybrid modelling approach that combines features of RANS modelling near the wall regions and LES modelling in detached flow regions. In this way, best of both worlds can be applied in cases where a RANS approach in the boundary layers is desired, and LES in the unsteady separated regions. As a result, DES keeps the advantages while avoiding the expensive mesh requirements of LES [34].

In STAR-CCM+, two DES variants are implemented: the Delayed Detached Eddy Simulation (DDES) and the Improved Delayed Detached Eddy Simulation (IDDES) [35].

The DDES variant has a delay factor implemented that help the model to distinguish between regions that need to be modelled RANS like and regions that need to be modelled LES like on mesh regions where there might be uncertainty about the choice of the application of either one of the models.

The IDDES variant incorporates a dependence on wall distance which allows RANS to be used in regions where the wall distance is much smaller than the boundary-layer thickness.

DES is a promising solution for certain simulations, however the meshing process should be approached with caution. [35]

2.2.2. (U)RANS Turbulence Models

In this section, the Eddy-Viscosity turbulence models are given which are available in STAR-CCM+. In the following sections, the fundamentals of the turbulence models is given and a few of the most common closure models are elaborated.

The Unsteady Reynolds Averaged Navier-Stokes (RANS) equations are derived by applying the Reynolds decomposition [13]

$$u_i = \overline{u_i} + u_i'$$

on the quantities in the Navier-Stokes equations and Reynolds averaging the set of equations. Where $\overline{u_i}$ is the ensemble average and u_i' the fluctuations of u_i.

Applying this for the incompressible Navier-Stokes equations and Reynolds averaging yields the RANS equations:

$$\frac{\partial \overline{u_i}}{\partial t} + \overline{u_j} \frac{\partial \overline{u_i}}{\partial x_j} = \overline{g_i} - \frac{1}{\rho} \frac{\partial \overline{p}}{\partial x_i} + v \frac{\partial^2 \overline{u_i}}{\partial x_j \partial x_j} - \frac{\partial \overline{u_i' u_j'}}{\partial x_j} \tag{2.23}$$

$$\tau_{ij} = -\overline{u_i' u_j'}$$

The problem with this formulations is that this expression always will have more unknowns than equations, i.e. no solutions exist. This also known as the Closure Problem. The RANS turbulence models solve this problem by approximating the Reynolds Stress Tensor.

Eddy viscosity models consider that turbulence leads to an exchange of momentum between fluid elements. It assumes the Reynolds Stress is proportional to the mean strain rate S_{ij}:

$$\tau_{ij} \cong 2v_T S_{ij} - \frac{2}{3} \delta_{ij} k \tag{2.24}$$

with the Kronecker delta function δ_{ij} and turbulence kinetic energy k. Substituting the eddy viscosity formulation into the RANS equations gives:

$$\frac{\partial \overline{u_i}}{\partial t} + \overline{u_j} \frac{\partial \overline{u_i}}{\partial x_j} = -\frac{\partial}{\partial x_i} \left(\frac{\overline{p}}{\rho} + \frac{2}{3} k \right) + \frac{\partial}{\partial x_j} \left(2(v + v_T) S_{ij} \right) \tag{2.25}$$

The modelling problem is now reduced to one unknown scalar field, namely the eddy viscosity v_T.

The Jones and Launder ($k - \varepsilon$) model

The Jones and Launder, or $k - \varepsilon$ model, is a two equation closure model that describes a transport equation for the turbulence kinetic energy k and for the turbulence dissipation rate ε. The transport equation for k goes as follows [15]:

$$\rho \left(\frac{\partial k}{\partial t} + \overline{u_j} \frac{\partial k}{\partial x_j} \right) = \frac{\partial}{\partial x_j} \left[\left(\mu + \frac{v_T}{\sigma_k} \right) \frac{\partial k}{\partial y} \right] + v_T \left(\frac{\partial \overline{u_i}}{\partial x_j} \right)^2 - \rho \varepsilon - 2\mu \left(\frac{\partial k^{0.5} x}{\partial x_j} \right)^2 \tag{2.26}$$

Transport equation for ε following the same structure as the transport equation for k:

$$\rho \left(\frac{\partial \varepsilon}{\partial t} + \overline{u_j} \frac{\partial \varepsilon}{\partial x_j} \right) = \frac{\partial}{\partial x_j} \left[\left(\mu + \frac{v_T}{\sigma_\varepsilon} \right) \frac{\partial \varepsilon}{\partial y} \right] + c_1 f_1 \frac{\varepsilon}{k} v_T \left(\frac{\partial \overline{u_i}}{\partial x_j} \right)^2 - c_2 f_2 \frac{\rho \varepsilon^2}{k} + 2\mu v_T \left(\frac{\partial^2 \overline{u_i}}{\partial x_j^2} \right) \tag{2.27}$$

with $v_T = c_\mu f_\mu \rho \frac{k^2}{\varepsilon}$, and constants

$$c_\mu = 0.09, \quad c_1 = 1.55, \quad c_2 = 2.0,$$

$$f_\mu = e^{\frac{-2.5}{1 + \rho k^2 / 50 \mu \varepsilon}}, \quad f_1 = 1, \quad f_2 = 1 - 0.3 e^{-\rho k^2 / \mu \varepsilon}$$

$$\sigma_k = 1.0, \quad \sigma_\varepsilon = 1.3$$

The $k - \varepsilon$ model is not very well suited for near wall flows since it is very sensitive for boundary conditions. It is best not to use it for flows with strong pressure gradients or separation.

The Witlox ($k - \omega$) model

The Wiltlox, or $k - \omega$, model is also e two equation model that describes the transport equation for the turbulence kinetic energy k and the specific turbulence dissipation rate $\omega = \frac{1}{C_D}\frac{\varepsilon}{k}$.

The transport equation for k reads [25] [13]:

$$\rho \left(\frac{\partial k}{\partial t} + \overline{u}_j \frac{\partial k}{\partial x_j} \right) = \tau_{ij} \frac{\partial \overline{u}_i}{\partial x_j} - \beta^* \rho \omega k + \frac{\partial}{\partial x_j} \left[(\mu + \sigma_{k1} v_T) \frac{\partial k}{\partial x_j} \right] \tag{2.28}$$

and the transport equation for ω reads:

$$\rho \left(\frac{\partial \omega}{\partial t} + \overline{u}_j \frac{\partial \omega}{\partial x_j} \right) = \frac{\gamma_1}{v_T} \tau_{ij} \frac{\partial u_i}{\partial x_j} - \beta_1 \rho \omega^2 + \frac{\partial}{\partial x_j} \left[(\mu + \sigma_{\omega 1} v_T) \frac{\partial \omega}{\partial x_j} \right] \tag{2.29}$$

With

$$v_T = \frac{k}{\omega} \quad , \quad \tau_{ij} = 2 v_T S_{ij} - \frac{2}{3} \delta_{ij} k$$

and constants

$$\sigma_k = 0.5, \quad \sigma_\omega = 0.5, \quad \beta = 0.0750$$
$$\beta^* = 0.09, \quad \kappa = 0.41, \quad \gamma = \beta_1/\beta^* - \sigma_\omega \kappa^2/\sqrt{\beta^*}$$

This model is less sensitive to boundary conditions and thus better suited for flow predictions in the boundary layer or flow with pressure gradients and separation.

SST model

The SST turbulence model is a combination of the $k - \varepsilon$ model in the exterior flow, with the $k - \omega$ in the boundary layer in order to benefit from the best of both models.

The high-Reynolds-number version of the $k - \varepsilon$ model is formulated such that it matches the $k - \omega$ form [25]:

$$\rho \left(\frac{\partial k}{\partial t} + \overline{u}_j \frac{\partial k}{\partial x_j} \right) = \tau_{ij} \frac{\partial \overline{u}_i}{\partial x_j} - \beta^* \rho \omega k + \frac{\partial}{\partial x_j} \left[(\mu + \sigma_k' v_T) \frac{\partial k}{\partial x_j} \right] \tag{2.30}$$

$$\rho \left(\frac{\partial \omega}{\partial t} + \overline{u}_j \frac{\partial \omega}{\partial x_j} \right) = \frac{\gamma}{v_T} \tau_{ij} \frac{\partial \overline{u}_i}{\partial x_j} - \beta' \rho \omega^2 + \frac{\partial}{\partial x_j} \left[(\mu + \sigma_\omega' v_T) \frac{\partial \omega}{\partial x_j} \right] + 2 \rho \sigma_\omega' \frac{1}{\omega} \frac{\partial k}{\partial x_j} \frac{\partial \omega}{\partial x_j} \tag{2.31}$$

With the constants:

$$\sigma_k' = 1.0, \quad \sigma_\omega' = 0.856, \quad \beta' = 0.0828$$
$$\beta^* = 0.09, \quad \kappa = 0.41, \quad \gamma' = \beta'/\beta^* - \sigma_\omega' \kappa^2/\sqrt{\beta^*} \tag{2.32}$$

The $k - \omega$ model is then multiplied by a function F_1 and the $k - \varepsilon$ model by $(1 - F_1)$. Both models are added together giving [25]:

$$\rho \left(\frac{\partial k}{\partial t} + \overline{u}_j \frac{\partial k}{\partial x_j} \right) = \tau_{ij} \frac{\partial \overline{u}_i}{\partial x_j} - \beta^* \rho \omega k + \frac{\partial}{\partial x_j} \left[(\mu + \sigma_k v_T) \frac{\partial k}{\partial x_j} \right] \tag{2.33}$$

$$\rho \left(\frac{\partial \omega}{\partial t} + \overline{u}_j \frac{\partial \omega}{\partial x_j} \right) = \frac{\gamma}{v_t} \tau_{ij} \frac{\partial \overline{u}_i}{\partial x_j} - \beta \rho \omega^2 + \frac{\partial}{\partial x_j} \left[(\mu + \sigma_\omega v_T) \frac{\partial \omega}{\partial x_j} \right] + 2 (1 - F_1) \rho \sigma_{\omega 2} \frac{1}{\omega} \frac{\partial k}{\partial x_j} \frac{\partial \omega}{\partial x_j} \tag{2.34}$$

For any constant ϕ in the *SST* model, the corresponding constant from the $k - \omega$ model ϕ_1 (see 2.2.2) and corresponding constant from the (rewritten) $k - \varepsilon$ model ϕ_2 (see 2.32), the resulting constant is composed as follows:

$$\phi = F \phi_{k-\omega} + (1 - F) \phi_{k-\varepsilon}$$

The function F is designed to equal 1 in the sublayer and logarithmic region of the boundary layer and 0 in the wake region. It is defined as follows:

$$F = tanh \left[max \left(2 \frac{\sqrt{k}}{0.09 \omega y} ; \frac{500 v}{y^2 \omega} \right) \right]^2 \tag{2.35}$$

with y being the distance to the next surface.

The value of σ_k from the $k - \omega$ model is changed to $\sigma_k = 0.85$, and the eddy viscosity is defined as:

$$v_T = \frac{ak}{max(a\omega; \Omega F)} \qquad (2.36)$$

with $a = 0.31$.

This model has been documented to show good behaviour in adverse pressure gradients and separating flows. Although the model is designed to benefit from the best properties of the $k - \omega$ and $k - \varepsilon$ models, it does not always give more accurate results than the separate models.

The Spallart-Allmaras model

The Spallart-Allmaras model is a one equation model based on a postulated transport equation for the eddy viscosity [13]:

$$\frac{\partial \tilde{v}}{\partial t} + \overline{u} \cdot \nabla \tilde{v} =$$

$$C_{b1}(1 - f_{t2})\tilde{S}\tilde{v} + f_{t1}\Delta u^2 + \frac{1}{\sigma}\nabla \cdot [(v + \tilde{v})\nabla \tilde{v}] + \frac{C_{b2}}{\sigma}|\nabla \tilde{v}|^2 - \left[C_{w1}f_w - \frac{C_{b1}}{\kappa^2}f_{t2}\right]\left(\frac{\tilde{v}}{d}\right)^2$$

with

$$v_t = \tilde{v}f_{v1}, \quad f_{v1} = \frac{\chi^3}{\chi^3 + C_{v1}^3}, \quad f_{v2} = 1 - \frac{\chi}{1 + \chi f_{v1}},$$

$$\chi = \frac{\tilde{v}}{v}, \qquad \tilde{S} = \sqrt{2\Omega_{ij}\Omega_{ij}} + \frac{\tilde{v}}{\kappa^2 d^2}f_{v2},$$

$$\Omega_{ij} = \frac{1}{2}\left(\frac{\partial u_j}{\partial x_i} - \frac{\partial u_i}{\partial x_j}\right), \quad f_w = g\left[\frac{1 + C_{w3}^6}{g^6 + C_{w3}^6}\right]^{1/6}, \quad g = r + C_{w2}\left(r^6 - r\right)$$

$$r = \frac{\tilde{v}}{\tilde{S}\kappa^2 d^2}, \quad f_{t1} = C_{t1}g_t \exp\left(-C_{t2}\frac{\omega_t}{\Delta u^2}\left[d^2 + g_t^2 d_t^2\right]\right), \quad f_{t2} = C_{t2}\exp\left(-C_{t4}\chi^2\right)$$

This model is robust and efficient since it only solves one equation. It is know to give good results for simple attached flows as well as flow is separation. It less suited for the prediction of flow re-attachment and free shear layers.

2.2.3. Multiphase VOF Model

For the simulation of cavitation in a fluid, a formulation is needed which represents both the liquid and vapor phase. In this section, the multi-phase Volume of Fluid approach is elaborated.

In this formulation, the distribution of phases are defined with respect to the phase volume fraction α_i of phase i which describes the presence of the different phases in a grid cell. In this case, a system of a liquid phase l and vapor phase v needs to be described. Hence, the liquid and vapor volume fractions are described respectively as [36]:

$$\alpha_l = \frac{V_l}{V} \qquad and \qquad \alpha_v = \frac{V_v}{V}, \qquad (2.37)$$

where the sum of the volume fractions of all phases must equal 1. For cells only containing the liquid phase, the liquid volume fraction becomes $\alpha_l = 1$ and the vapor volume fraction $\alpha_v = 0$. And vice versa for cells containing only the vapor phase. Cells with values of α_i between 0 and 1 indicate a presence of both liquid and vapor and an interface in the cell. The method requires at least three cells across each droplet or bubble, meaning that no bubbles or droplets can be captured within a single cell for cells with $0 < \alpha_v < 1$. In such a case, the mesh should be further refined so that the droplet is again encapsulated by at least three cells.

The mixture density ρ_m and dynamic viscosity μ_m are then defined as a function of the liquid and vapor densities:

$$\rho_m = \alpha_l \rho_l + \alpha_v \rho_v, \qquad (2.38)$$

$$\mu_m = \alpha_l \mu_l + \alpha_v \mu_v. \tag{2.39}$$

With this formulation, the continuity and momentum equation can be expressed as:

$$\frac{\partial \rho_m}{\partial t} + \frac{\partial \left(\rho_m u_j \right)}{\partial x_j} = 0 \tag{2.40}$$

$$\frac{\partial \left(\rho_m u_i \right)}{\partial t} + \frac{\partial \left(\rho_m u_i u_j \right)}{\partial x_j} = -\frac{\partial p}{\partial x_i} + \frac{\partial}{\partial x_j} \left[\mu_m \left(\frac{\partial u_i}{\partial x_j} + \frac{\partial u_j}{\partial x_i} - \frac{2}{3} \frac{\partial u_k}{\partial x_k} \delta_{ij} \right) \right]. \tag{2.41}$$

With the decomposition of the liquid and vapor phases, the continuity equation can also be decomposed for phase i:

$$\frac{\partial \left(\rho_i \alpha_i \right)}{\partial t} + \frac{\partial \left(\rho_i \alpha_i u_j \right)}{\partial x_j} = \dot{m}_i \tag{2.42}$$

with the source term (or mass transfer rate) $\dot{m}_i$. For some models this term is divided up in a source and sink (or evaporation and condensation) term $\dot{m}_i = \dot{m}_i^+ - \dot{m}_i^-$. Replace the subscript l with v for the continuity decomposition 2.42 for the vapor phase. To simulate cavitation in this framework, source and sink terms in this VOF method are defined by a cavitation model.

2.2.4. Cavitation Modelling

To describe cavitation with the VOF multiphase method, a seed-based mass transfer model is used [37].

In order for cavitation to occur (as discussed in section 2.1.1), cavitation nuclei need to be initially present in the fluid. The cavitation starts to expand outward from these seeds. In this present model, the following assumptions are made: (1) The seeds are uniformly distributed in the liquid, characterized by the number of seeds per unit of volume of liquid n_0. (2) All seeds initially have the same radius.

The number of seeds in a control volume V can now be expressed as a function of the seed density and liquid volume fraction $N_s = n_0 \alpha_l V$. With the volume of a bubble being $V_b = \frac{4}{3} \pi R^3$, the total vapor volume in the control volume becomes:

$$V_v = N_s V_b = n_0 \alpha_l V \frac{4}{3} \pi R^3 \tag{2.43}$$

Assuming the volume fraction is known, the bubble radius can now be calculated:

$$R = \left(\frac{3 \alpha_v}{4 \pi n_0 \alpha_l} \right)^{1/3} \tag{2.44}$$

The rate of change of a bubble volume is can now be expressed as:

$$\frac{dV_b}{dt} = 4 \pi R^2 \frac{dR}{dt} = 4 \pi R^2 \dot{R}$$

Multiplying with the number of seeds in the control volume N_s and the vapor density density ρ_v gives the mass transfer rate per unit volume from the left hand side of continuity equation 2.42:

$$\dot{m} = n_0 \alpha_l \rho_v 4 \pi R^2 \dot{R} \tag{2.45}$$

The only unknown left in the mass transfer rate 2.45 is the bubble radius velocity $\dot{R}$.

At this point, the various Cavitation models provide different approaches. In the following section, the various models will be discussed.

Rayleigh-Plesset

The Rayleigh-Plesset (R-P) cavitation model calculates the bubble radius velocity $\dot{R}$ by solving the Rayleigh-Plesset equation as derived in 2.1.2, neglecting the non-condensable gas term [37]:

$$\rho \left[R\ddot{R} + \frac{3}{2}\dot{R}^2 \right] = p_v - p_\infty - \frac{2S}{R} - 4\mu\frac{\dot{R}}{R} \tag{2.46}$$

This equation can be rearranged and solved iteratively using an implicit Euler Scheme.

This is the most accurate model option since it takes into account the bubble radius acceleration, surface tension and viscosity terms. On the other hand, this also makes it the most computationally expensive cavitation model to use.

Schnerr-Sauer

The Schnerr-Sauer (S-S) model is a simplification of the Rayleigh-Plesset equation where the bubble radius acceleration, surface tension, non-condensable gas and viscosity terms are neglected yielding [37]:

$$\dot{R} = \sqrt{\frac{2}{3}\left(\frac{p_v - p}{\rho_l}\right)} \tag{2.47}$$

Due to the simplification, the Schnerr-Sauer model is less computationally expensive compared with the full Rayleigh-Plesset model 2.2.4. However, it might not capture all the necessary physics depending on the application and the accuracy requirements. For the analysis of steady and unsteady cavitation around hydrofoils, numerous papers show results of the Schnerr-Sauer model to be coherent with experimental results [22] [27]. This makes it a good candidate for application in this study and will therefore be implemented in this work.

2.3. Linear Theory of Cavitation

Thin airfoil theory is a linear theory based on potential flow around a two dimensional airfoil with small thickness with respect to the chord length. Using this theory expressions for lift and drag as a function of the angle of attack can be derived. Potential flow assumes an inviscid, incompressible and irrotational fluid meaning that its an idealised model. Nevertheless, it serves as a valuable tool to gain insight on basic properties of the airfoil.

Tulin used thin airfoil theory to derive an expression for the maximum cavity length l_{max}/c as a function of the parameter $\frac{\sigma}{2\alpha}$ with angle of attack α (in radians) for cavities larger than the chord length [39]:

$$\alpha \left(\frac{2}{\sigma} + 1 \right) = (l-1)^{\frac{1}{2}} \tag{2.48}$$

Acosta extended this and derived an expression which describes the maximum cavity length as a function of $\frac{\sigma}{2\alpha}$ for partial cavitation (smaller that the chord length) [1]:

$$\frac{\sigma}{2\alpha} = \frac{1}{\left(\frac{c}{l_{max}} - 1 \right)^{1/2}} \left[2 \frac{c}{l_{max}} - 1 + 2 \left(\frac{c}{l_{max}} \right)^{1/2} \left(\frac{c}{l_{max}} - 1 \right)^{1/2} \right] \tag{2.49}$$

Both expressions are visualised in figure 2.7.
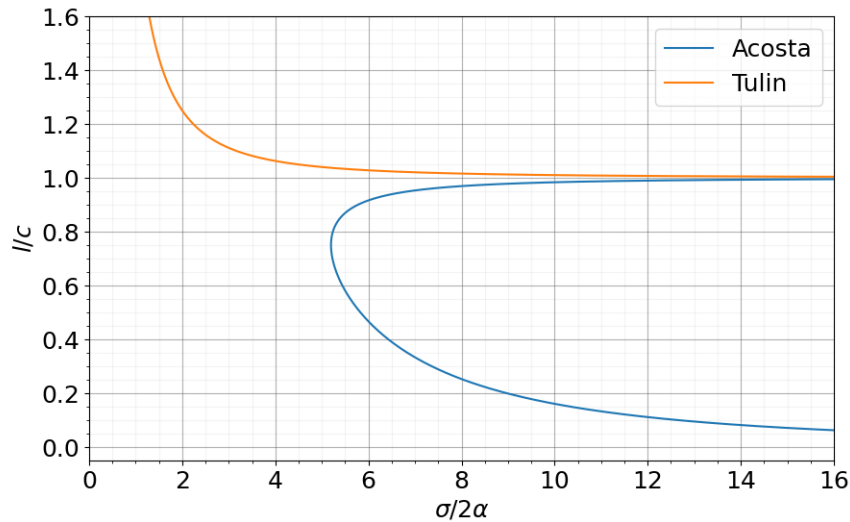
Figure 2.7: Relation of $\frac{\sigma}{2\alpha}$ with respect to the maximum cavity length expressed by Acosta [1] for partial cavitation and Tulin [39] for super cavitation.

3

Methodology

In this chapter, the methodology towards answering the research questions is elaborated. First, two test cases are presented which are used to validate the simulation results and the numerical models used in this work. A test case for non-cavitating as well as a case for cavitating conditions are presented, for which the geometry, operating conditions and experimental reference is discussed. Next, the procedures in order to make a robust and accurate CFD simulation are discussed. Moreover, a method comparison of cavitation analysis with and without cavitation model is proposed, as well as an analysis of the stability of steady to unsteady cavitation and a polar and efficiency analysis.

3.1. Test Cases

On order to validate the simulation results and numerical models used in this work, test cases are simulated for which experimental data is available. In order to gradually work towards the final set-up, a non-cavitating case is considered first. When this non-cavitating case is validated, the cavitating case can be implemented using the non-cavitating case as a starting point. In this section, the geometries, operating conditions and experimental reference data of the two test cases are discussed.

3.1.1. Non-Cavitating

The experimental reference data is from a NASA Report by Ladson [19]. This data is used to validate the non cavitating CFD simulation results.

For the non-cavitating test case, a NACA-0012 section geometry is chosen (see figure 3.1). The section is symmetric and has a relative maximum thickness of 12% of the chord at 30% of the chord length. The coordinates data of the geometry are from the UIUC Airfoil Coordinates Database [31]. A chord length of 1 m is chosen.
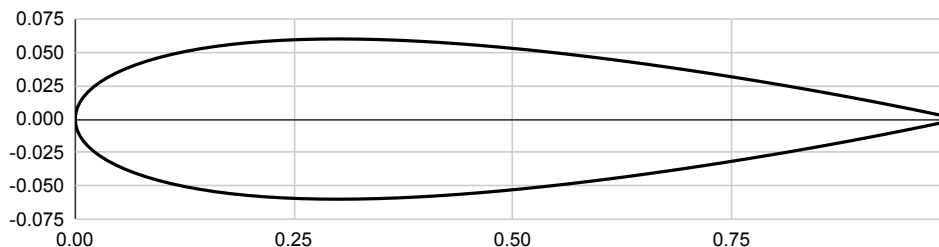
Figure 3.1: NACA-0012 Geometry

For the non-cavitating test case, the Reynolds number is set to $Re = 5.93 \times 10^6$, the Mach number to $M = 0.3$ in air with a density of $\rho = 1.225\,kgm^-3$. The following series of angles of attack is measured $\alpha = [-2.02, 4.03, 6.08, 8.13, 10.12, 12.12, 14.27, 16.25]$.

3.1.2. Cavitating

The experimental reference data for the cavitating test case is from Leroux et. al. [20]. This test case will be used to validate the cavitating set-up and the numerical models used in the simulations. Numerous academics have used the experimental data from Leroux for validation purposes. Seo et. al. is one of them and performed numerical validation on the same test case [32]. His results are also used for comparison in the results.

The geometry used for this case is a NACA-66(mod) section geometry (see figure 3.2). The NACA-66 geometry has a relative maximum thickness of 12% of the chord at 45% of the chord length and with a relative maximum camber of 2% at 50% from the chord length. The coordinates of this modified NACA-66 geometry are provided in the paper from Leroux et. al. [20]. The chord length is $c = 0.15$. The saturation vapor pressure
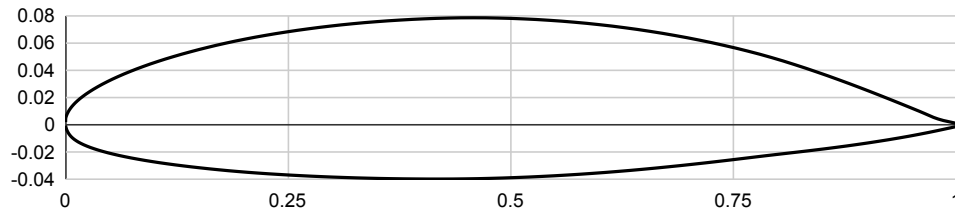
Figure 3.2: Modified NACA-66 Geometry

Steady Sheet Cavitation

The operating conditions used in this test case are as follows. The freestream velocity is set at $U_\infty = 5.33\,m/s$ corresponding to a Reynolds number of $Re = 0.8 \times 10^6$ in water with a density of $997.98\,kg/m^3$ at an angle of attack of $\alpha = 6.5°$. The cavitation number is varied for values of $\sigma = [1.29, 1.35, 1.4]$ and one for non-cavitating flow, i.e. $\sigma > 2$.

Unsteady Cloud Cavitation

When the steady sheet cavitation cases have been carried out, operating conditions for unsteady cloud cavitation are implemented and conducted. For the first unsteady cloud cavitation case, an angle of attack of $\alpha = 6.5°$, a cavitation number of $\sigma = 1.05$ and a freestream velocity of $U_\infty = 5.33\,m/s$ is used. For the second cloud cavitation case, the angle of attack is set to $\alpha = 8°$, the cavitation number to $\sigma = 1.27$ and the freestream velocity stays at $U_\infty = 5.33\,m/s$. For the third cloud cavitation case, the angle of attack is set to $\alpha = 8°$, $\sigma = 1.31$ and a freestream velocity of $U_\infty = 12.86\,m/s$ (or 25 $knts$). For this last case, no experimental data is available and hence this case cannot be used for the actual validation. The purpose of this case is to see how the model handles more extreme cloud cavitation scenarios.

3.2. CFD Simulation Setup

For this project, an finite volume Unsteady RANS solver from the commercial software Star-CCM+ is used. In order to create a robust simulation which obtains accurate results, several steps need to be taken into account. In this section, an in depth overview of the necessary steps are discussed.

3.2.1. Meshing Strategy

The first step in making a finite volume CFD simulation is making an appropriate computational mesh on which the solutions of the URANS equations are calculated.

The first consideration is the dimensionality of the computational mesh, which can be two or three dimensional. At first glance, a two dimensional domain would be a natural choice since for this study two dimensional hydrofoil sections are considered. Also the amount of cells is many times smaller for a two dimensional domain than for a three-dimensional domain, reducing the computational time considerably. However, since cavitating flow is turbulent and therefore inherently shows three dimensional flow dynamics, this choice should be reconsidered carefully. For steady cavitation bubbles, the bubble length is more or less constant and the three dimensional flow effects should therefore be limited. For unsteady cloud cavitation however, cavitation bubbles are shedded periodically which is likely to show strongly three dimensional flow effects. Kashyap et. al. compared two and three dimensional flow responses around a hydrofoil section and observed that the key stages in the two dimensional cavity flows where consistent with the corresponding vorticity cycles for the three dimensional case [16]. Therefore, a two dimensional computational domain is concluded to be sufficiently accurate to capture the flow features considered in this study.

Furthermore, as the topology of a C-type grid and an automated unstructured polyhedral mesh generation is chosen. The automated mesh allows for easy mesh regeneration when performing a series of simulations with incrementing angle of attack of the hydrofoil geometry. Around the hydrofoil geometry prism layers are generated in order to capture and resolve the flow near the hydrofoil surface.

Boundary Layer Treatment

In order to In Star-CCM+, the controls of the prism layer is prescribed by number of prism layers N_p, the total prism layer thickness Δ_{tot} and the prism layer growth rate S_p. In order to capture the boundary layer sufficiently well, the values of these parameters must be set up with care. Since the viscous sub-layer needs to be captured, it is important that the value of the non-dimensional wall distance y^+ is below 1. For this, the definition of y^+ is used to find an appropriate value of the first layer thickness of the prism layer. The non-dimensional wall distance is defined as follows:

$$y^+ = \frac{y u_\tau \rho}{\mu} \tag{3.1}$$

with the friction velocity $u_\tau = \sqrt{\frac{\tau_w}{\rho}}$ and with the wall shear stress $\tau_w = \frac{1}{2} C_f \rho U_\infty^2$. The skin friction coefficient is estimated with Prandtl's one-seventh power law and provides a reasonable approximation for turbulent boundary layers: $C_f = 0.027 Re^{-1/7}$. With these definitions, one can find an expression for the wall distance estimate a value for the first prism layer thickness:

$$y = \frac{y^+ \mu}{\rho} \sqrt{\frac{2}{0.027 Re^{-1/7} U_\infty^2}}. \tag{3.2}$$

With the desired value for y^+ and the known values for the density ρ, viscosity μ and freestream velocity U_∞, one obtains the wall distance which is used as the first layer thickness Δ_1.

The total thickness of prism layer can now be expressed using the first layer, growth rate and the total number of layers using the geometric series, as follows:

$$\Delta_1 \frac{1 - S_p^{Np}}{1 - S_p} = \Delta_{tot}. \tag{3.3}$$

The growth rate is recommended to keep below 1.2 in order to limit numerical diffusion and the number of prism layers N_p is chosen.

When the simulation is run, the $y+$ value should be checked along the hydrofoil surface making sure it stays below 1. Furthermore, it should be verified that the velocity gradients from the boundary layer are within the prism layer along the hydrofoil geometry. If the velocity gradient falls outside of the prism layer, more layers should be added in order to thicken the total prism layer ensuring the gradients fall within the prism layer.

Non-cavitating Test Case

The dimensions of the computational domain are parameterized by the chord length c of the hydrofoil. The C-shaped domain forms a half circle upstream attached to a rectangle downstream from the hydrofoil geometry. The leading edge of the hydrofoil geometry is at the center of a half circle with radius $10\,c$ upstream from the body with. The rectangular part of the domain has height $10\,c$ in positive and negative y direction with respect to the foil geometry and $15\,c$ downstream in positive x direction measured form the leading edge of the hydrofoil (see figure 3.5).

Simcenter STAR-CCM+

mesh elements: 48750
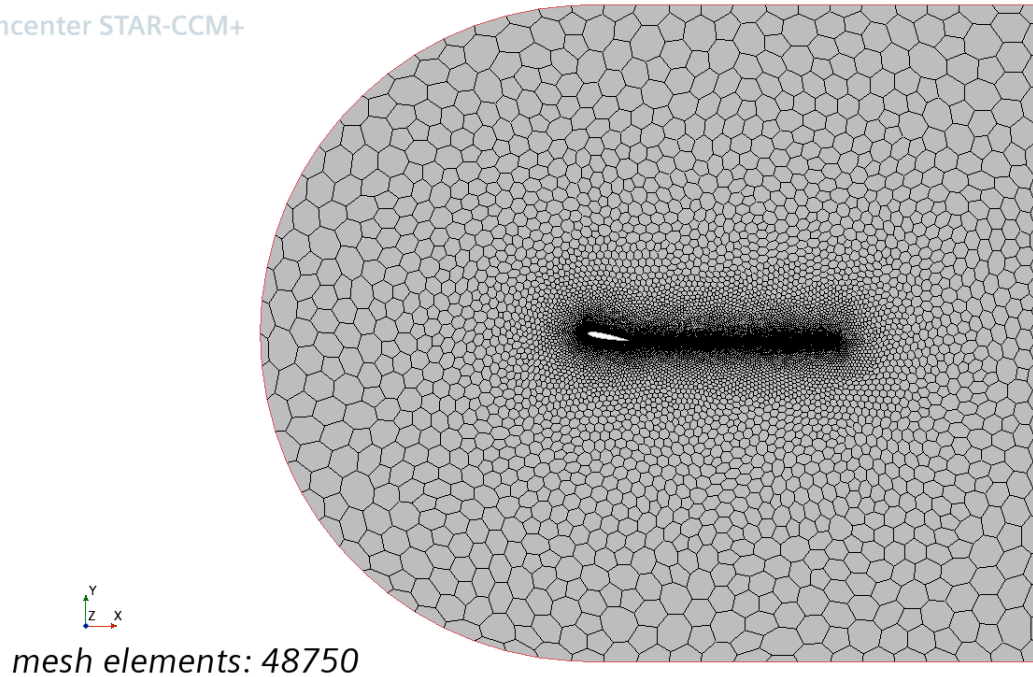
Figure 3.3: Full mesh

The cell sizes are parameterized with respect to the chord length c. The target size in the volume is set to $0.5c$, gradually decreasing the cell size towards the foil surface. Mesh control volumes are added to the leading and trailing edge in order to make additional refinements with cell sizes of about $10^{-4}c$ in these regions, assigning an appropriate growth rate to ensure that the size of the cells in these regions gradually changes to the cells in the volume. An additional mesh control volume is made as mesh refinement in the wake of the foil by adding a thin line with cells of about $10^{-2}c$ in x direction from the trailing edge of the foil up to about $8c$ downstream of the foil. Again, an appropriate growth rate is assigned to the cells in the wake in order to make the cells gradually fade in with the cells in the volume and on the other hand, not refining more cells than necessary outside the wake.

Cavitating Test Case

For the cavitating case, the meshing strategy is slightly modified. The dimensions of the computational domain have been increased by a factor 10. The parametrization is performed as described in the section for the non-cavitating case. However, the base mesh density $MS = 1$ has been slightly increased. The thickness of the prism layer has been increased with respect to the non-cavitating validation study in order to contain the cavitation bubble for stable sheet cavitation cases. In figure 3.6 a detail of the vapor volume fraction at the leading edge of the foil is shown for a converged steady cavitation case. The cell boundaries are highlighted in white to show that the converged cavity bubble (in red, i.e. vapor volume fraction close to 1) for $\sigma = 1.4$ is contained within the prism layer. Also, a slight refinement is added in the whole region above the suction side in order to account for more en stronger gradients in pressure and velocity due to the cavitation bubble.
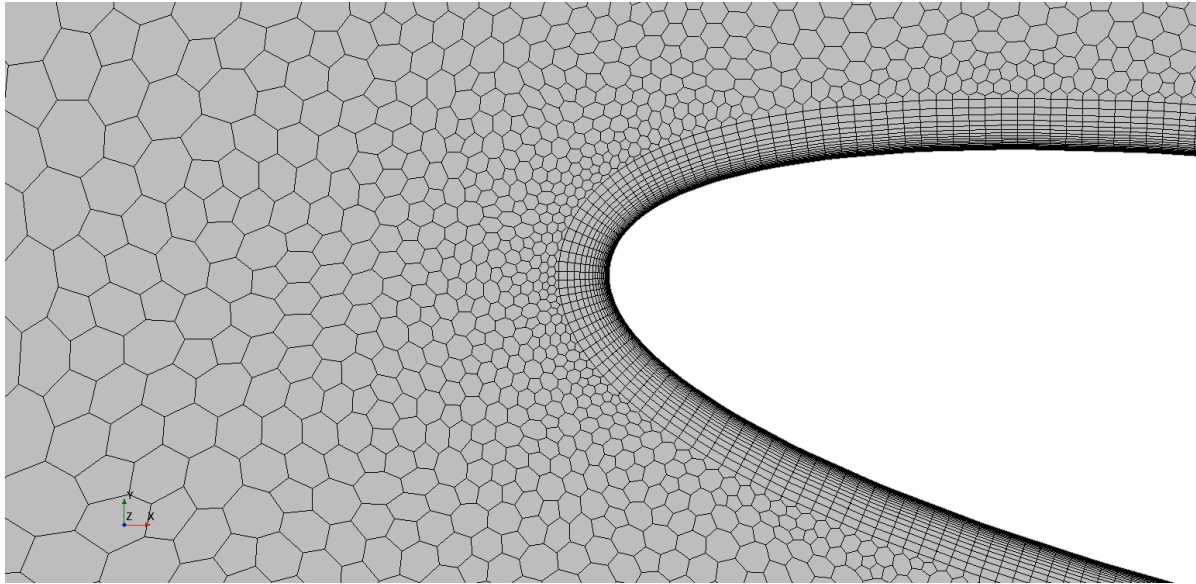
(a) Leading edge
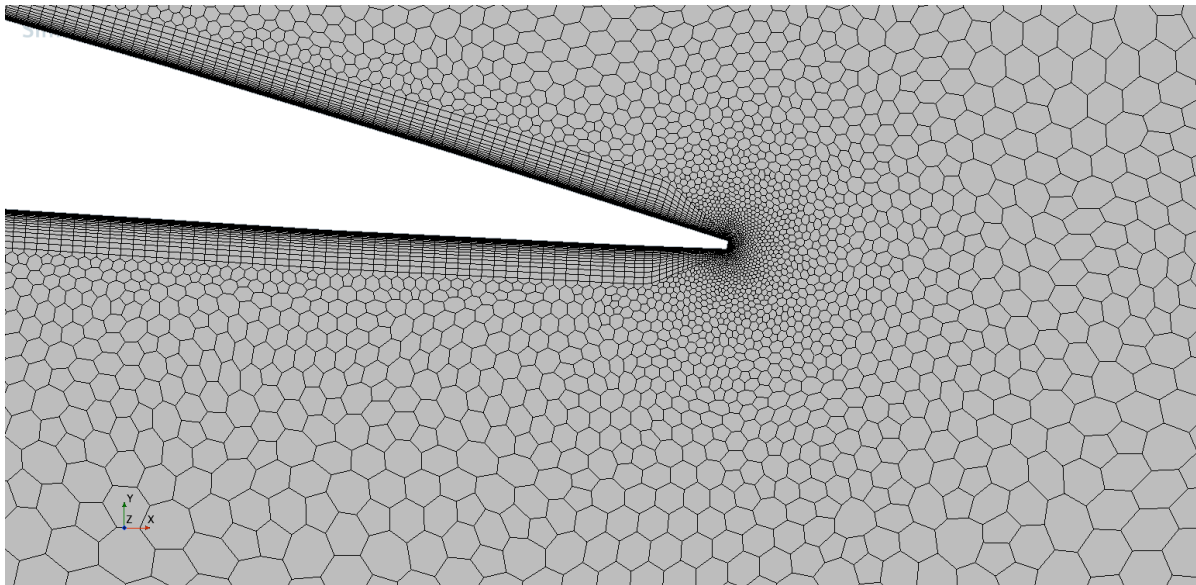
(b) Trailing edge

Figure 3.4: Mesh: Leading and trailing edge detail.
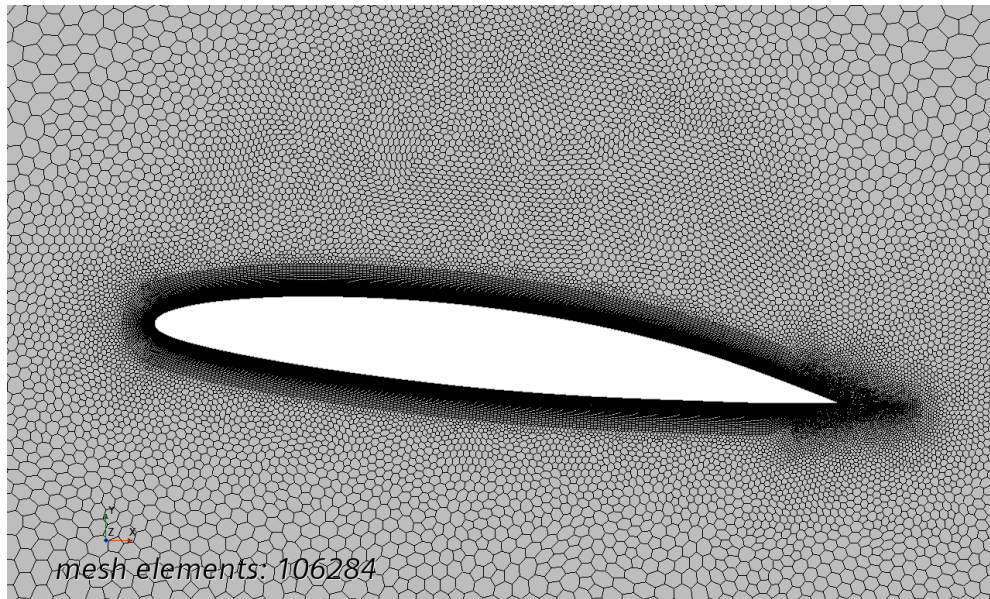
Figure 3.5: Mesh around the $NACA - 66(mod)$ geometry section.
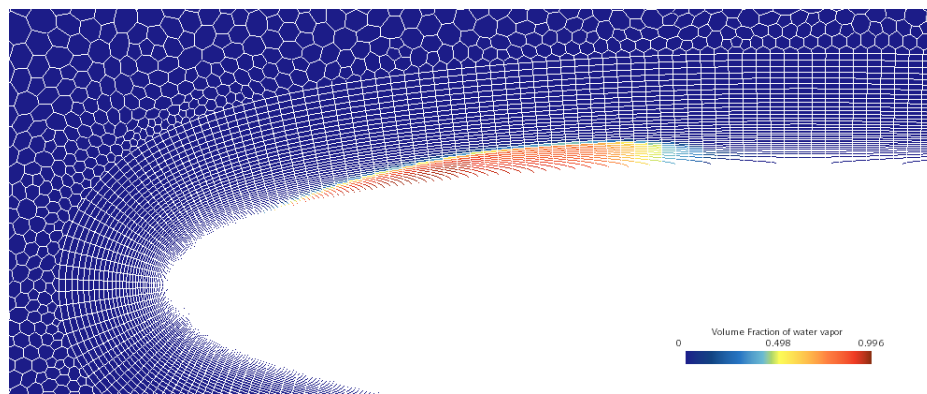
Figure 3.6: Detail of the volume fraction field a converged cavitation bubble at $\sigma = 1.4$ with highlighted mesh cell contours.

3.2.2. Mesh Convergence

Since the computational domain is discretized in finite volumes, it is inevitable that spatial discretization errors occur, reducing the accuracy of the flow solution. Increasing the mesh density can help mitigating these errors, increasing the resolution and accuracy of the flow solution. The number of cells in a simulation could theoretically be increased indefinitely, however at one point, the increase in computational cost does not outweigh the increase of accuracy in the flow solution. A mesh convergence study aims to analyse how the converged flow solution depends on the mesh density. By doing so, it aims to find an appropriate mesh density considering the accuracy of the flow solution and the computational cost. The mesh convergence study is performed by running the same simulation while using different mesh densities.

Non-Cavitating Case

For A mesh scaling parameter MS is added to the parametric cell sizes in the volume, in the refined regions in the leading edge, trailing edge and wake, as well as in the prism layer. A series of values for this mesh scaling parameter is chosen, i.e. $MS = [1.4, 1.2, 1, 0.8, 0.6, 0.4]$, resulting in meshes with respectively, 29003, 33319, 39453, 48750, 63029 and 94433 mesh elements. Hence, this parameter quantifies the respective mesh densities from coarse to fine. In figure 3.7, the meshes around the foil geometry with highest and lowest mesh density around are shown.

(a) $MS = 0.4$

(b) $MS = 1.4$
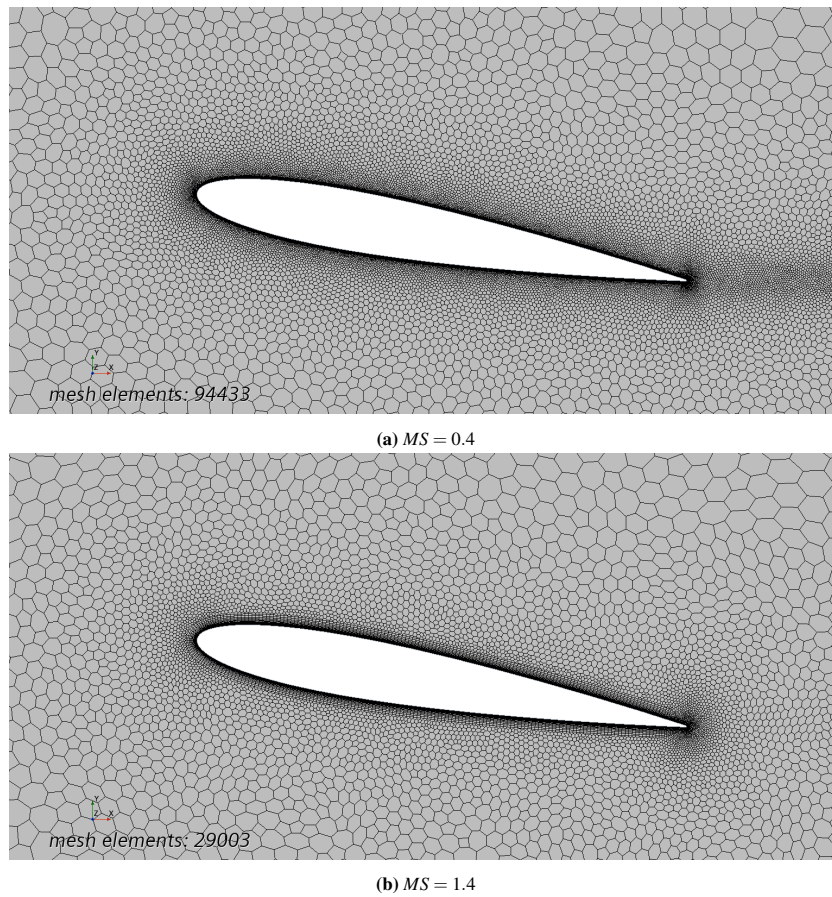
Figure 3.7: Mesh around the hydrofoil geometry with highers and lowest mesh density.

The simulations are now ready to be run. When the simulations are completed, the simulation time, lift and drag coefficients are compared and plotted to analyse how the solutions converge with respect to the number of mesh elements, i.e. mesh densities.

Cavitating Case

For the mesh convergence study for the cavitating case, the following series of scaling factors is chosen $MS = [1.2, 1, 0.8, 0.6, 0.4]$. In figures 3.8a and 3.8b the mesh around the foil surface is shown for the mesh scaling of 1.2 and 0.4 respectively.
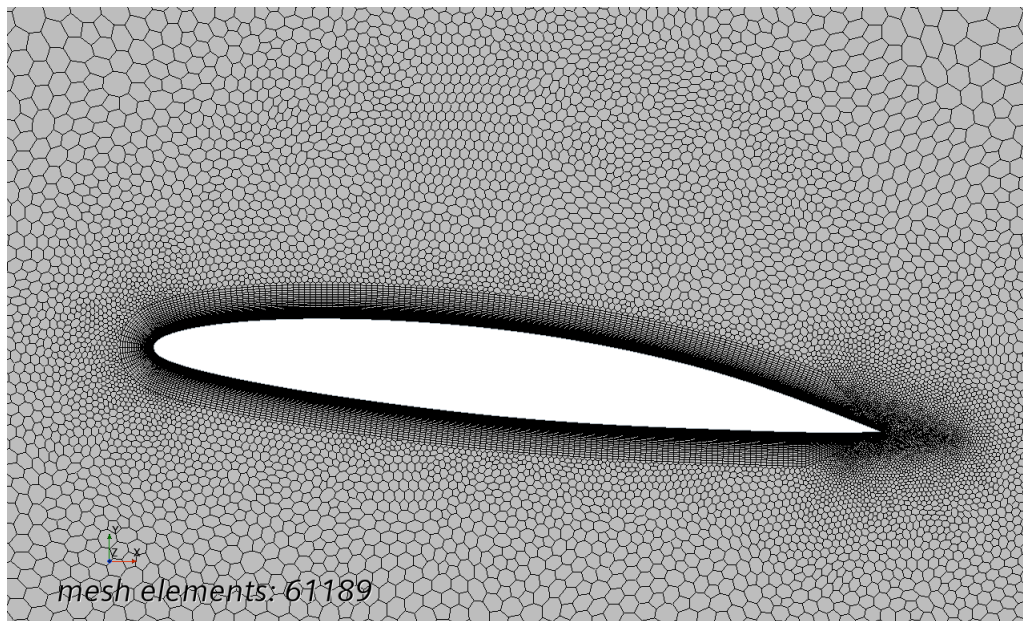
(a) For $MS = 1.2$
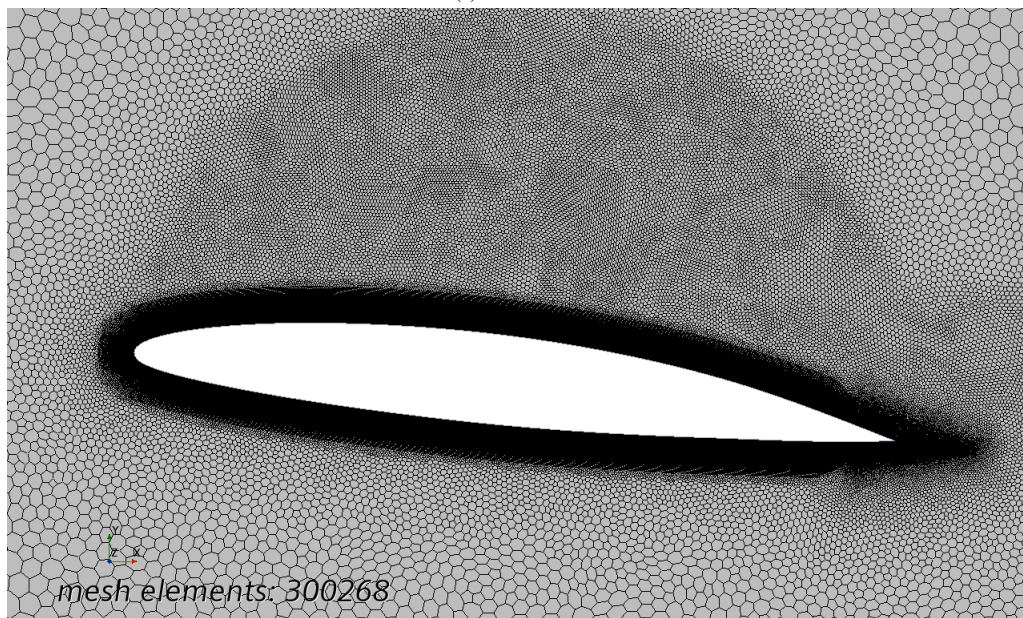
(b) For $MS = 0.4$

Figure 3.8: Mesh around the foil surface

3.2.3. Time-Step

For Unsteady RANS simulations, i.e. the cavitating test case simulations, the influence of the solver time-step size should also be investigated. For this, a base time-step of $dt = t_0/200$ is chosen [16] with the characteristic time-step t_0 defined as $t_0 = c/U_\infty$. This base time-step is then divided by a factor 2 and 4. A test case simulation is then run with the chosen time-steps $dt = [t_0/200, t_0/400, t_0/800]$, from which the pressure lift and drag coefficients results are compared with experimental reference data from this test case in order to asses the influence of the time-step on the simulation solution. From this study, the times-step size for the final set-up is chosen.

3.2.4. Turbulence Model

In the current study, a (U)RANS CFD framework is used which requires turbulence models in order to solve the solver equations. One of the four models using the Boussineq hypothesis, the *SA*, $k - \varepsilon$, $k - \omega$ or the *SST* turbulence model, is to be chosen for the final set-up. However, these models are all possible candidates and thus

should a comparison study be conducted. Since the *SST* model combines the $k - \varepsilon$ properties in exterior flow and $k - \omega$ near the wall, the $k - \varepsilon$ model will not be included in the comparison as cavitating flow is mainly exterior flow. Thus, the cavitating reference case simulation is run for the *SST*, $k - \omega$ and *SA* turbulence model and the results are compared with the experimental data. From this study, the turbulence model for the final set-up is chosen.

3.2.5. Turbulent Viscosity

In the $k - \omega$ and $k - \varepsilon$ turbulence models, the effective viscosity in the transport equations is defined as $\mu = \mu_l + \mu_t$ with the liquid viscosity μ_l and turbulent viscosity defined as

$$\mu_t = \rho \, C_\mu k^2 / \varepsilon$$

for the $k - \varepsilon$ model and

$$\mu_t = \rho \, C_\mu k / \omega$$

for the $k - \omega$ turbulence model. These (U)RANS turbulence models are developed for fully in-compressible single-phase flows and are not intended to be used for flow problems involving compressible multi-phase mixtures like cavitation. To account for this problem, Coutier-Delgosha [9] proposed a modification to the turbulent viscosity where the density ρ is replaced by a function of the mixture density

$$\mu_t = f(\rho_m) \, C_\mu k^2 / \varepsilon$$

with the new density function defined as

$$f(\rho_m) = \rho_v + \left(\frac{\rho_v - \rho_m}{\rho_v - \rho_l} \right)^n (\rho_l - \rho_v).$$

Figure 3.9 shows how the modified turbulent viscosity with $n = 3$ (as used by Tran et. al. [38] and by Zhou et. al. [46]) for cavitation is reduced as a function of the mixture density with respect to the non modified mixture density varying form the density of water vapor $\rho = 0.023 kg/m^3$ to the density of water $\rho = 997.561 kg/m^3$.
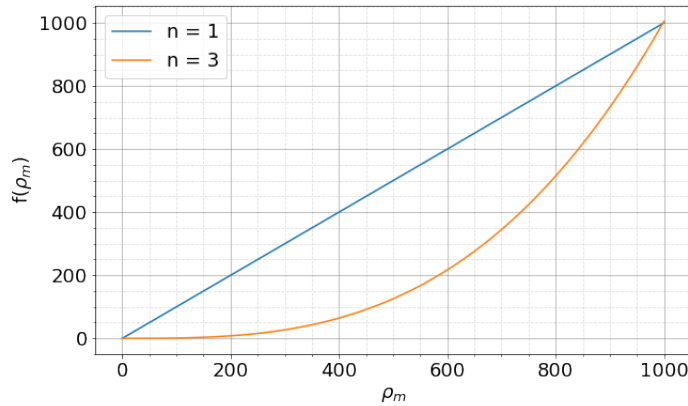
Figure 3.9: Turbulent viscosity as a function of the mixture density for the $n = 1$ (non-modified) and $n = 3$ (modified).

This modification is implemented and tested for $n = 3$, $n = 2$ and $n = 2.3$ and the results are compared with the experimental data.

3.2.6. Cavity Length Measurement

For the measurement of the cavitation bubble length within the CFD simulation, the vapor volume fraction field is used. The vapor volume fraction has a value between 0 and 1 for each cell in the mesh. When the cell contains only water the values is 0 when the cell contains only water vapor the value is 1. For values between 0 and 1 the cell contains an interface between the water and vapor phase. For the measurement of the cavity length, the difference between the minimum and maximum x-position values is taken, in the hydrofoil section reference frame, where the volume fraction is 0.5. The choice in this definition of the cavity length works well for stable

cavitation bubble. However, for unsteady cavitation cases where the cavitation bubble detaches and sheds into the flow, the value of the maximum x-position of the cavitation follows the shedded part of the cavitation. Hence, this definition does not exclusively define the length of the "main" unbroken and attached cavitation bubble for all cases. This should be taken into consideration, especially for unsteady cloud cavitation cases.

3.3. Cavitation Analysis With vs. Without Cavitation Model

Once the CFD set-up is validated and ready to be used, a study is done where CFD results acquired with cavitation model are compared to results acquired without cavitation model. This study is performed in order to asses the analysis of cavitation in CFD without cavitation model where only the pressure distribution is analysed of a flow undisturbed by cavitation.

For this study, the same geometry and conditions are used as the cavitating test case. The geometry is the modified $NACA - 66$ section (see **??**) with $c = 0.15$ at $\alpha = 6.5°$ in a freestream velocity of $U_\infty = 5.33\ m/s$ and $Re = 8 \times 10^5$. This time, the simulation will only be run for cavitation number $\sigma = 1.4$. This simulation will be run two times, once with the validated cavitation set-up enabled. and once without the numerical cavitation model.

A similar comparison is performed for section geometry referred to as BPXI. This time the operating conditions are $\alpha = 4°$, $U_\infty = 18.52\ m/s$ (or $36\ knts$) and $\sigma = 0.63$. For this hydrofoil section and these conditions, the flow around the foil has presumably been known to cause cloud cavitation.

A comparison of the pressure distribution and the pressure field will give an indication if the more "primitive" cavitation analysis without cavitation model is missing important information and if so, what important information could be missing.

3.4. Stability Analysis

The influence of the cavitation bubble length on the cavitation stability has been studied experimentally and has been documented by Leroux [20]. The cavitation is observed to be stable for a cavity length up to about $l/c = 0.5$. For $l/c > 0.5$, cavity starts to oscillate in length and produces cloud cavitation. Reducing the cavitation number further increases the cavity up to a point where the cavity becomes stable again and covers the whole suction side of the hydrofoil, i.e. $l/c > 1$. This regime (or cavitation type) is called super cavitation.

As discussed in section 2.3, Acosta [1] and Tulin [**tulin_steady_1960**] derived analytical expressions for the relationship between the cavity length l/c and the parameter $\frac{\sigma}{2\alpha}$ for cavities on a flat plate and slender bodies. Watanabe et. al. further analysed analytically the transitional and partial cavitation [41]. Kjeldsen et. al. [18] carried out experiments using a $NACA - 0015$ section geometry in a water tunnel to investigate the spectral characteristics of cloud and sheet cavitation using the parameter $\frac{\sigma}{2\alpha}$ to characterize the different cavitation regimes. Arndt et. al. numerically investigated the same test case used by Kjeldsen found a criterion for cavitation stability given by $\frac{\sigma}{2\alpha} \approx 4$ [4]. When this criterion is surpassed, Arndt found that the sheet cavity becomes unstable. This result was found to be coherent with results from Leroux's study [20] on the $NACA - 66(mod)$ using the parameter $\sigma/2(\alpha - \alpha_0)$ with α_0 the angle of attack for which the section geometry gives zero lift, i.e. $C_L = 0$. For the $NACA - 66(mod)$, this angle of attack has a value of $\alpha_0 = -2.5$ [21].

For the stability analysis in the current study, a series of 25 simulations is carried out for fixed flow velocity at $u_\infty = 5.33\ m/s$ with the following values of the cavitation number $\sigma = [2, 1.6, 1.4, 1.35, 1.29]$ and the following angles of attack $\alpha = [0, 2, 4, 6, 8]$ degrees.

A second series of 35 simulations is run at fixed absolute pressure where $p_{abs} = \rho g d + p_{atm}$ choosing depth d to be at 1 meter below the free surface. The value of the cavitation number is then varied by changing the free stream velocity. The simulations are thus carried out for all combinations of values for the free stream velocity $u_\infty = [15, 20, 25, 30, 35, 40, 45]$ knots and angles of attack of $\alpha = [0, 2, 4, 6, 8]$ degrees.

As a asymmetrical section is used in this study, the stability parameter $p_s = \frac{\sigma}{2(\alpha - \alpha_0)}$ is used with α_0 being the angle of attack for zero lift. The result for the cavity bubble length of both series of simulations is plotted as a function of stability parameter p_s alongside the relation derived from linear theory. The error bars of the root mean squared of the cavitation bubble length over time gives an indication of the (un)steadiness of the cavitation and thus give an rough estimation of the cavitation type for each value of p_s. Moreover, a spectral analysis of the time series of the cavity bubble length during the simulation of each data point can be conducted as done in by Arndt et. al. [4]. This spectral analysis can then give an indication in what cavitation regime is produced by the

operating conditions in the simulation. In turn, an estimation of the transition from steady to unsteady cavitation can be made.

3.5. Polars

For the study of the polar loads in cavitating conditions, a series of simulations is carried out on for the followings angles of attack $\alpha = [0, 2, 4, 6, 8]$. This series of simulations is then conducted for the following cavitation numbers $\sigma = [1.6, 1.4, 1.35, 1.2, 1]$. The lift and drag coefficient, as well as the performance L/D are then reported in polar plots for the different polars per σ to be compared. The polars are also compared to experimental reference data from Leroux et. al. [20] and values obtained from potential flow solver *xFoil*.

4

Results & Discussion

In this chapter, all results are presented and discussed. First the non-cavitating and cavitating test cases are presented for the validation of the numerical models and the results are discussed. Furthermore, results from simulations of unsteady cloud cavitation conditions are presented. As this has not finally become part of the actual validation, this study has a separate section. With use of the validated models and CFD set up, the results from the method comparison of the cavitation analysis with cavitation model versus without cavitation model is presented and discussed. Then, the results from the stability analysis is presented and discussed and finally, the polar and efficiency studies are presented and discussed.

4.1. Test Case: Non-Cavitating

In this section the results from the simulations of the non-cavitating test case are presented. First the mesh convergence is presented and discussed, then the lift and drag polars and finally the pressure distributions and fields are shown and discussed.

4.1.1. Mesh Convergence

In table 4.1, some of the key solution quantities of the mesh convergence study are shown. The mesh scaling parameter, solver time, mesh elements, lift and drag coefficients and L/D are shown for the executed simulations of all mesh densities. Also added in the table are the result from the experimental data from Ladson [19] and the result from potential flow solver for comparison.

In figure 4.1 the total solver time, lift and drag coefficients are plotted as a function of the number of mesh elements .

Table 4.1: Mesh convergence output quantities in comparison with experiment and xFoil for NACA-0012 section at $\alpha = 10.12°$ for $Re = 5.93 \times 10^6$ and $M = 0.3$.

$\alpha = 10.12°$	Mesh Scaling	Cd	Cl	L/D	Solver Time (min)	Mesh Elements
	1.4	0.014039	1.10074	78.4058	4.13918	29003
	1.2	0.013428	1.10429	82.2379	4.42002	33319
	1	0.0131919	1.10552	83.8026	5.78125	39453
	0.8	0.0127835	1.10899	86.7518	7.56895	48750
	0.6	0.0126462	1.10959	87.7412	10.7118	63029
	0.4	0.0125571	1.11186	88.5441	20.0685	94433
Experiment (Ladson)		0.012	1.1251	95.78		
xFoil		0.01105	1.2234	110.70		

30

(a) Lift Coefficient

(b) Drag Coefficient

(c) Total Solver Time
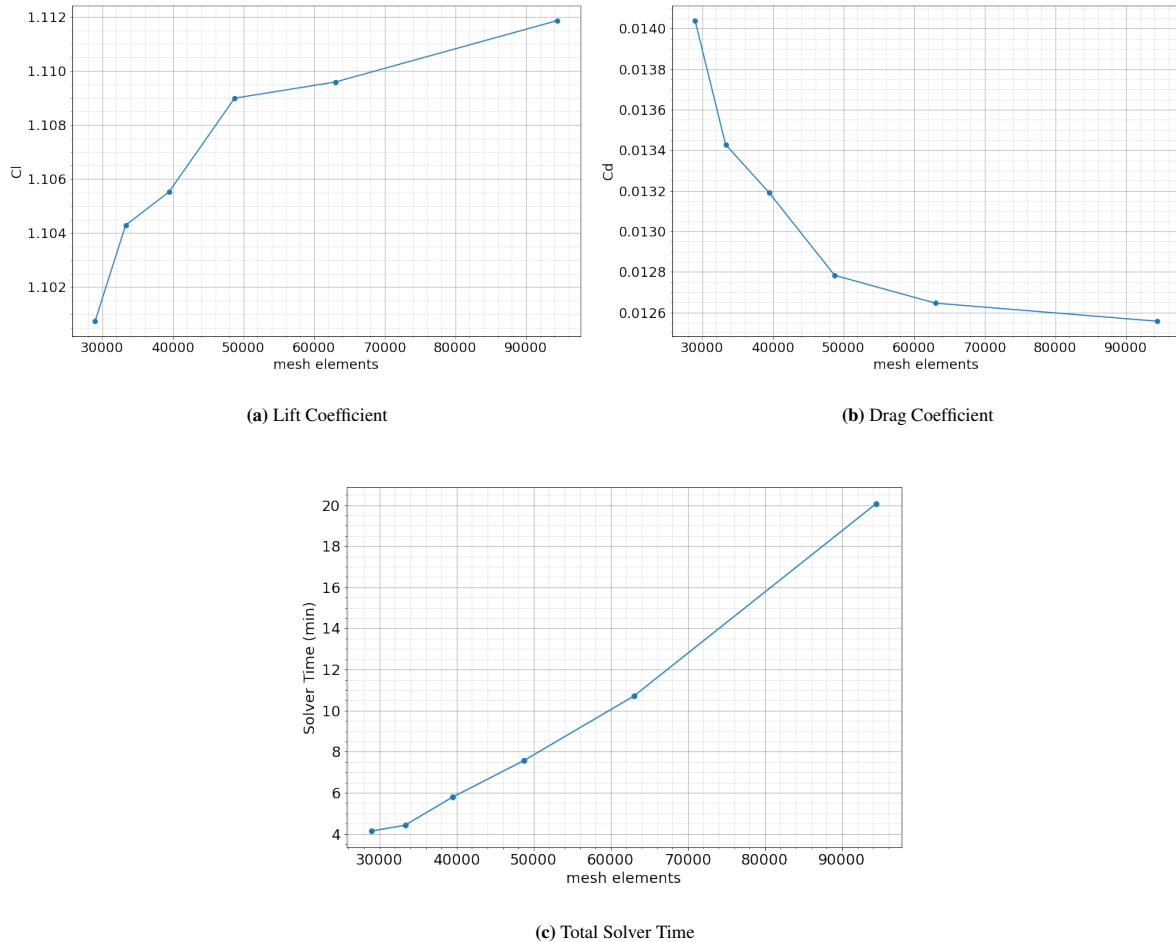
Figure 4.1: Mesh convergence quantities for the NACA-0012 section at $\alpha = 10.12°$, $Re = 5.93 \times 10^6$ and $M = 0.3$.

From results in table 4.1 an the plots in figure 4.1, it can be seen that the values for lift and drag coefficient converge as the number of mesh elements increases. Also, the total solver time increases significantly as the mesh elements. Considering the rate of convergence and the total solver time, the mesh scaled by $MS = 0.8$ is considered to be sufficiently accurate as the error in lift coefficient with the experimental value is about 1.4% and in drag coefficient around 6%. The error in lift and drag for the highest mesh density ($MS = 0.4$) is about 1.2% and 4%, which is a slight improvement over the mesh with $MS = 0.8$. However, the increase in computational time is 2.5 times higher. Hence, the mesh with $MS = 0.8$ is chosen.

4.1.2. Polars

The CFD simulation with $MS = 0.8$ is considered to be converged and thus this mesh density is used for further studies. In this section, the results for the polars are given. Figure 4.2 shows the lift and drag polars and the efficiency or L/D. The tables 4.2, 4.3 and 4.4 show the results for the lift, drag and pressure drag coefficients respectively. The results are compared with results from Ladson [19] and *xFoil* and their respective errors are given in the tables. In the polar plots, the lift and drag coefficients seem to be coherent with the experimental results from Ladson [19] in the linear region up to about $\alpha = 13°$. At higher angles of attack, the data from Ladson shows stall whereas this stalling is not captured in the current CFD study. This stall can also be seen in the drag coefficient polar as the drag strongly increases in the experimental data for about $\alpha > 13°$. Again, this increase is not captured by the current CFD study. In table 4.2, it can be seen that the error in the current CFD results with respect to the experimental data is smaller than 2% in the range for angle of attack $4° < \alpha < 12°$. As mentioned above, for higher values the CFD did not capture the stalling behaviour, hence the larger errors. The CFD measurement for $\alpha = -2.02°$ also shows a larger error of 7.12%, this can partially be explained by the fact that errors are larger for smaller values.

(a) C_L

(b) C_D

(c) L/D
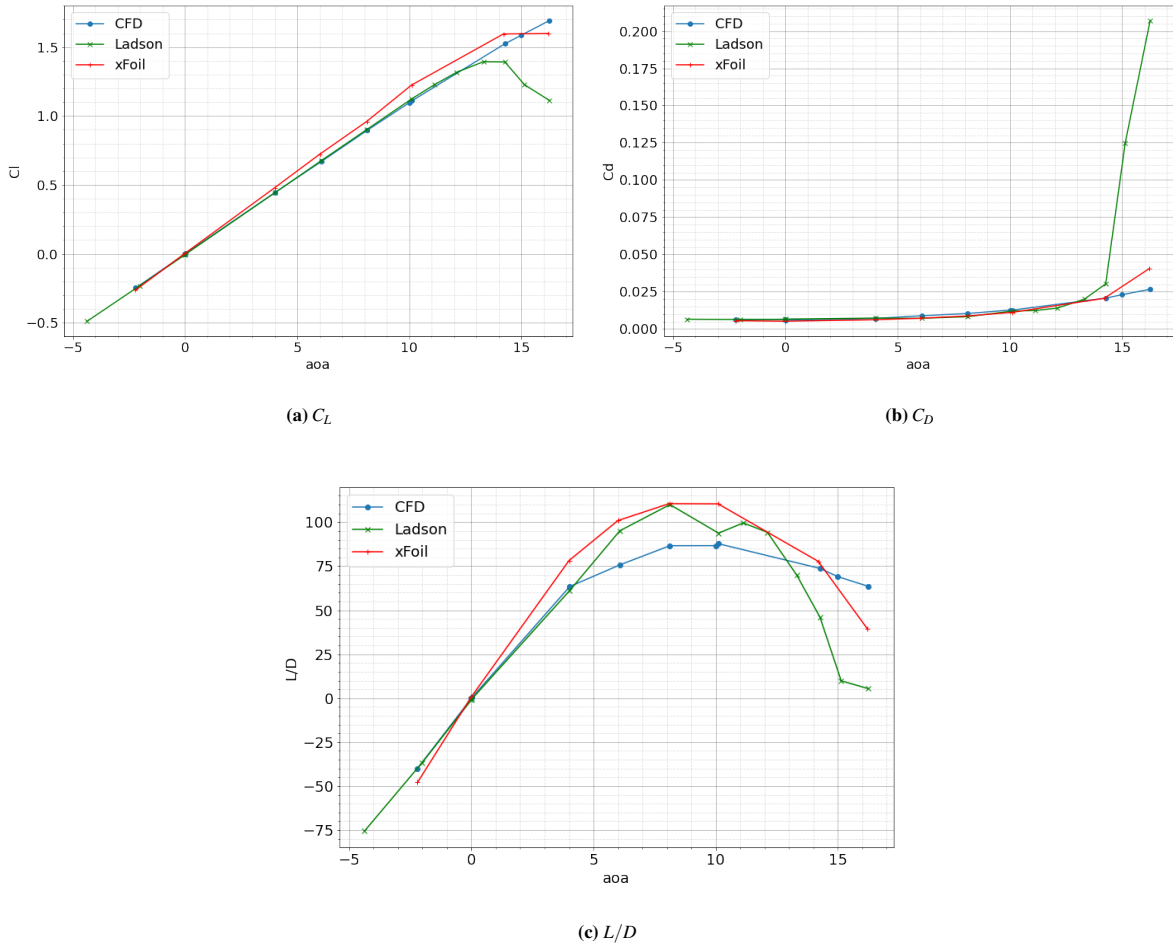
Figure 4.2: Polar Plots for the NACA-0012 section at $\alpha = 10.12°$, $Re = 5.93 \times 10^6$ and $M = 0.3$.

Table 4.2: Lift Coefficient: Results Comparison for the NACA-0012 section with $Re = 5.93 \times 10^6$ and $M = 0.3$.

α	CFD	Ladson	xFoil	Error Ladson (%)	Error xFoil (%)
-2.02	-0.2481	-0.2316	-0.2623	7.12	5.42
4.03	0.4529	0.4452	0.4794	1.73	5.53
6.08	0.6781	0.6762	0.7216	0.28	6.03
8.13	0.9011	0.9039	0.9597	0.32	6.11
10.12	1.1092	1.1251	1.2237	1.41	9.36
12.12	1.3140	1.3172	1.4265	0.25	7.89
14.27	1.5175	1.3917	1.5947	9.04	4.84
16.25	1.6765	1.1132	1.5992	50.60	4.83

Table 4.3: Drag Coefficient: Results Comparison for the NACA-0012 section with $Re = 5.93 \times 10^6$ and $M = 0.3$

α	CFD	Ladson	xFoil	Error Ladson (%)	Error xFoil (%)
-2.02	0.00558	0.0063	0.00543	11.43	2.76
4.03	0.00631	0.00728	0.00613	13.28	2.99
6.08	0.00799	0.00711	0.00715	12.33	11.70
8.13	0.00993	0.00822	0.00868	20.86	14.46
10.12	0.01241	0.012	0.01108	3.45	12.04
12.12	0.01593	0.01397	0.01437	14.06	10.88
14.27	0.02090	0.03023	0.02051	30.85	1.92
16.25	0.02755	0.20698	0.04036	86.69	31.75

Table 4.4: Pressure Drag Coefficient: Results Comparison for the NACA-0012 section with $Re = 5.93 \times 10^6$ and $M = 0.3$

α	CFD	xFoil	Error xFoil (%)
-2.02	0.00112543	0.00093	21.01
4.03	0.00175803	0.00161	9.19
6.08	0.00315054	0.00276	14.15
8.13	0.00512198	0.0044	16.41
10.12	0.00812373	0.00687	18.25
12.12	0.0118054	0.01045	12.97
14.27	0.0170235	0.01718	0.91
16.25	0.0241165	0.03796	36.47

4.1.3. Pressure Coefficient

Figure 4.3 shows the pressure coefficient distribution along the surface and the pressure field for $\alpha = 0°$ in 4.3a and 4.3b, for $\alpha = 10°$ in 4.3c and 4.3d and for $\alpha = 15°$ in 4.3e and 4.3f. The overall shapes of the C_p distributions are coherent with the experimental data by Ladson. However, the low pressure pressure on the suction side seem to be slightly overestimated by the current CFD study compared to the experimental data from Ladson, i.e. the current CFD results show slightly lower negative values. This difference is visibly largest for $\alpha = 15°$, which is coherent with the earlier found results in the polar study in previous section.

In general, the results of the current CFD simulations are in good agreement with the reference data within the relevant range angles of attack, that is up to about $\alpha = 10°$. This CFD simulation set up for non cavitating flow can now be used as a base for the following test case, the CFD simulation for cavitating flow.
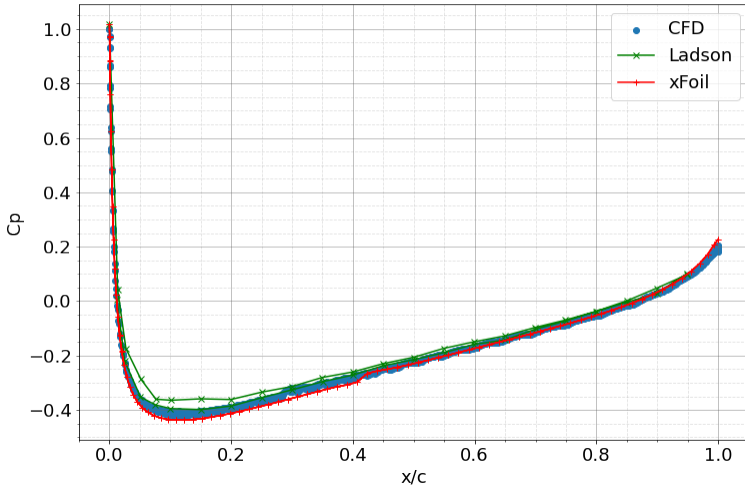
(a) $\alpha = 0°$: Comparison of C_p over section surface.
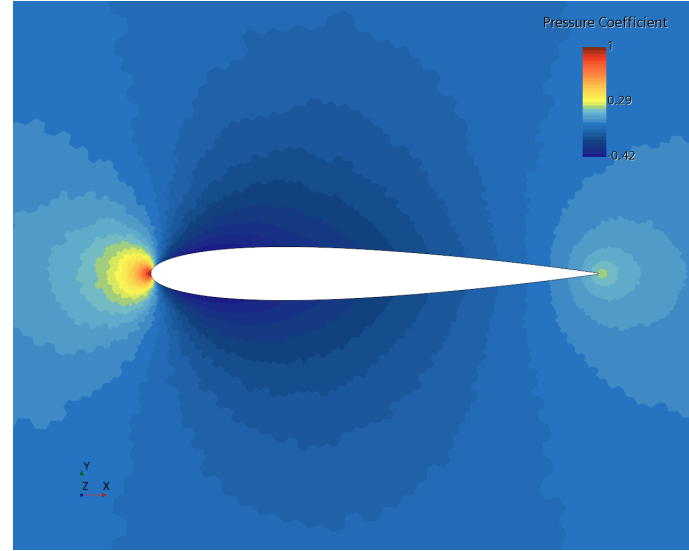
(b) $\alpha = 0°$: C_p Field around the Foil
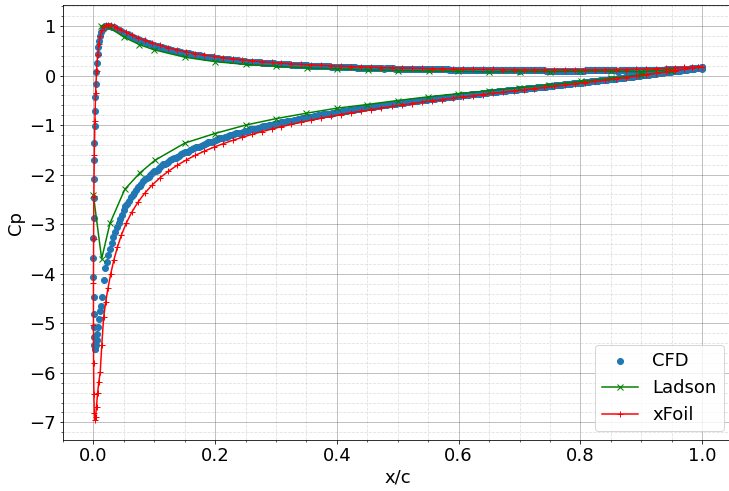
(c) $\alpha = 10°$: Comparison of C_p over section surface.
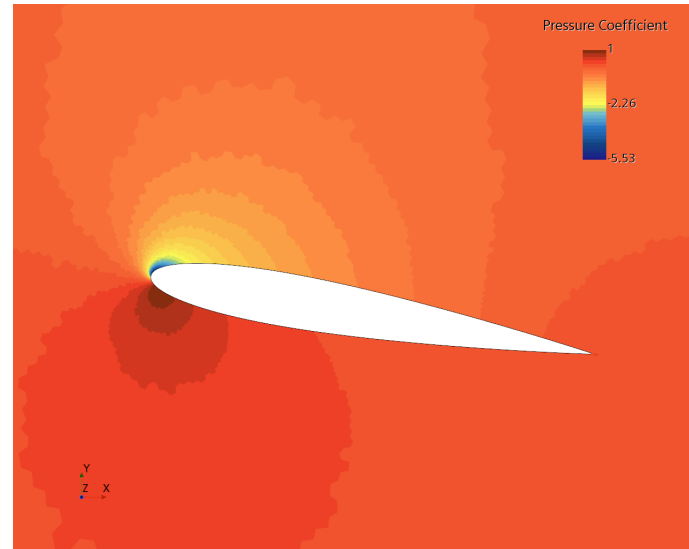
(d) $\alpha = 10°$: C_p Field around the Foil
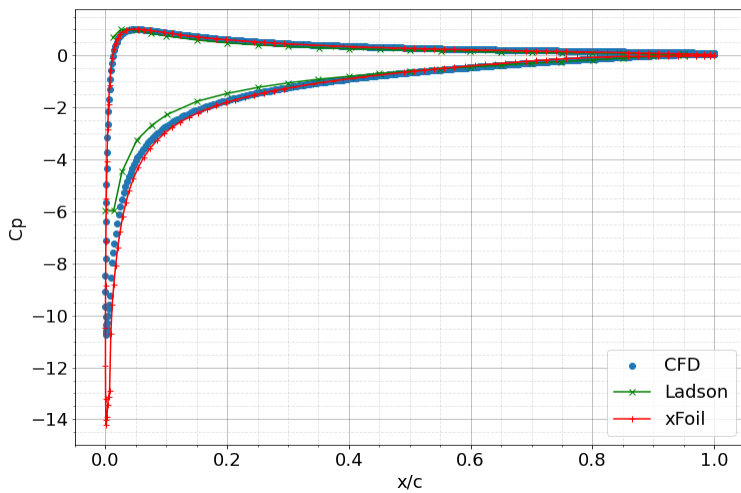
(e) $\alpha = 15°$: Comparison of C_p over section surface.
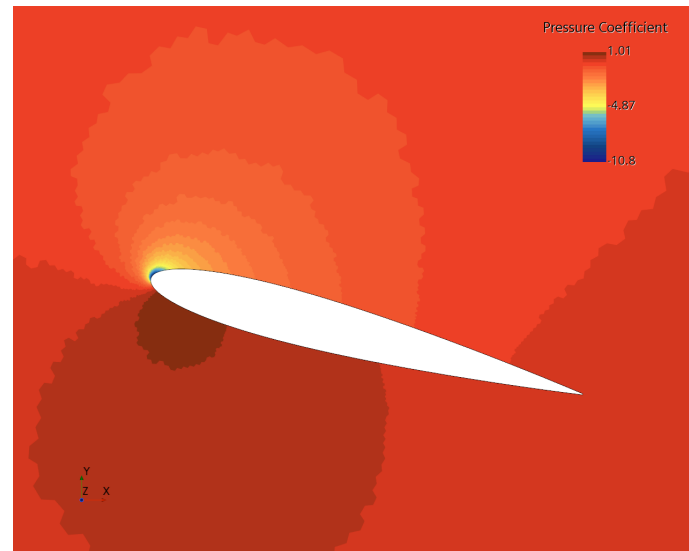
(f) $\alpha = 15°$: C_p Field around the Foil

Figure 4.3: Pressure Coefficient Results for the NACA-0012 section with $Re = 5.93 \times 10^6$ and $M = 0.3$ at $\alpha = 0°, 10° and 15°$

4.2. Test Case: Cavitating

In this section, the results for the validation of the cavitating test case are presented. First the mesh convergence is reported and discussed. Next, the time-step and turbulence models studies are presented and discussed. Finally, the results from the turbulent viscosity modification study is presented and discussed.

4.2.1. Mesh Convergence

In figure 4.4 some of the key quantities of the mesh convergence results are shown. The convergence of the mean lift and drag is plotted (with the root mean square indicated with error-bars) as function of the number of mesh elements in figures 4.4a and 4.4b respectively. Figure 4.4c shows the relative errors in the mean lift and drag coefficients with respect to the mean result obtained with the highest number of mesh elements. Figure 4.4d shows the total solver time in hours as a function of the number of mesh elements. Table 4.5 shows an overview of the mesh convergence results. It can be seen that the errors in lift and drag coefficients for the mesh scaling 1.2 and 1 are all higher than 3%. For the mesh scaled by 0.8 the error in C_L drops to 1.1% and the error in C_D to 0.4%. As the mesh is scaled by 0.6 the errors in C_L and C_D are 0.1% and 0.2% respectively.

(a) Lift Coefficient

(b) Drag Coefficient

(c) Relative errors in C_L and C_D
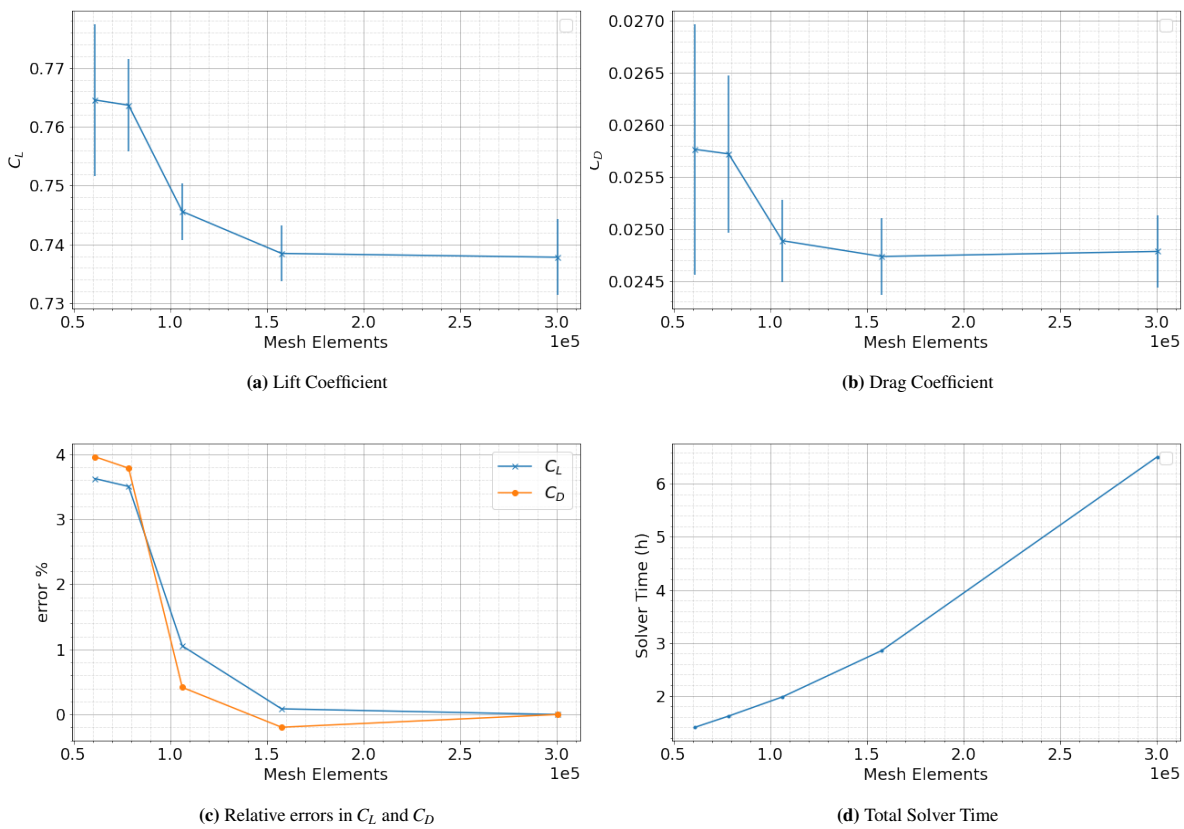
(d) Total Solver Time

Figure 4.4: Convergence quantities as a function of mesh elements: $\alpha = 6.5°$, $\sigma = 1.4$, $Re = 8 \cdot 10^5$

Table 4.5: Mesh Convergence Quantities Table

Mesh Scaling	Mesh Elements	mean C_L	rms C_L	mean C_D	rms C_D	error C_L [%]	error C_D [%]	Total Solver Time (h)
0.4	300268	0.738	0.00644	0.0248	0.00035	0	0	6.5
0.6	157633	0.738	0.00469	0.0247	0.00037	0.1	-0.2	2.9
0.8	106284	0.746	0.00480	0.0249	0.00040	1.1	0.4	2.0
1	78532	0.764	0.00790	0.0257	0.00076	3.5	3.8	1.6
1.2	61189	0.765	0.01293	0.0258	0.00121	3.6	4.0	1.4

As expected, the error in lift and drag decreases and the total solver time increases as the number of elements increase. The simulations with mesh scaling 1 and 1.2 both have a solver time around 1.5 hours while still having an error in lift and drag coefficient higher than 3%. For a mesh scaling of $MS = 0.8$, the solver time only increases by 25% while the gain in the lift coefficient is about 70%, with an even larger gain drag coefficient. For the mesh scaling of $MS = 0.6$, the solver time increases by about 45% and while the gain in C_L and C_D are significant (relative gain is large because of the small values), the loss in solver time outweighs the gain in C_L and C_D. Moreover, the relative errors for $MS = 0.8$ already are within acceptable margins and the simulation time needs to be as short as possible if this simulation will be run for large series of runs. The dimensionless wall distance $Y+$ is shown in figure 4.5 to demonstrate that the $y+$ value falls below 1 over the whole section surface. With a small peak at the leading edge at 0.8, the dimensionless wall distance satisfies the condition $Y+ < 1$ to capture the viscous sub layer. With these considerations in mind, the simulation with mesh scaling $MS = 0.8$ is considered to be sufficiently converged. This mesh density will be used for the following simulations.
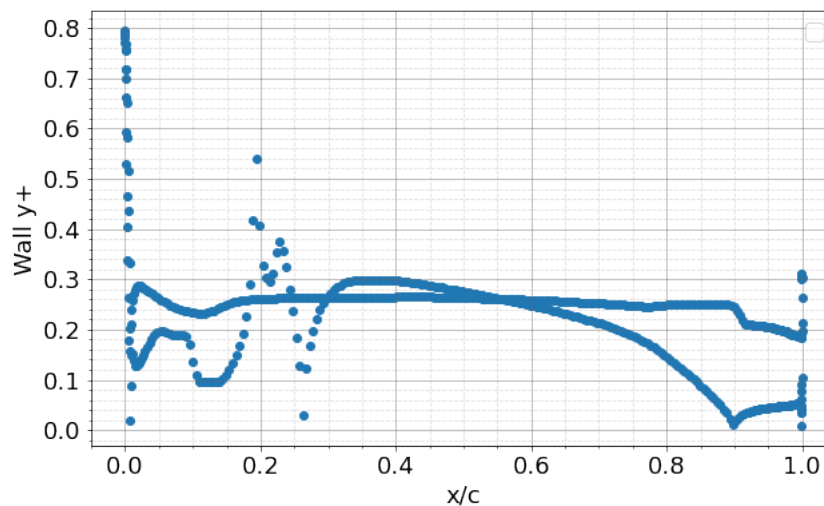
Figure 4.5: Wall y+ along the hydrofoil surface for the base mesh scaled by 0.8.

Now comparing the pressure distribution results from current mesh convergence study with reference values, figure 4.6 shows the pressure coefficient results for the NACA-66(mod) at $\alpha = 6.5°$ with $\sigma = 1.4$ for the mesh scaled by 0.4 and 1.2 compared to the experimental reference values form Leroux [20] and Seo [32]. The sudden drop in pressure distribution of our current CFD mesh convergence studies at around $x/c = 0.2$ indicates the end of the cavitation bubble. The constant pressure up to the leading edge is at the level of the saturation vapor pressure. However, the pressure distribution of the finest mesh scaled by 0.4 does not correspond well with the reference values. In fact, the mean lift coefficient according to the experimental values by Leroux give a value of 0.852, which gives the results from most refined mesh an error of about 13% for the lift coefficient. Also, the relative cavitation bubble length l/c given by the results of Leroux give a value of $l/c = 0.29$ compared to $l/c = 0.21$ for the current CFD simulation results with mesh scaling 0.4, corresponding to an error of about 27%.
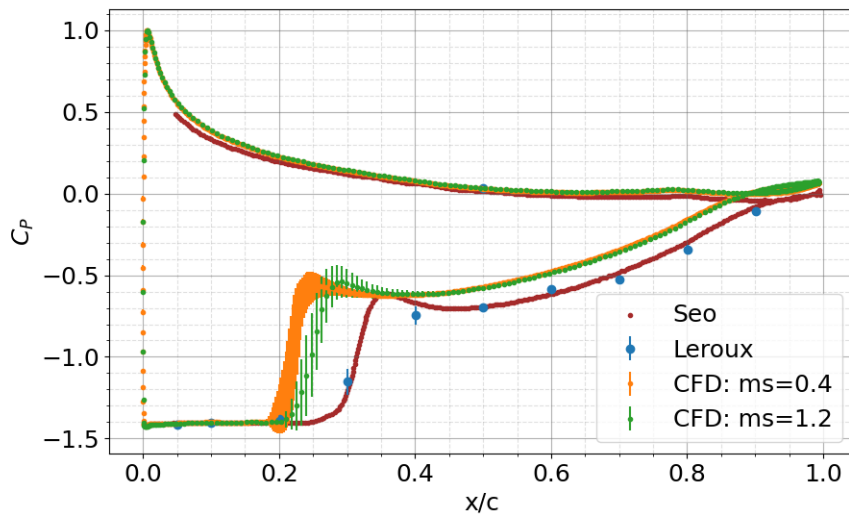
Figure 4.6: Pressure distribution of NACA-66(mod) at $\alpha = 6.5°$ with $\sigma = 1.4$ with the finest and most coarse mesh from the mesh convergence study compared to the experimental reference values from Leroux and the numerical validation from Seo.

Although the mesh convergence study finds a clearly converged solution, the results obtained do not agree with the with the experimental reference values of Leroux and the numerical reference values from Seo [32]. From these results, it is clear that more simulation parameters should be studied in order to validate the simulation set-up.

4.2.2. Time Step

In order to study the influence of the time step size on the simulation results with the implemented Schnerr-Sauer cavitation model, the simulation results for initial time step $dt = t_0/200$ is compared with results from simulations with time steps $dt = t_0/400$ and $dt = t_0/800$.

The pressure coefficient will again be compared since this discrepancy between the reference values and the CFD results from current study. Figure 4.7 shows the pressure distribution results for the time steps $dt = [t_0/200, t_0/400, t_0/800]$ as well as the experimental pressure distribution values from Leroux and the numerical validation from Seo.

It can be seen that the pressure distribution curve for the CFD results of the compared time steps are practically identical. As a result, the lift and drag are also identical for each time step size. Since no difference is measured, it can be concluded that the solution already has converged at time step $dt = t_0/200$ and that increasing the time resolution further does not have an influence on the solution at the base time step. More simulation parameters need to be studied in order to validate the simulation set up.
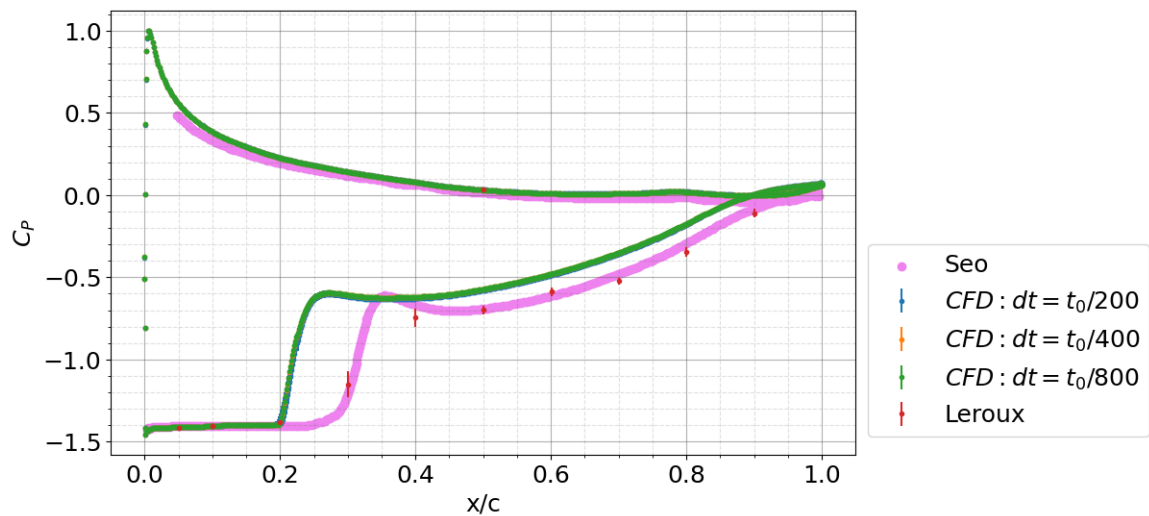
Figure 4.7: Pressure distribution of NACA-66(mod) at $\alpha = 6.5°$ with $\sigma = 1.4$ for time steps $dt = [t_0/200, t_0/400, t_0/800]$ and reference values from Leroux and Seo.

4.2.3. Turbulence Models

Next, the influence of the different turbulence models is investigated. The initial mesh convergence study presented in previous sections is executed with the SST turbulence model. The turbulence models which are considered in this comparison are the SST, the SA and $k - \omega$ turbulence models. The $k - \varepsilon$ turbulence model is not considered in this comparison since the properties of this model are included in the SST model for the exterior flow. Hence the development and dynamics of the cavitation bubble will not change much with respect to the simulation with an SST turbulence model.

In figure 4.8, the pressure distribution results for the different turbulence models are presented in comparison with the experimental pressure distribution values from Leroux and the numerical validation from Seo. It can be seen that the pressure stays at the saturation pressure about 0.015 further downstream chordwise along the suction side for the SA model compared to the SST, meaning the cavitation bubble is about 1.5% longer. For the $k - \omega$ model, the pressure stays a fraction longer at the saturation pressure, indicating a cavitation bubble that is a little bit longer. However, the results for neither models approach the reference values within acceptable margins for validation. Further simulation parameters need to be studied in order to validate the simulation set up. As no significant improvement is achieved using any of the turbulence models, the turbulence model in further studies is chosen based on relevant literature published within the last 15 years [27] [22] [38]. These studies the *SST* model is used, thus this turbulence model is also used in further studies.
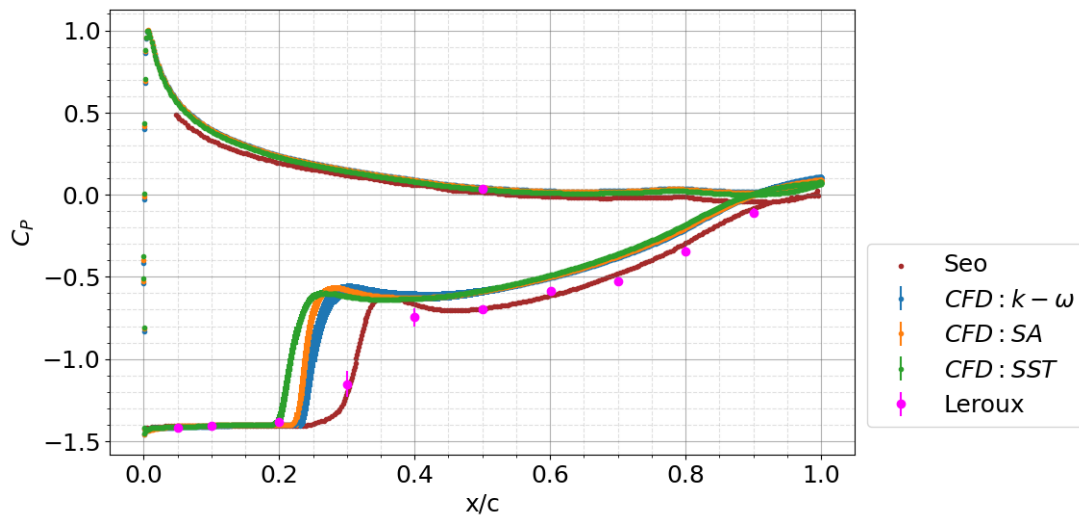
Figure 4.8: Pressure distribution of NACA-66(mod) at $\alpha = 6.5°$ with $\sigma = 1.4$ for different turbulence models and reference values from Leroux and Seo.

4.2.4. Turbulent Viscosity

In this section, the results for different values of the turbulent viscosity exponent n (see 3.2.5) are presented and discussed.

Turbulent viscosity exponent $n = 3$

The results for the proposed value of the turbulent viscosity exponent $n = 3$ by Tran et. al. [38] are presented and discussed in this section. In figures 4.9, the time series of the bubble size and the lift coefficients during the simulation are shown. It can be seen that the both quantities show strong peaks and pulses from about 2.5 seconds resulting in a very noisy signal and a large root mean square.

(a) Maximum cavity length l/c as a function of physical time (s).

(b) Lift coefficient C_L as a function of physical time.
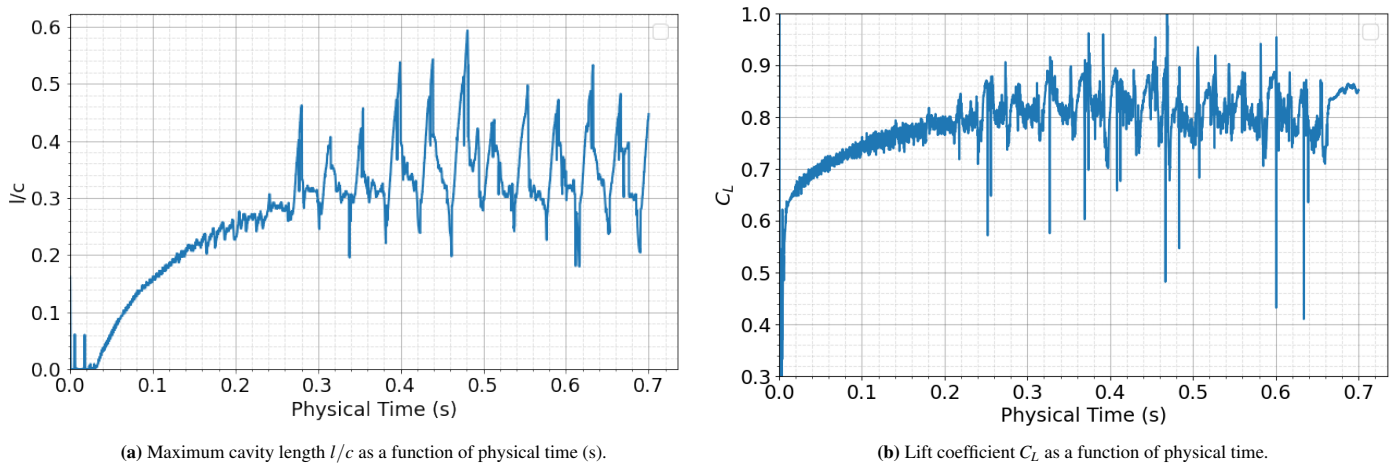
Figure 4.9: Convergence of the maximum cavity length and lift coefficient during the course of the simulation for the NACA-66(mod) at $\alpha = 6.5°$, $Re = 8 \times 10^5$ and $\sigma = 1.4$ for turbulent viscosity exponent $n = 3$.

In figure 4.10 the pressure distribution is shown where the mean C_P values and the root mean square are indicated in comparison with the reference values from Leroux [20] and Seo [32]. The drop in the mean value at the suction side of the pressure distribution coincides with the drop in the reference values. However, above $x/c = 0.4$ the mean value on the suction side is higher than the reference values. Also, the root mean square shows very large values along the along most of the hydrofoil surface, especially on the suction side at the pressure drop where the cavitation bubble ends. These high values in the root mean square are consistent with the peaks in the bubble length l/c in figure 4.9a. As mentioned in the methodology, note that the bubble length l/c is defined as the maximum value along the x-axis in the hydrofoil reference frame of the mesh elements with a vapor volume fraction above 0.5 (see 3.2.6).

Figure 4.10: Pressure distribution over the NACA-66(mod) at $\alpha = 6.5°$, $Re = 8 \times 10^5$ with $\sigma = 1.4$ for turbulent viscosity exponent $n = 3$ compared with the reference values from Leroux [20] and Seo [32].

Figure 4.11 show the mean converged values of the bubble length l/c, lift coefficient C_L and drag coefficient C_D as a function of the cavitation number for $\sigma = [1.29, 1.35, 1.4]$. The current CFD results are compared with results form the reference studies from Leroux [20] and Seo [32]. The mean values and root mean square are taken from the sample set of values from 0.5 to 0.7 seconds of physical time. The mean values of the quantities are not far off from the reference values. However, the large root mean square in the values indicate that the converged state shows significant unsteady behaviour.
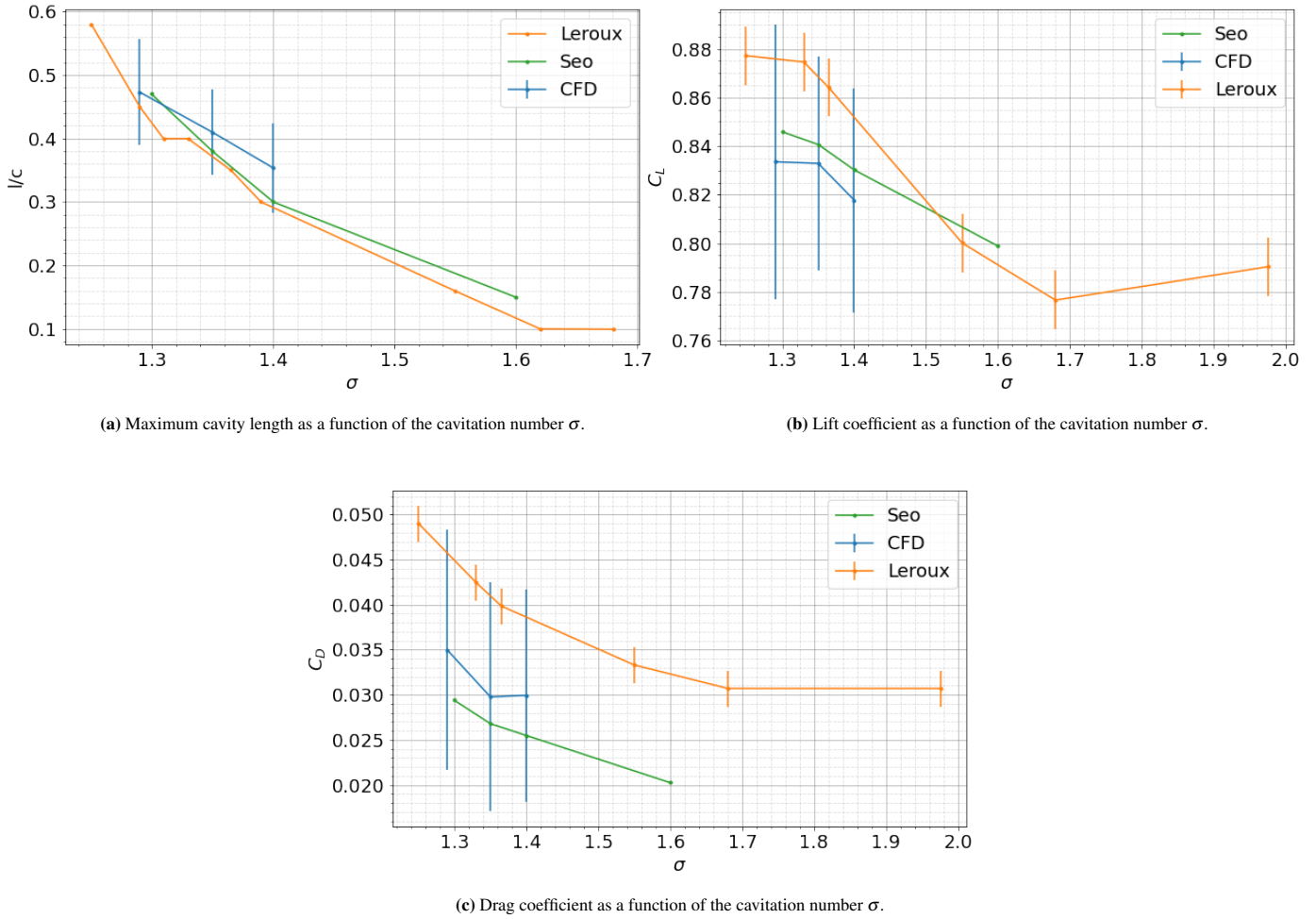
(a) Maximum cavity length as a function of the cavitation number σ.

(b) Lift coefficient as a function of the cavitation number σ.

(c) Drag coefficient as a function of the cavitation number σ.

Figure 4.11: Maximum cavity length, lift and drag coefficients as a function of sigma compared to reference values from Leroux [20] and Seo [32] for the NACA-66(mod) at $\alpha = 6.5°$, $Re = 8 \times 10^5$ with turbulent viscosity exponent $n = 3$. The mean and root mean square values are calculated from the time step samples from 0.5 to 0.7 seconds.

During the course of the simulation, images of the volume fraction field and absolute pressure field around the hydrofoil are exported to give insights on the cavitation dynamics and general behaviour. In figures 4.12 and 4.13 the vapor volume fraction and absolute pressure fields are shown during one of the peaks to be seen in 4.9a between 4.1 and 4.4 seconds for $\sigma = 1.4$. It can be seen that the end of the cavitation bubble shows some light pulsating behaviour. These small pulsations cause perturbations in the pressure field as can be seen in figure 4.13 which explains the peaks in the lift coefficient and the large root mean square values in the pressure coefficient distribution.

The value of exponent n has a significant impact on the behaviour of the cavitation bubble and the stability of the bubble dynamics. In the following sections, various values of n will be examined to investigate its impact on the cavitation behavior and determine the appropriate value that yields valid results.
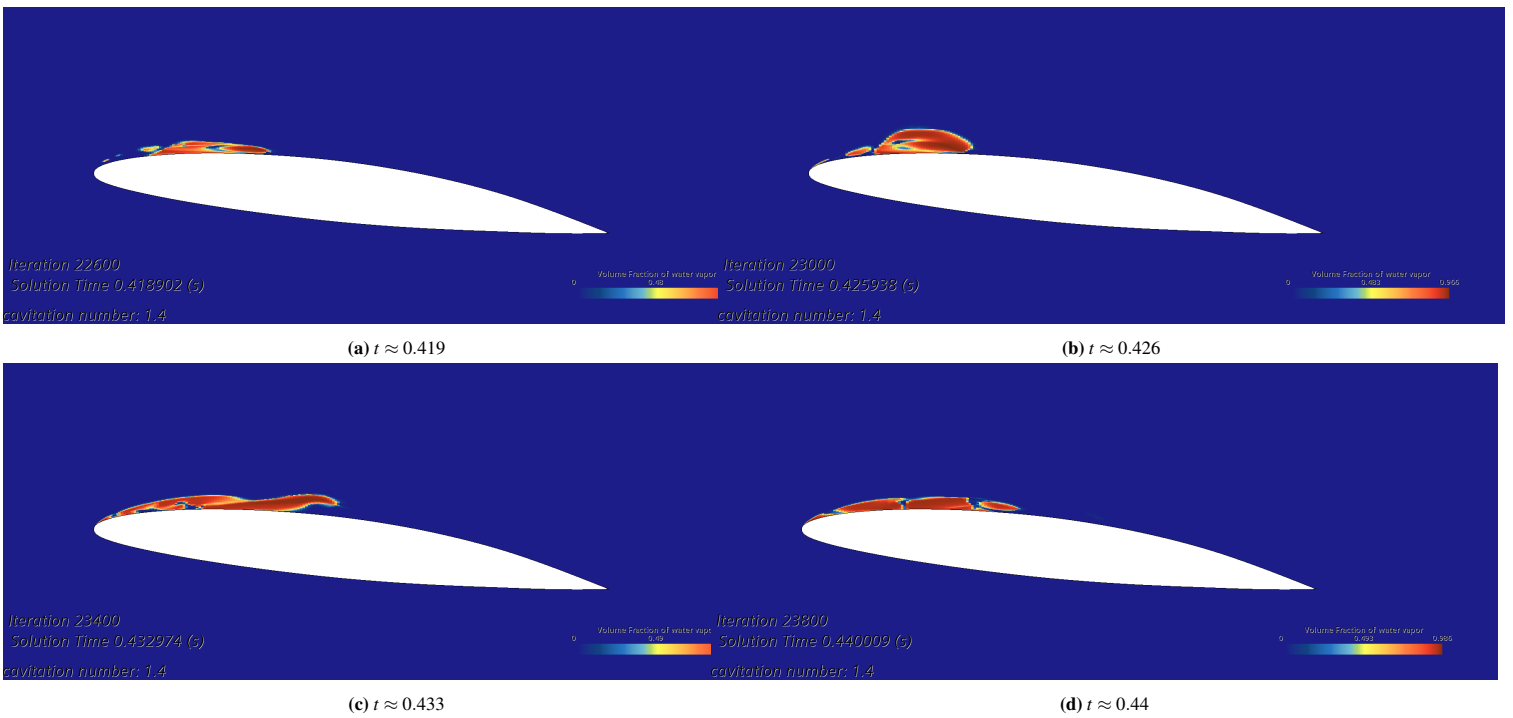
Figure 4.12: Images of the vapor volume fraction at times $t \approx [0.419, 0.426, 0.433, 0.44]$ around the NACA-66(mod) at $\alpha = 6.5°$, $Re = 8 \times 10^5$ with $\sigma = 1.4$ for turbulent viscosity exponent $n = 3$ showing the instability in the cavitation bubble.
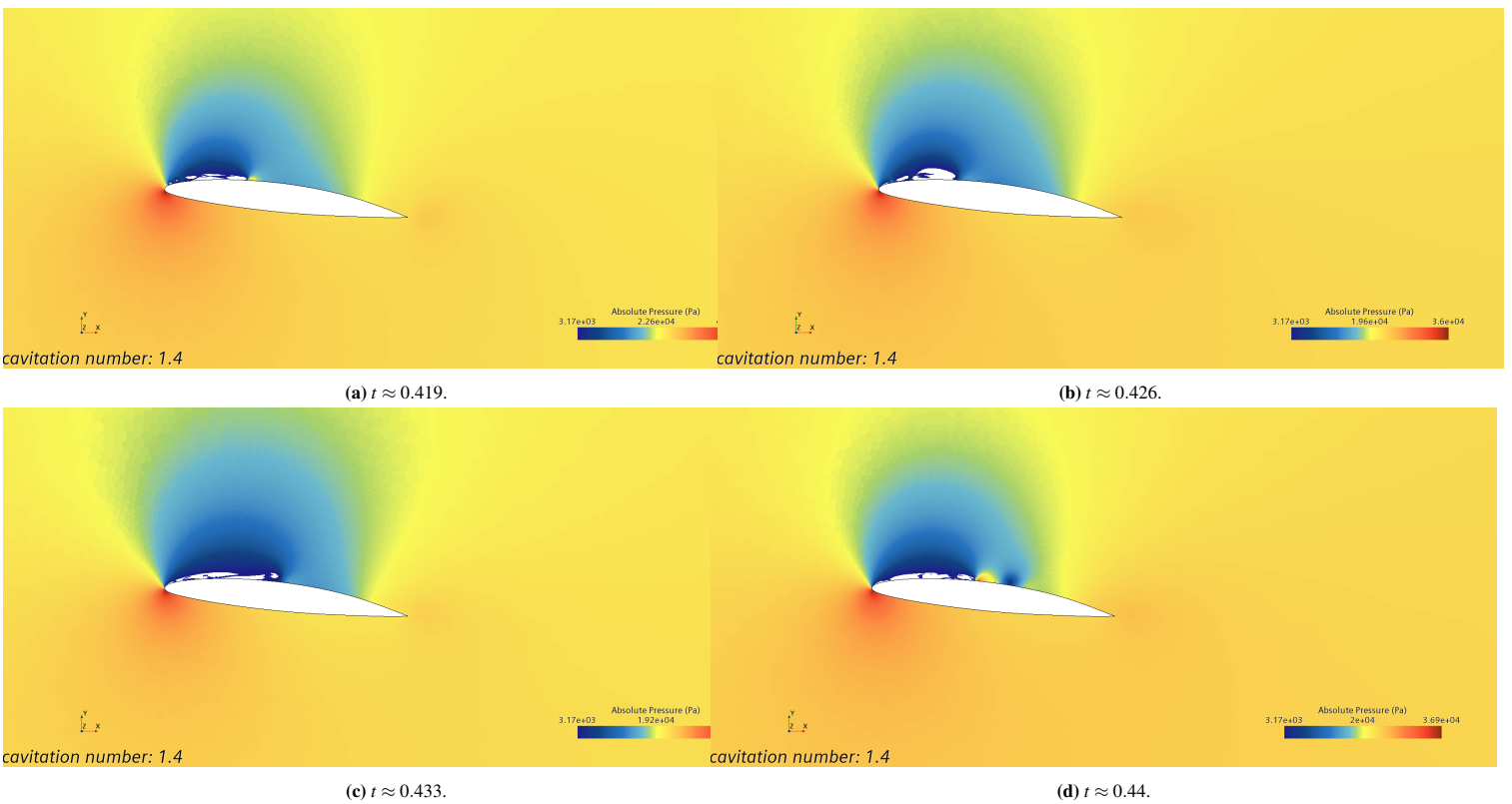
Figure 4.13: Images of the pressure field times $t \approx [0.419, 0.426, 0.433, 0.44]$ over the NACA-66(mod) at $\alpha = 6.5°$, $Re = 8 \times 10^5$ with $\sigma = 1.4$ for turbulent viscosity exponent $n = 3$ showing instability in the cavitation bubble. A minimum pressure is added to the pressure field such that pressure regions for which $p < p_v$ is indicated in white.

Effects of lowering the exponent to $n = 2$

In this section, the simulation results for the turbulent viscosity modification with parameter $n = 2$ are presented and discussed.

Figure 4.14 shows the time series of the cavity length l/c (a.) and the lift coefficient C_L (b.) during the course of the simulation. The signals of the bubble length and lift coefficient show a much more smooth convergence than for the simulation with turbulent viscosity exponent $n = 3$. Moreover, the pressure coefficient distribution in figure 4.15 does not show the very large root mean square around the mean values compared with the results for $n = 3$. This smoother behaviour suggests that the stability of the cavity has increased and that no more severe pulsations are present. However, the drop in the pressure coefficient tends slightly more towards the leading edge with respect to the reference values, which suggests that the CFD predictions still slightly underestimate the length of the cavitation bubble.

(a) Maximum cavity length l/c as a function of physical time (s).

(b) Lift coefficient C_L as a function of physical time.

Figure 4.14: Convergence of the maximum cavity length and lift coefficient during the course of the simulation for the NACA-66(mod) at $\alpha = 6.5°$, $Re = 8 \times 10^5$ and $\sigma = 1.4$ for turbulent viscosity exponent $n = 2$.
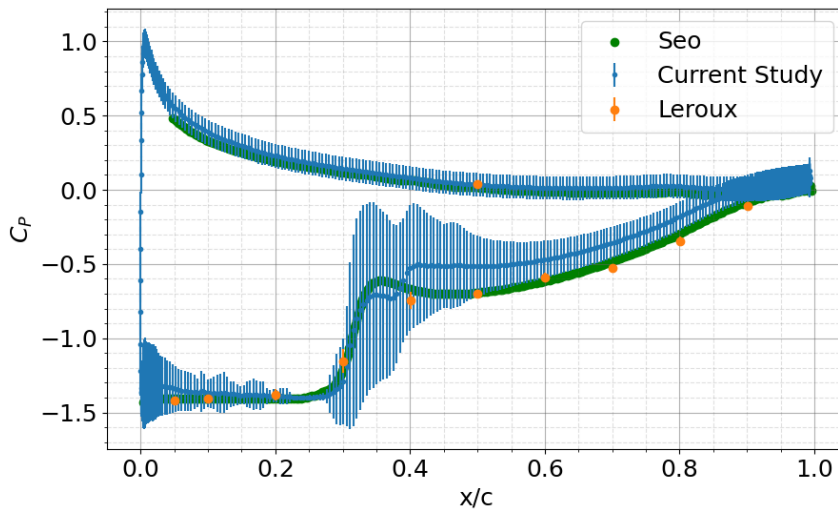

Figure 4.15: Pressure distribution over the NACA-66(mod) at $\alpha = 6.5°$, $Re = 8 \times 10^5$ with $\sigma = 1.4$ for turbulent viscosity exponent $n = 2$ compared with the reference values from Leroux [20] and Seo [32].

Figure 4.16 shows the mean converged values of the bubble length l/c, lift coefficient C_L and drag coefficient C_D as a function of the cavitation number for $\sigma = [1.29, 1.35, 1.4]$. Again, the current CFD results are compared with results form the reference studies Leroux [20] and Seo [32] and the mean values and root mean square are taken from the sample set of values from 0.5 to 0.7 seconds of physical time.

The root mean squares of the values are much smaller than for the simulations with $n = 3$ which is coherent with the observations of the increased stability of the cavity bubble. Furthermore, in figure 4.16a the current CFD results seem to be consistently underestimating the cavity bubble length l/c. In table 4.6 the error percentages of the CFD results with respect to the experimental reference values from Leroux [20] are given. For a cavitation number of 1.29, 1.35 and 1.4 the relative errors are about 18%, 15.7% and 6.9% respectively (the signs before the percentages are left in the table to easily see whether the values over or underestimate the reference values). Looking at figure 4.16b and 4.16c, it can be seen that the lift and drag coefficient values as a function of the cavitation number are also significantly underestimated. For the lift coefficient, the relative errors with respect to the reference values for a cavitation number of 1.29, 1.35 and 1.4 are 9.5%, 9.5% and 8.6% respectively (see table 4.6). For the drag coefficient, the relative error percentages with respect to the reference values for a cavitation number of 1.29, 1.35 and 1.4 are 36.6%, 33% and 32.4% respectively.

Based on these results we conclude that the predictions provided by the model are not withing acceptable error margins. Hence, the value for the turbulent viscosity exponent n is further adjusted and studied.

(a) Maximum cavity length as a function of the cavitation number σ.

(b) Lift coefficient as a function of the cavitation number σ.
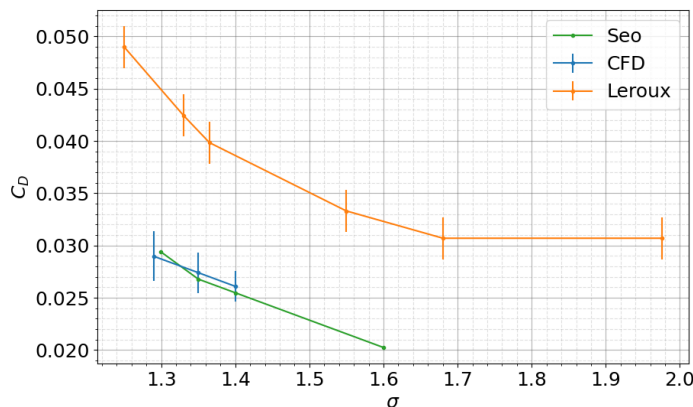
(c) Drag coefficient as a function of the cavitation number σ.

Figure 4.16: Maximum cavity length, lift and drag coefficients as a function of sigma for the NACA-66(mod) at $\alpha = 6.5°$, $Re = 8 \times 10^5$ and turbulent viscosity exponent $n = 2$ compared with reference values from Leroux [20] and Seo [32]. The mean and root mean square values are calculated from the time step samples from 0.5 to 0.7 seconds.

Table 4.6: Error percentages for l/c, C_L and C_D for the NACA-66(mod) at $\alpha = 6.5°$, $Re = 8 \times 10^5$, $\sigma = 1.4$ and turbulent viscosity exponent $n = 2$ with respect to reported values from Leroux.

σ	1.29	1.35	1.4
l/c	-18	-15.68	-6.90
C_L	-9.47	-9.45	-8.57
C_D	-36.62	-33.01	-32.38

Optimized turbulent viscosity exponent $n = 2.3$

As discussed in the results for exponent $n = 3$ (see section 4.2.4), the length of the cavitation bubble is increased which is desirable with respect to the reference data. However, the cavitation bubble also becomes unstable which does not reflect the reference data. For the exponent $n = 2$ (see section 4.2.4), the instability is gone but the cavity length and lift coefficient are still underestimated by an unacceptable margin. A few, simulations with the exponent n between 2 and 3 have been tried with $n = 2.3$ having the best results between having a stable cavitation bubble and being in agreement with the reference values. In this section, the simulation results for the turbulent viscosity modification with parameter $n = 2.3$ are presented and discussed.

Figure 4.17 shows the convergence of the cavity length l/c (a.) and the lift coefficient C_L (b.) during the course of the simulation. The signals of the bubble length and lift coefficient show a smooth convergence just like the simulation with turbulent viscosity parameter $n = 2$. Also, the pressure coefficient distribution in figure 4.18 does not show the very large root mean square around the mean values compared with the results for $n = 3$. This smooth behaviour suggests that the cavity bubble is stable and does not pulsate. Moreover, the drop in the pressure coefficient coincides with the pressure drop from the reference values.

(a) Maximum cavity length l/c as a function of physical time (s).

(b) Lift coefficient C_L as a function of iteration.

Figure 4.17: Convergence of the maximum cavity length and lift coefficient during the course of the simulation for the NACA-66(mod) at $\alpha = 6.5°$, $Re = 8 \times 10^5$ and $\sigma = 1.4$ for turbulent viscosity exponent $n = 2.3$.
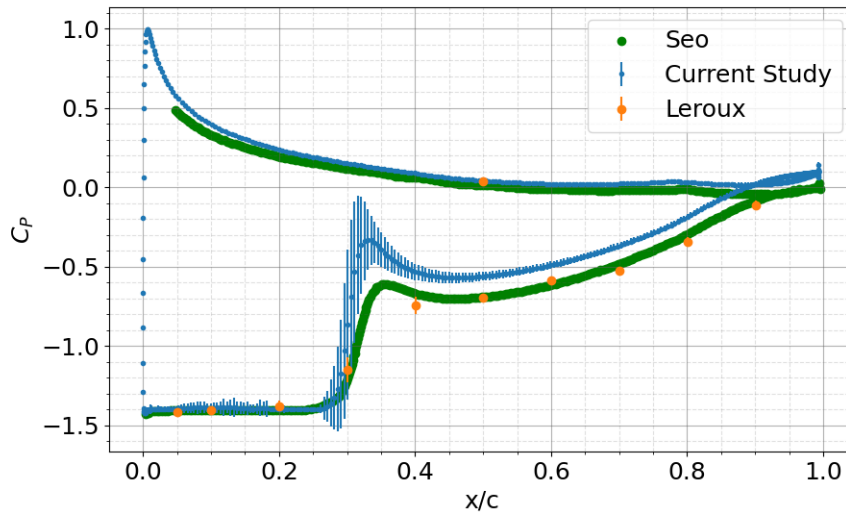
Figure 4.18: Pressure distribution over the NACA-66(mod) at $\alpha = 6.5°$, $Re = 8 \times 10^5$ and $\sigma = 1.4$ for turbulent viscosity exponent $n = 2.3$ compared with the reference values from Leroux [20] and Seo [32].
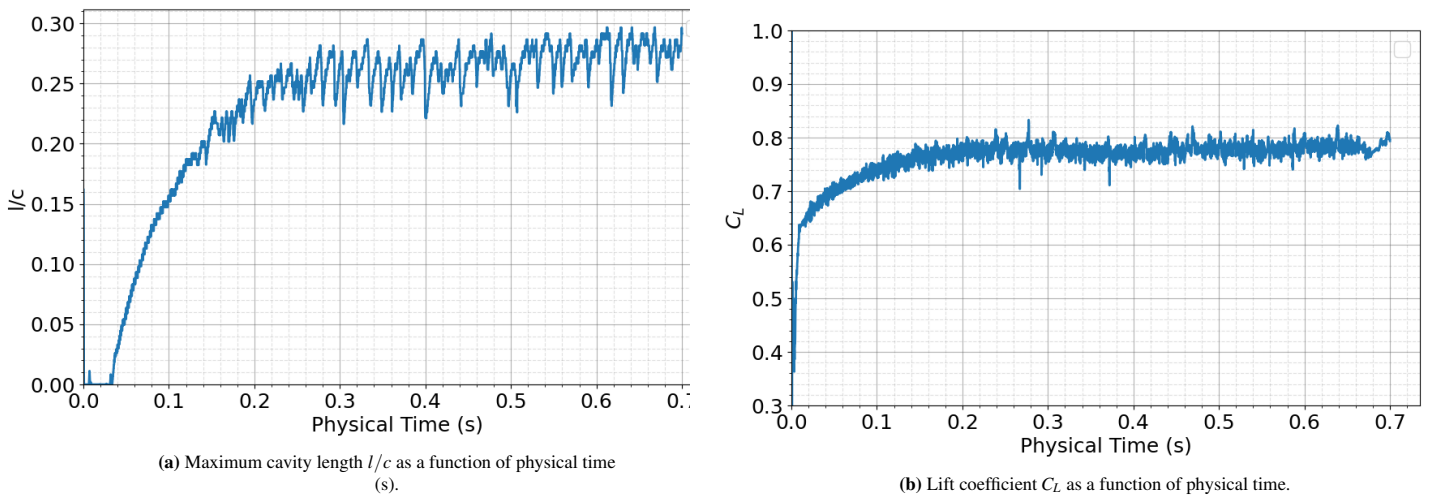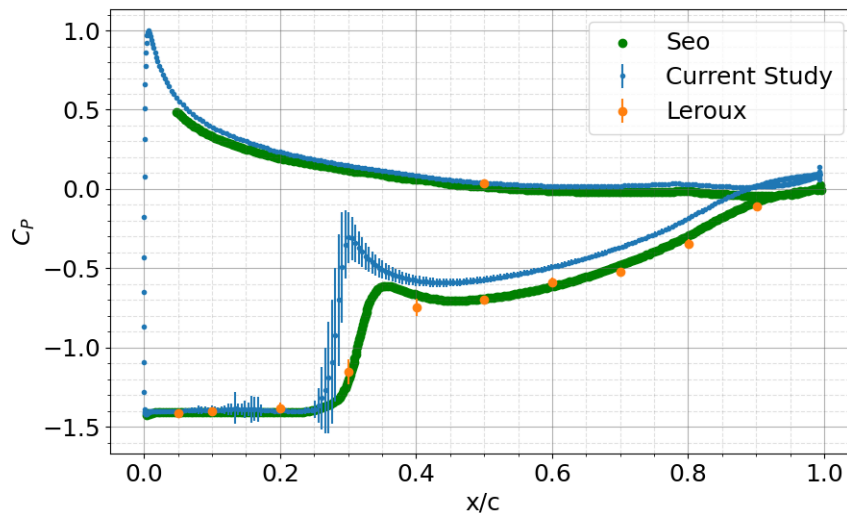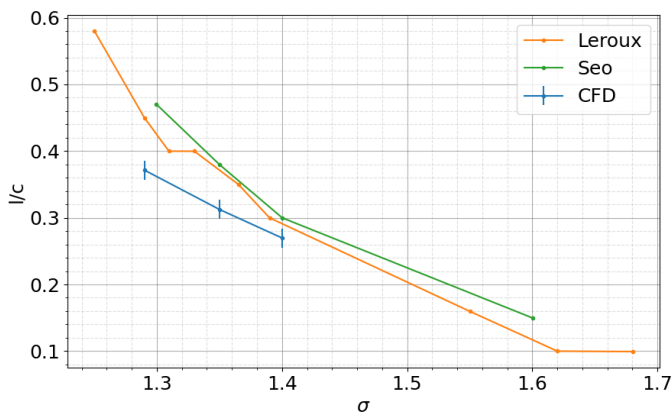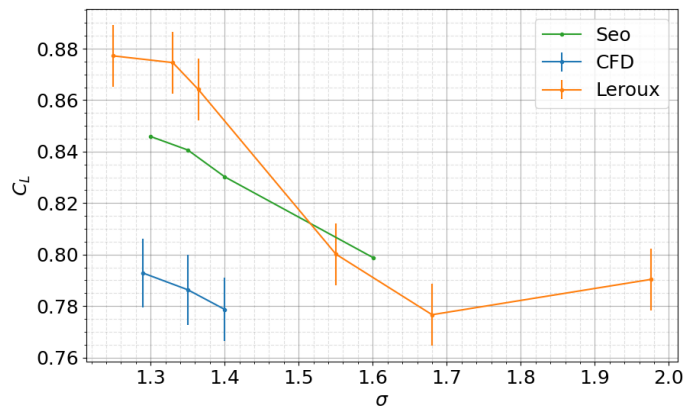
Figure 4.19 show the mean and root mean square values of the bubble length, lift and drag coefficients as a function of the cavitation number and compares these values with the reference values. Table 4.7 shows the error percentages of the bubble length, lift and drag coefficients for the simulated values of the cavitation number.

In figure 4.19a, it can be seen how the values of the bubble length for current CFD results are in agreement with the reference for the simulated cavitation numbers. The relative errors in l/c for a cavitation number of 1.29, 1.35 and 1.4 are 3.1%, 6.2% and 2.4% respectively (see table 4.7). The values for the lift coefficient are somewhat underestimated with respect to the reference values (see figure 4.19b).

The relative error percentages in C_L for the cavitation numbers 1.29, 1.35 and 1.4 are 6.4%, 6.9% and 6.4% respectively (see table 4.7), which are to be considered to be within acceptable margins. What stands out is the relatively large root mean square value of the simulation for $\sigma = 1.29$. This large root mean square value suggest that the end of the cavitation bubble shows some instabilities. This is not that surprising, since the the cavitation bubble becomes larger and more unstable as the bubble length approaches $l/c = 0.5$

The relative errors in C_D for the cavitation numbers 1.29, 1.35 and 1.4 are 28.3%, 31.8% and 32.1% respectively (see table 4.7). The values for the drag coefficient are not in agreement with the reference values. As it turns out, it is not trivial to get the drag coefficient withing reasonable margins, as can be seen by the results of Seo et. al. in figure 4.19b.

Table 4.7: Relative error percentages for l/c, C_L and C_L for the NACA-66(mod) at $\alpha = 6.5°$, $Re = 8 \times 10^5$ and turbulent viscosity exponent $n = 2.3$ for $\sigma = [1.29, 1.35 \, 1.4]$ with respect to reported values from Leroux.

σ	1.29	1.35	1.4
l/c	-3.11	-6.22	2.41
C_L	-6.39	-6.94	-6.44
C_D	-28.29	-31.78	-32.12

Table 4.8 shows the average relative error percentages of the cavity length l/c, the lift coefficient C_L and drag coefficient C_D averaged over all measured values for σ for each value of exponent n. The average relative error of the cavity length is 3.91% for the turbulent viscosity exponent $n = 2.3$ which is within acceptable accuracy margins whereas for $n = 2$ and $n = 3$ the relative error does not provide acceptable accuracy exceeding the 10%. The average relative error of the lift coefficient for $n = 3$ is lower than for $n = 2.3$, however, note that fluctuations in l/c and C_L where observed for $n = 3$ making the exponent $n = 3$ a unsuitable value for the model. This also holds for the drag coefficient.

Table 4.8: Average relative error percentages of l/c, C_L and C_D for the NACA-66(mod) at $\alpha = 6.5°$, $Re = 8 \times 10^5$ with respect to reported values from Leroux averaged over errors from $\sigma = [1.29, 1.35, 1.4]$.

n	l/c	C_L	C_D
3	12.60	4.30	24.33
2.3	3.91	6.59	30.73
2	13.33	9.17	33.96
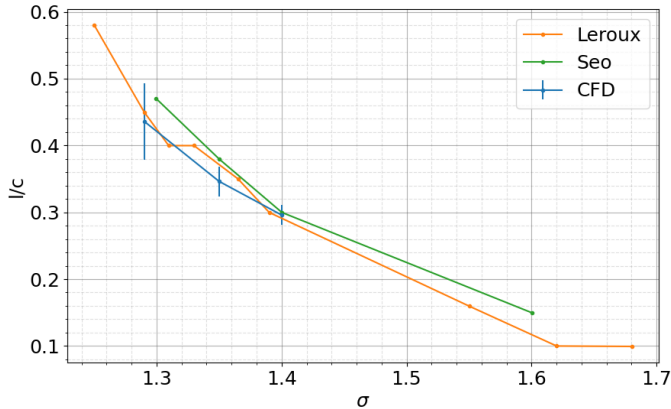
(a) Maximum cavity length as a function of the cavitation number σ.
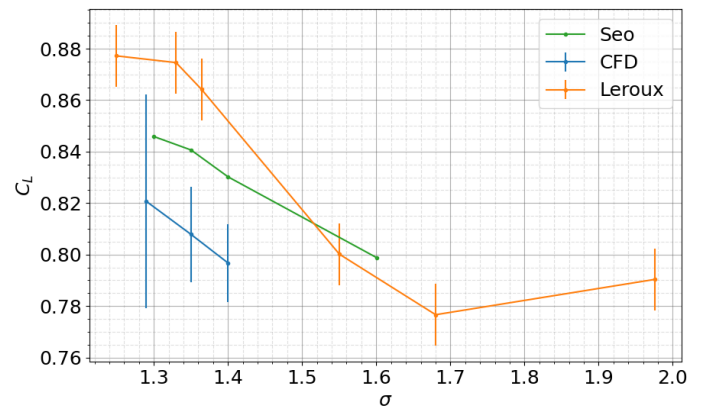
(b) Lift coefficient as a function of the cavitation number σ.
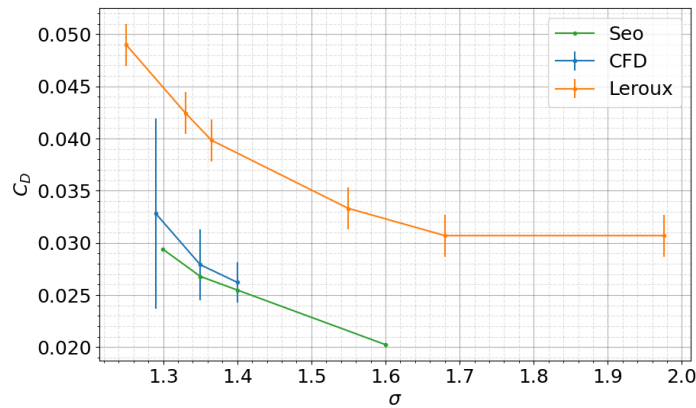
(c) Drag coefficient as a function of the cavitation number σ.

Figure 4.19: Maximum cavity length, lift and drag coefficients as a function of σ for the NACA-66(mod) at $\alpha = 6.5°$, $Re = 8 \times 10^5$ and $\sigma = 1.4$ with turbulent viscosity exponent $n = 2.3$ compared with reference values from Leroux [21] and Seo [32]. The mean and root mean square values are calculated from the time step samples from 0.5 to 0.7 seconds.

With the value of the turbulent viscosity exponent at $n = 2.3$, the current CFD setup with implemented Schnerr-Sauer cavitation model is considered to make sufficiently satisfactory predictions for the purpose of this project. The simulations for current study are conducted with this setting.

4.3. Cloud Cavitation

As documented by Leroux et. al. [20], two types of unsteady cavitation dynamics oscillations have been observed to occur, which are referred to in the paper as *dynamics 1* and *dynamics 2*. At $\alpha = 6.5°$ the frequency of the oscillation has been observed to be more or less constant with a frequency of about $\sim 3.5\,Hz$ for a range of cavitation numbers in the unstable cavitation regime, i.e. *dynamics 1*. The second type of oscillation behaviour, *dynamics 2*, has been observed as the angle of attack increases at about $\alpha = 7.5°$ with a frequency of about $40\,Hz$.

In section 4.3.1, the flow conditions for the reference case for 'dynamics 1' by Leroux is replicated with the current CFD setup. The results are presented and discussed. In section 4.3.2, the flow conditions for the the reference case for 'dynamics 2' by Leroux is replicated with the current CFD model. Again, the results are presented and discussed. For both cases, the same NACA-66(mod) geometry is used as for the steady sheet cavitation cases.

4.3.1. Dynamics 1

The flow conditions for the dynamics 1 reference case by Leroux are a free-stream velocity of $u_\infty = 5.33\,m/s$, an angle of attack of $\alpha = 6.5°$ and a cavitation number of $\sigma = 1.05$. The frequency of the bubble shedding can be determined by looking at the (quasi) periodic signal in the cavity length and the lift coefficient (figure 4.20). To do this, we look at the up crossings of the signal where the signal is more of less clean. For the cavity length, we look at the up-crossings at $l/c = 0.6$ and for the lift coefficient, we look at the up-crossings at $C_L = 0.8$. The time between two up-crossings gives an estimation for one period. Next, the mean of the four estimations is taken to get the final estimation. For the cavity length signal this gives a mean period of $0.339\,s$ and a frequency of $2.950\,Hz$. The estimation from the lift coefficient signal obtains a period of $0.342\,s$ and a frequency of $2.924\,Hz$. Averaging these two values gives a frequency of $2.935\,Hz$ and a Strouhal number of

$$St = fc/U = 0.083 .$$

The frequancy reported by Leroux et al. [20] for cavitation bubble shedding at the same conditions is about $3.625\,Hz$ corresponding to a Strouhal number of about $St = 0.102$. Compared with the reference value, the current cavitation set up results in an error of about 19%.

(a) Maximum cavity length l/c as a function of physical time (s).

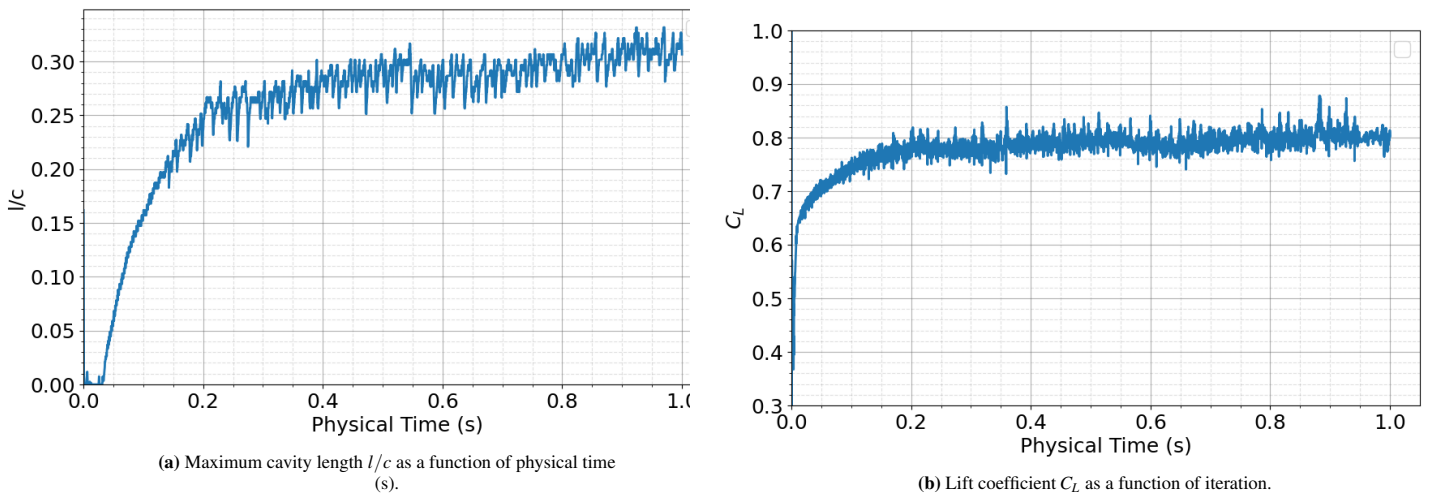**(b)** Lift coefficient C_L as a function of iteration.
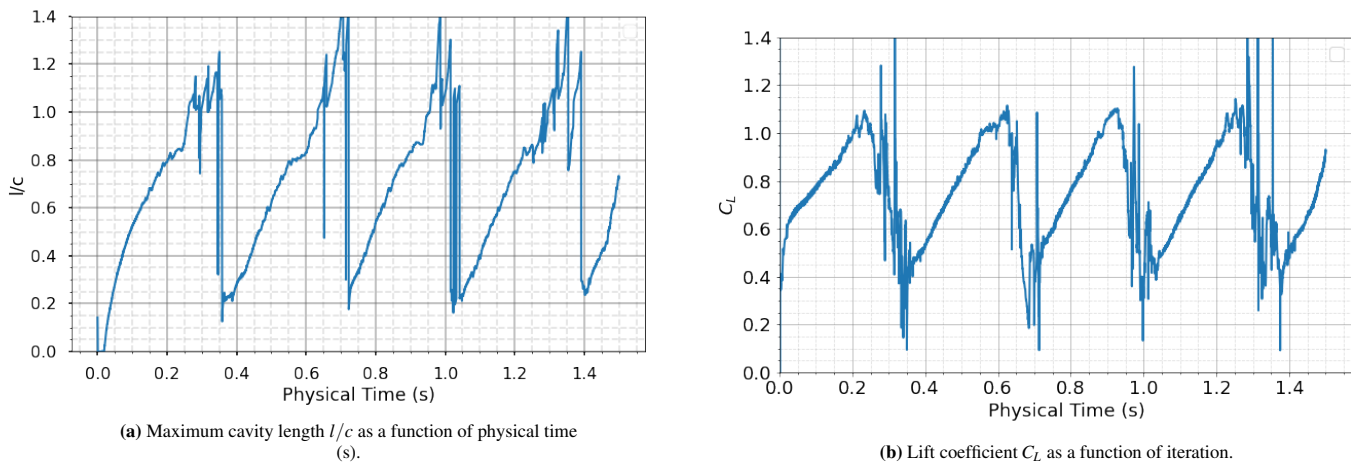
Figure 4.20: Time series of the maximum cavity length and lift coefficient during the course of the simulation for the NACA-66(mod) at $\alpha = 6.5°$, $u_\infty = 5.33\,m/s$ and $\sigma = 1.05$.

As the bubble length l/c is defined as the maximum value along the x-axis (in the hydrofoil reference frame) of the vapor volume fraction field with a cell value above 0.5, the peaks in the signal of the bubble length l/c can indicate a detached bubble convecting with the fluid instead of one continuously attached cavity. Hence, this value does not indicate the maximum attached cavity length per se. This is namely true for the strong peaks where $l/c > 0.8$, as the cavitation bubble often detaches around this point.

(a) $t \approx 0.37\,s$ **(b)** $t \approx 0.44\,s$

(c) $t \approx 0.51\,s$ **(d)** $t \approx 0.58\,s$

(e) $t \approx 0.65\,s$ **(f)** $t \approx 0.72\,s$
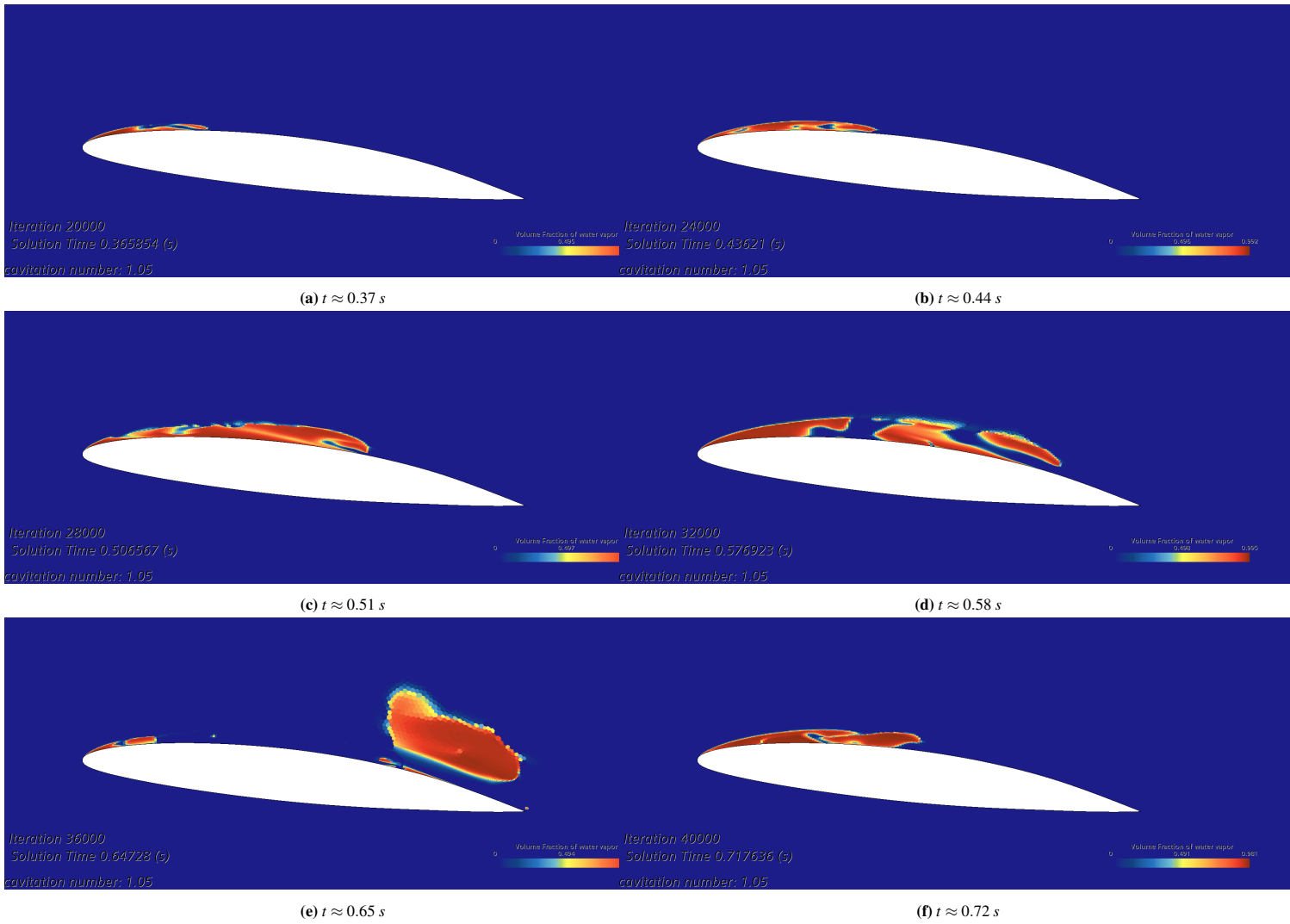
Figure 4.21: Images of the vapor volume fraction for the NACA-66(mod) at $\alpha = 6.5°$, $u_\infty = 5.33\,m/s$ and $\sigma = 1.05$ at times $t \approx [0.37, 0.44, 0.51, 0.58, 0.65, 0.72]$ showing the bubble instability.

In figure 4.21, images of the vapor volume fraction field are shown at times $t \approx [0.37, 0.44, 0.51, 0.58, 0.65, 0.72]$ seconds. The bubble growth can be distinguished in the first three images, corresponding to the bubble growth in figure 4.20a up to about, $t \approx 0.55\,s$. In figure 4.21d, the start of the bubble separation can already be seen and in figure 4.21e the cavitation bubble is fully separated and starts to convect with the fluid until it disappears at around 0.7 seconds. In the meantime, the growth of a new cavitation bubble can already be seen in 4.21e and in 4.21f the new cavitation bubble is grown up to about $l/c \approx 0.5$, having completed a cycle.

4.3.2. Dynamics 2 (case 1)

The flow conditions for the dynamics 2 reference case by Leroux are a free stream velocity of $u_\infty = 5.33\,m/s$, an angle of attack of $\alpha = 8°$ and a cavitation number of $\sigma = 1.27$.

Again, the frequency of the (quasi) periodic bubble shedding is determined by looking at the bubble length and lift coefficient, see figures 4.22a and 4.22b. In both figures, two clear periods can be determined with a frequency of about $\sim 2.5\,Hz$. However, after $0.8\,s$, the periodicity in the signal changes and becomes more noisy.

According to Leroux [20], the frequency of the dynamics 2 behaviour at these operating conditions is about $\sim 18\,Hz$. This does not correspond to the frequency of the first few periods. After 0.8 seconds, the oscillations in the bubble length signal are too small to represent the bubble shedding oscillations. Hence, for these operating conditions, the current simulation with cavitation model set up is not in agreement with the reference.

(a) Maximum cavity length l/c as a function of physical time (s).

(b) Lift coefficient C_L as a function of iteration.
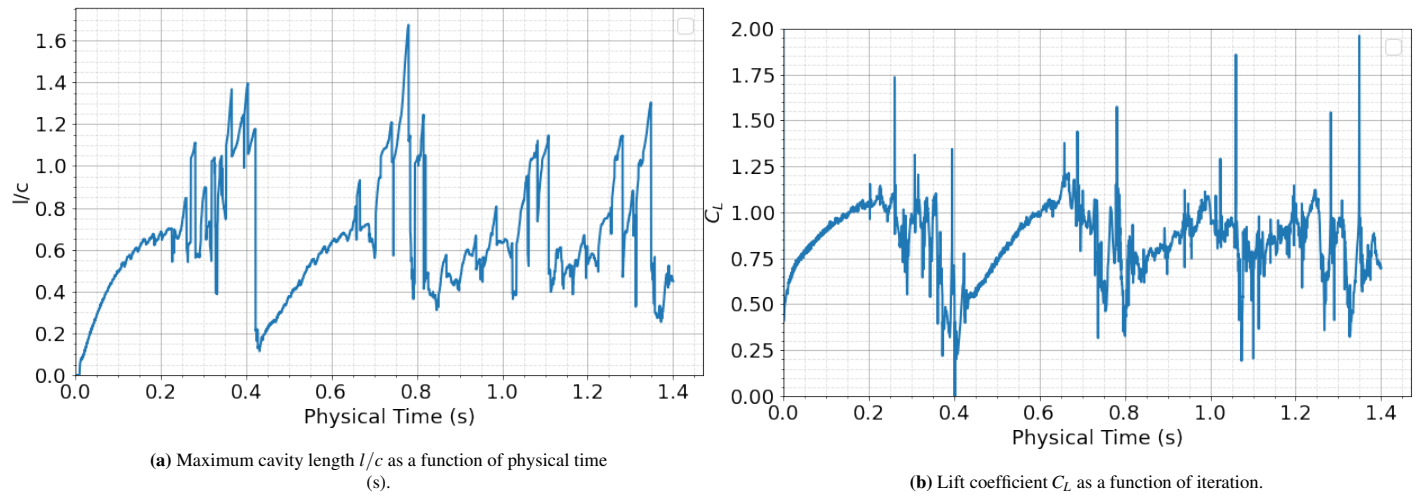
Figure 4.22: Time series of the maximum cavity length and lift coefficient during the course of the simulation for the NACA-66(mod) at $\alpha = 8°$, $u_\infty = 5.33\,m/s$ and $\sigma = 1.27$.

4.3.3. Dynamics 2 (case 2)

The dynamics 2 behaviour documented by Leroux is reported to have a more or less fixed frequency for a range of operating conditions. Here, the free stream velocity is increased to see whether the dynamics 2 behaviour can be captured.

For the operating conditions $\alpha = 8°$, $\sigma = 1.31$ and $u_\infty = 12.86\,m/s$ (or $25\,knts$), a clear bubble shedding oscillation signal can be seen in the cavitation bubble length signal (figure 4.23a) and the lift coefficient (figure 4.23b). Again, an estimate of the frequency of the quasi-periodic signal can be made by counting the up crossings, measuring the period of each oscillation and taking the average of the measured periods. This estimation yields a frequency of about $\sim 5.9\,Hz$, corresponding to a Strouhal number $St = 0.068$. This result does not correspond to the reported reference frequency for dynamics 2. Surprisingly however, the Strouhal number is not far off from the Strouhal number measured earlier for $\alpha = 6.5°$, $\sigma = 1.05$ and $u_\infty = 5.33\,m/s$, suggesting that the measured comes closer to the reported dynamics 1 behaviour.

(a) Maximum cavity length l/c as a function of physical time (s).

(b) Lift coefficient C_L as a function of iteration.
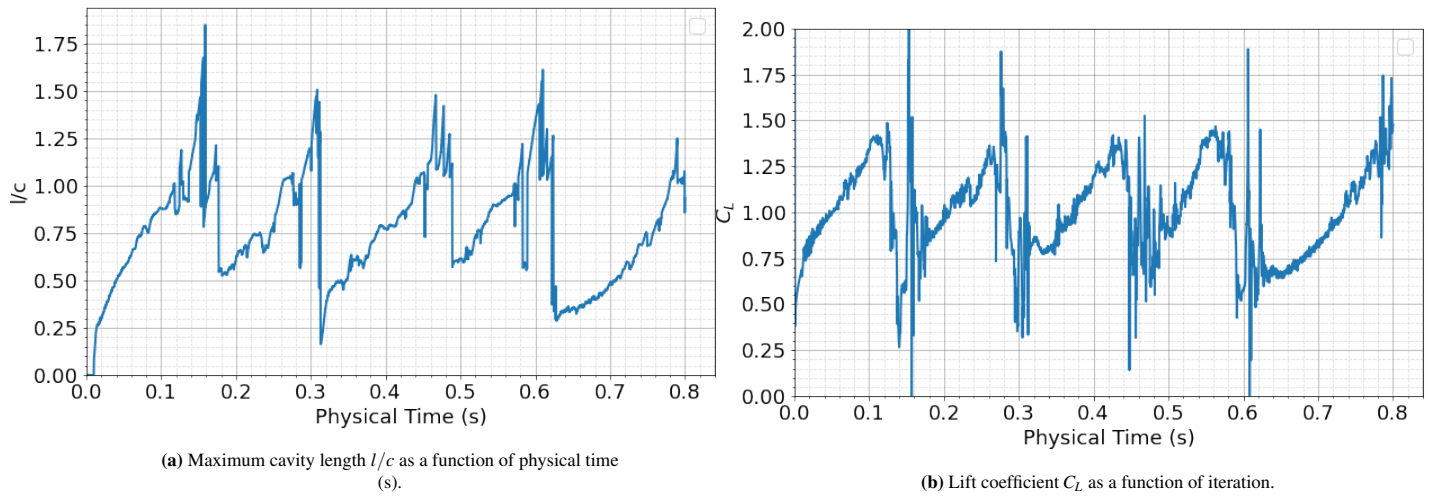
Figure 4.23: Time series of the maximum cavity length and lift coefficient during the course of the simulation for the NACA-66(mod) at $\alpha = 8°$, $u_\infty = 12.86\,m/s$ and $\sigma = 1.31$.

(a) $t \approx 0.32\ s$

(b) $t \approx 0.35\ s$

(c) $t \approx 0.38\ s$

(d) $t \approx 0.41\ s$

(e) $t \approx 0.44\ s$

(f) $t \approx 0.47\ s$
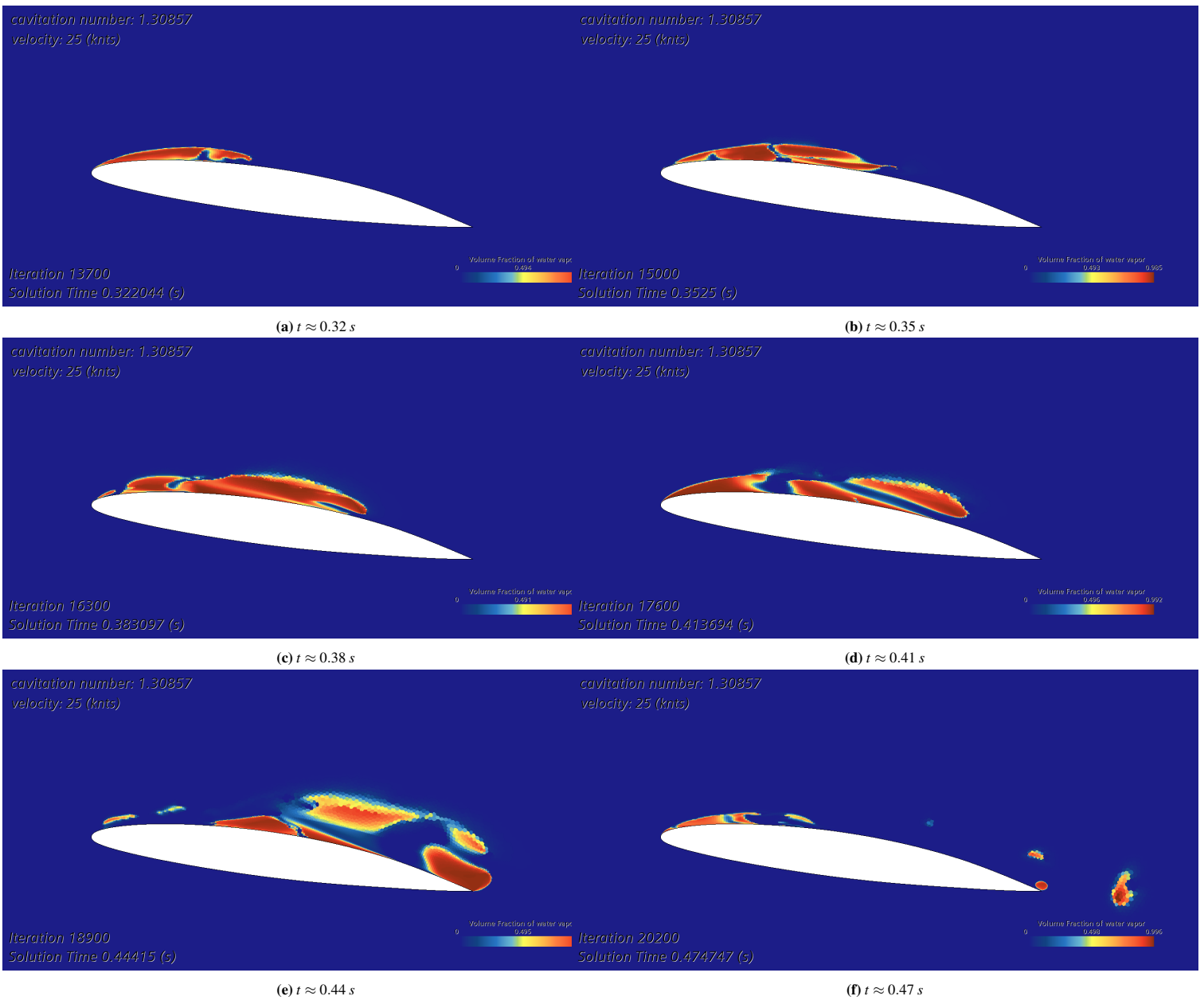
Figure 4.24: Images of the vapor volume fraction for the NACA-66(mod) at $\alpha = 8°$, $u_\infty = 12.86\,m/s$ and $\sigma = 1.31$ at times $t \approx [0.419, 0.426, 0.433, 0.44]$ showing the bubble instability.

4.3.4. Bubble Growth and Detachment

In figure 4.25, a series of images of the velocity field around the suction side of the foil during the cavitation bubble growth and detachment is shown at $\alpha = 8$, $\sigma = 1.27$ and $u_\infty = 12.86\,m/s$. The local flow velocity vectors are indicated with black arrows and the purple line indicates the contour of the cavitation bubble defined by a vapor volume fraction > 0.5. In figure 4.25a, the flow vectors clearly show flow reversal at the end of the cavitation bubble and reversed flow within the cavitation bubble can be identified. This behaviour is widely reported in the literature and is referred to as the re-entrant jet. As the bubble grows (see figure 4.25b), the flow velocity of the re-entrant jet increases up to about 70% of the free stream velocity, at this point the bubble starts to detach and convect with the fluid. This process can be seen in figures 4.25c and 4.25d. In the mean time, a new cavitation bubble is growing and starting a new shedding cycle.

It can be seen in the velocity field images (figure 4.25) that the cell size is quite large at locations where the cavitation bubble is shedded into the fluid. At these locations, very strong velocity gradients are also to be seen. Ideally, the mesh should be well refined at locations with strong gradients in order to accurately resolve the fluid. This is likely to play a significant role to the fact that the results for unstable cloud cavitation do not correspond well with the reference values.

(a) $t \approx 0.031 \, s$

(b) $t \approx 0.062 \, s$

(c) $t \approx 0.093 \, s$

(d) $t \approx 0.124 \, s$

(e) $t \approx 0.155 \, s$
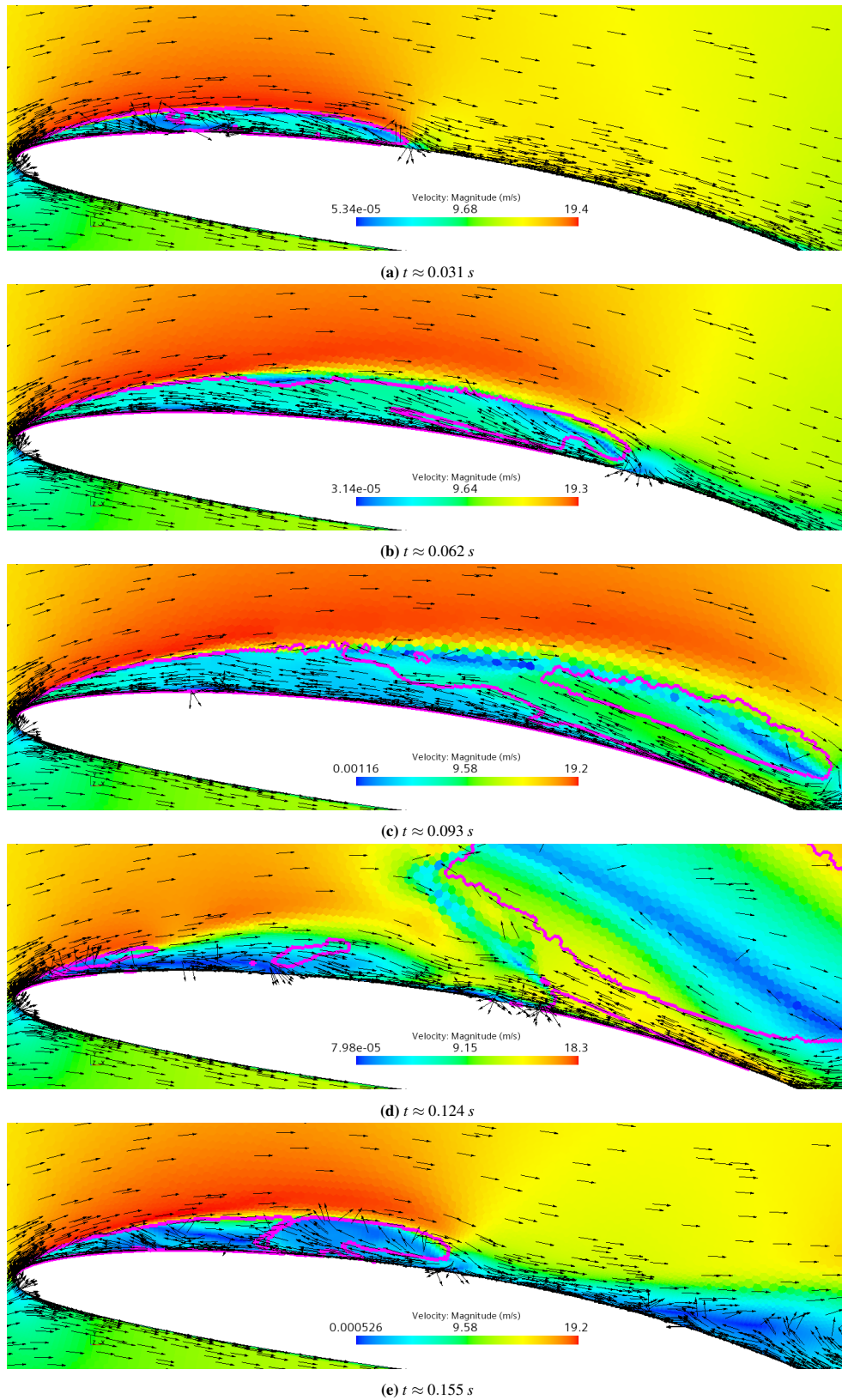
Figure 4.25: Images of the velocity field during the bubble growth and detachment for the NACA-66(mod) at $\alpha = 8°$, $u_\infty = 12.86 \, m/s$ and $\sigma = 1.27$. The local flow velocity vectors are indicated with the black arrows. The purple line defines the contour of the cavitation bubble defined by a vapor volume fraction > 0.5.

4.4. Cavitation Analysis With vs. Without Cavitation Model

Cavitation is an important phenomenon to consider in the design and development of hydrofoils. Without actually modelling the cavitation phenomenon in CFD, one can analyse the pressure field and look at where the pressure falls below the saturation vapor pressure to make an estimation where the flow will cavitate. In the design process, one can use this method to modify the design in order to eliminate or minimize the region on the foil surface which falls below the saturation vapor pressure. This is a common technique to account for cavitation in the design of hydrofoils. The drawback of this technique is that when the flow actually starts to cavitate, the cavitation bubble perturbs the flow around the hydrofoil and consequentially the performance of the hydrofoil modified. It is therefore useful to see how the cavitated region and the flow around the foil behaves using just this pressure analysis method compared to results using a cavitation model to simulate the actual phenomenon.

4.4.1. NACA-66(mod)

Here, the flow around the foil and performance of the NACA-66(mod) section is compared between the pressure field analysis and simulation results with cavitation model as developed and validated in earlier sections. The same operating conditions, i.e. $\alpha = 6.5°$, $\sigma = 1.4$ and $u_\infty = 5.33\,m/s$, and geometry is run with and without cavitation model activated.

In figure 4.31 the pressure coefficient distribution along the foil with and without cavitation model are shown. For the simulation without cavitation model, the leading edge suction side of the foil experiences a strong negative pressure peak. The simulation with cavitation model shows a constant pressure about equal to the (non-dimensional) saturation vapor pressure along the suction side up the end of the cavitation bubble at about $x/c \approx 0.3$. Although the pressure just downstream for the end of the cavitation bubble shows a positive peak, the lift coefficient is slightly higher for the simulation with cavitation model, as shown in table 4.9. In this table, an overview of the the cavitation region length (indicated with l/c), lift and drag coefficient and lift over drag results is shown. The length of the cavitation region in the simulation with the cavitation model is about $l/c = 0.31$ whereas the without cavitation model the length of the region is measured to be $l/c = 0.054$. Due to this stretched low pressure cavitation region, the lift in the simulation with cavitation model is slightly higher with $C_L = 0.813$ versus $C_L = 0.804$ without cavitation model. The drag coefficient has also increased in the simulation with cavitation model with $C_L = 0.0264$ and $C_L = 0.0149$ without cavitation model resulting in a significant drop in lift over drag, i.e. efficiency with $L/D = 30.8$ in the simulation with cavitation model and 54 in the simulation without.
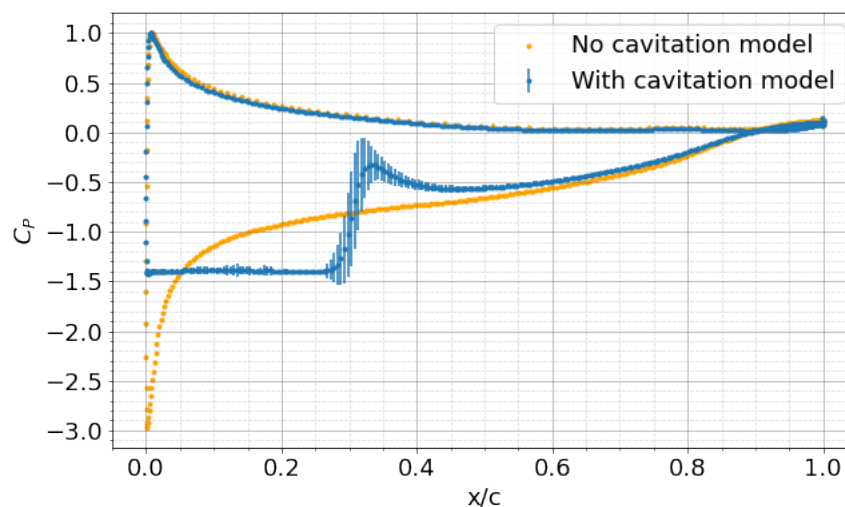
Figure 4.26: Comparison of the pressure distributions of the simulation results with and without cavitation for the NACA-66(mod) at $\alpha = 6.5°$, $u_\infty = 5.33\,m/s$ and $\sigma = 1.4$.

Table 4.9: Cavitation region length, lift and drag coefficient results for simulations of the NACA-66(mod) at $\alpha = 6.5°$, $u_\infty = 5.33\,m/s$ and $\sigma = 1.4$ with and without cavitation model.

	With Cavitation	Without Cavitation
l/c	0.31	0.054
C_L	0.813	0.804
C_D	0.0264	0.0149
L/D	30.8	54.0

In figure 4.31, the pressure fields for both the simulation with and without cavitation model are shown. The minimum value of the color map is set to the saturation vapor pressure and the region for which $p < p_{sat}$ is marked in purple. It can be seen how the length of the cavitated region at the leading edge for the results without simulation model is much smaller than the cavitated region in the simulation with cavitation model. It looks as if the low pressure cavitation bubble has been spread out along the suction side of the foil, resulting in a large low pressure region above the cavitation bubble covering a large part of the suction side.

cavitation number: 1.4

(a) Without cavitation model.

cavitation number: 1.4

(b) With cavitation model.
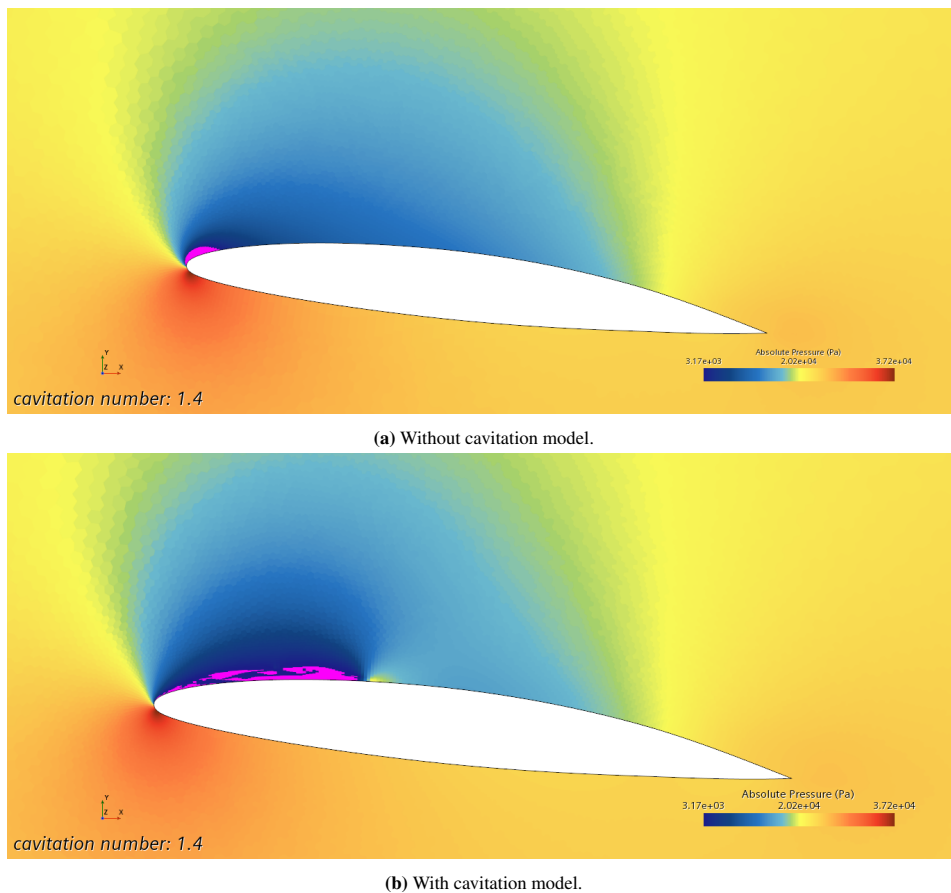
Figure 4.27: Images of the pressure field of the converged simulations with and without cavitation model of the NACA-66(mod) at $\alpha = 6.5°$, $u = 5.33\,m/s$ and $\sigma = 1.4$. The cavitated region is indicated in pink.

Analysing these results, it can be stated that when using the simple method of pressure analysis the length of the cavitation region is significantly underestimated compared to the simulation resolving the cavitation phenomenon. As a result the lift coefficient is slightly underestimated (about 1%), as well as the drag coefficient (about 43%) and thus is the efficiency overestimated by about 43% if the analysis is done using only the pressure field analysis.

4.4.2. BPXI

The same analysis is performed for a hydrofoil section section we will refer to as *BPXI*, in the following operating conditions; $\alpha = 4°$, $\sigma = 0.63$ and $u_\infty = 18.52\,m/s$ (or 36 *knts*). For these conditions, cloud cavitation has been observed in data that cannot be reported here for reasons of confidentiality.

In figure 4.28 the pressure coefficient distributions along the foil with and without cavitation model are shown for the simulations with and without cavitation model. For the simulation without cavitation model, the leading edge suction side of the foil experiences a strong negative pressure peak. The pressure distribution for the simulation without cavitation model gives large root mean square values, suggesting unsteady behaviour in the cavitation bubble causing large pressure fluctuations.

Looking at the time series of the bubble length and lift coefficient during the course of the simulation in figure 4.29, the unstable behaviour of the cavitation bubble is clearly to be seen as from about 0.08 seconds.

Figure 4.30 shows the frequency spectrum of the C_L time series from the simulation for the *BPXI* hydrofoil section at $\alpha = 4°$, $u_\infty = 18\,m/s$ and $\sigma = 1.4$. It can be seen that there is no clear dominant frequency is present in the spectrum.
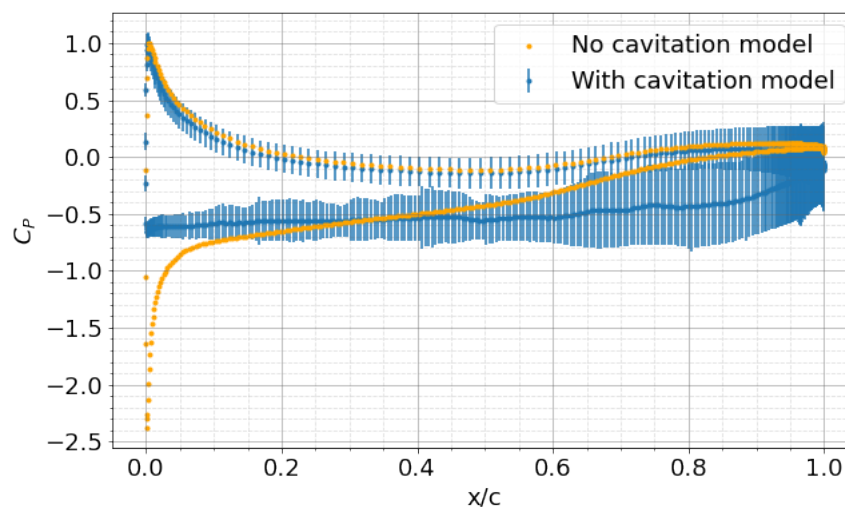
Figure 4.28: Comparison of the pressure distributions of the simulation results with and without cavitation for the *BPXI* hydrofoil section at $\alpha = 4°$, $u_\infty = 18\,m/s$ and $\sigma = 1.4$.

(a) Maximum cavity length l/c as a function of physical time (s).

(b) Lift coefficient C_L as a function of physical time.

Figure 4.29: Time series of the maximum cavity length and lift coefficient during the course of the simulation for the *BPXI* hydrofoil section at $\alpha = 4°$, $u_\infty = 18\,m/s$ and $\sigma = 1.4$.
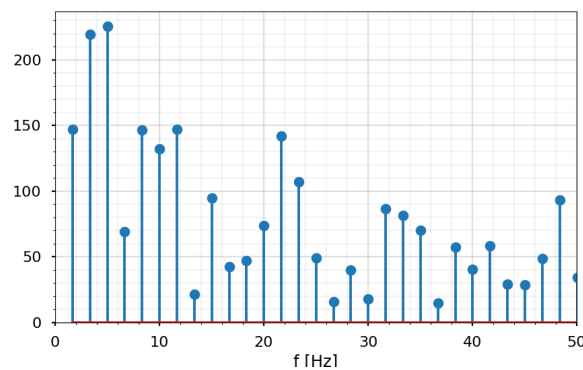
Figure 4.30: Frequency spectrum of the first 50 lowest frequencies for the C_L time series from the simulation of the *BPXI* hydrofoil section at $\alpha = 4°$, $u_\infty = 18\,m/s$ and $\sigma = 1.4$.

Figure 4.31 shows images of the pressure fields of the simulation with and without cavitation model. For confidentiality reasons, the section geometry is covered up by a black ellipse. The pressure field without cavitation model shows a cavitation region at the leading edge on the suction side with a length of about $l/c = 0.23$. On the other hand, the pressure field for the simulation with cavitation model shows the detachment of a cavitation bubble near the trailing edge. The cavitation behaviour shows to be strongly unsteady, however no clear periodicity of a cavitation growth and detachment is seen in the bubble length and lift coefficient signal. The behaviour is similar as seen in section 4.3.2, where a quasi period bubble shedding was expected but not found with the current simulation set up. Therefore, it is probable that the current simulation set up does not resolve the unsteady flow state sufficiently well in order to capture any possible periodic bubble shedding.

(a) Without cavitation model.

(b) With cavitation model.
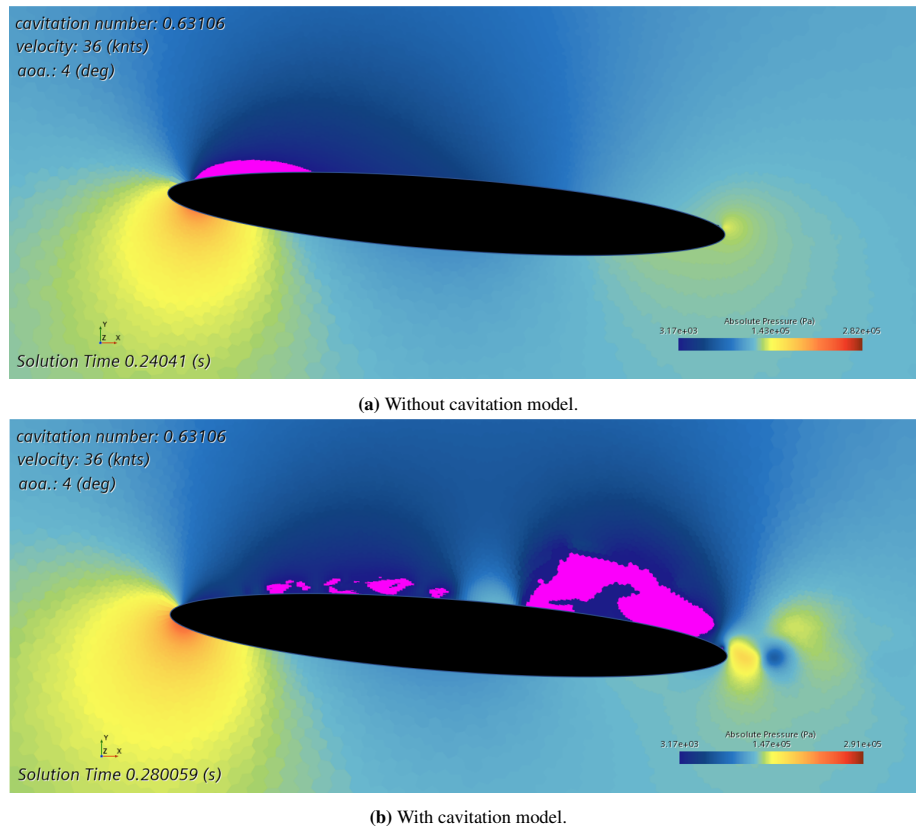
Figure 4.31: Images of the pressure field of the converged simulations with and without cavitation model for the *BPXI* hydrofoil section at $\alpha = 4°$, $u = 18.52 \, m/s$ and $\sigma = 0.63$. The region indicated in magenta is where $p < p_{sat}$, which represents the cavitated region. The section geometry is sensored by a black ellipse for confidentiality reasons.
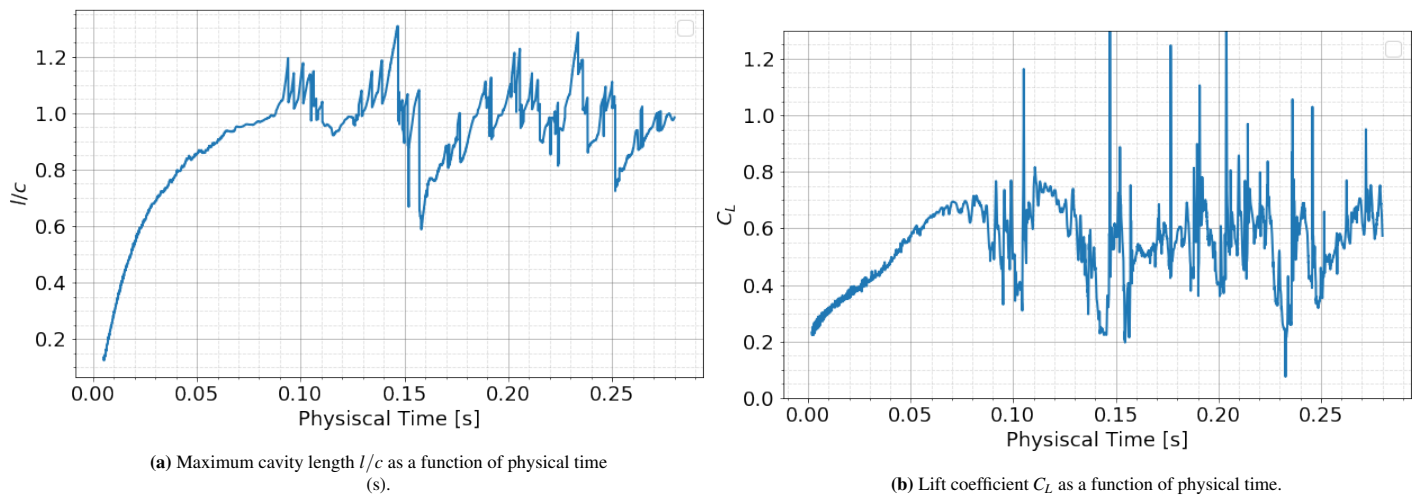
4.5. Stability Analysis

In figure 4.32, the results for the cavity length l/c is plotted as a function of the stability parameter $p_s = \frac{\sigma}{2(\alpha - \alpha_0)}$ for the simulation runs with fixed free stream velocity and for fixed absolute pressure. The analytical approximation from linear theory is indicated with the black dotted lines. The mean cavity length l/c and the root mean square (RMS) fluctuation are derived from the time series of the cavity length with a sample size of 3904. The mean values are indicated with the blue dots and the fluctuations are denoted with the orange stars.
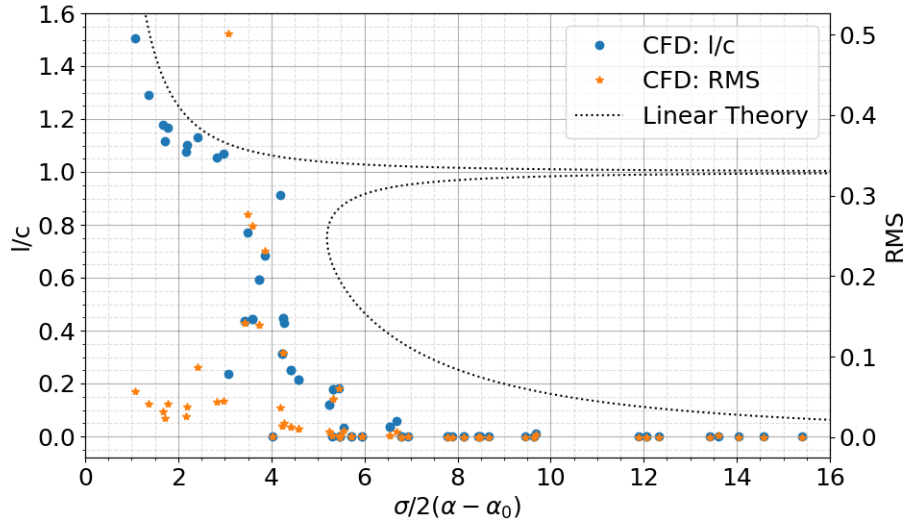
Figure 4.32: Cavitation length l/c and RMS fluctuation as a function of $\sigma/2(\alpha - \alpha_0)$ with analytical approximation from linear theory.

It can be seen in figure 4.32 that (virtually) no cavitation occurs for values of p_s higher than about 7. From about 7 to 5, the first early cavitation cases seem to start forming small sheet cavitation bubbles up to a length of about $l/c \approx 0.2$. These cases show little variation in the cavitation bubble length ($RMS < 0.05$). This is as expected since steady sheet cavitation occurs first at high values of σ and low α. From about $p_s \approx 5$ to about 4, the cavitation bubble grows up to about $l/c \approx 0.45$. The cavitation bubbles are still stable for these cases, this is consistent with observations from Leroux et. al. reporting cavitation bubbles to be stable up to $l/c \approx 0.5$. The RMS fluctuation in this range is globally still small ($RMS < 0.1$) indicating stable cavitation bubbles.

It can be seen that the data points with the largest RMS fall between values of the stability parameter $p_s = 3$ and 4 with a $RMS = 0.4$ and higher. A few data points have a RMS between 0.2 and 0.3 and one data point has $RMS = 0.5$. These higher values in the RMS indicate large variance in the cavity length, hence showing strong cavitation instability. It can be verified what cavitation regime the data points represent by looking at the simulation images. Looking at these images, it can be seen that the data points with the stability parameter in the range $3 < p_s < 4$ undergo cloud cavitation. Some data points near $p_s = 4$ can have slightly elevated RMS values. However, looking at the images these simulations do not show the distinct bubble growth and shedding cycle associated with cloud cavitation, although the observed variation in bubble length seems to indicate being near the transition to cloud cavitation. It is shown that the transition from stable to unstable cavitation is roughly found at $p_s \approx 4$. This result is coherent with results from Leroux et. al. [21] and Arndt et. al. [4].

It should be mentioned that the measurements of the mean cavity length for the unsteady cases can be marginally inaccurate due to the definition of the cavitation length. As mentioned in section 3.2.6, the maximum x-position of the vapor volume fraction used in the definition of the cavity length is shedding with the bubble into the flow for unstable cloud cavitation cases. This may cause the measurement to be a little higher than the actual length of the "main" continuous cavitation bubble. Furthermore, for some of the unstable cloud cavitation cases, the time series only captures a few periods. This might be on the lower end in order to get a very accurate estimate of the mean bubble length. It should therefore be taken into consideration that the estimates of the mean bubble lengths may be slightly inaccurate for the measurements with a high RMS.

Bubbles with $l/c > 1$ enter the super cavitation regime which forms a stable bubble encapsulating the suction side of the section. The super cavitation cases fall within the range of transition parameter $p_s < 3$, except one case with a bubble length of about $l/c = 0.91$ for $p_s = 4.2$. The operating conditions for this case are $\alpha = 0$ and

$U_\infty = 45\,knts$. Looking at the simulation images, it can be seen that a stable cavitation bubble has formed around the suction side of the section. However, since the angle of attack is 0, the cavitation bubble does not start at the leading edge of the section but at about $c/4$. Hence, the measurement of the stable super cavitating bubble results in a value smaller than 1. In the super cavitation regime, the bubble lengths can still vary a bit due to unsteadiness in the flow, hence the *RMS* values go up to about 0.1 in this range.

In figure 4.33 a snapshot from the converged simulation for an angle of attack $\alpha = 6°$, cavitation number $\sigma = 2.04$ and freestream velocity $u_\infty = 10.29\,m/s$ or ($20\,knts$) is shown for which the stability parameter results in $p_s = 6.7$. For these conditions, a small stable sheet cavitation bubble at the leading edge of the foil of about $l/c \approx 0.1$ has formed as can be seen in the image.
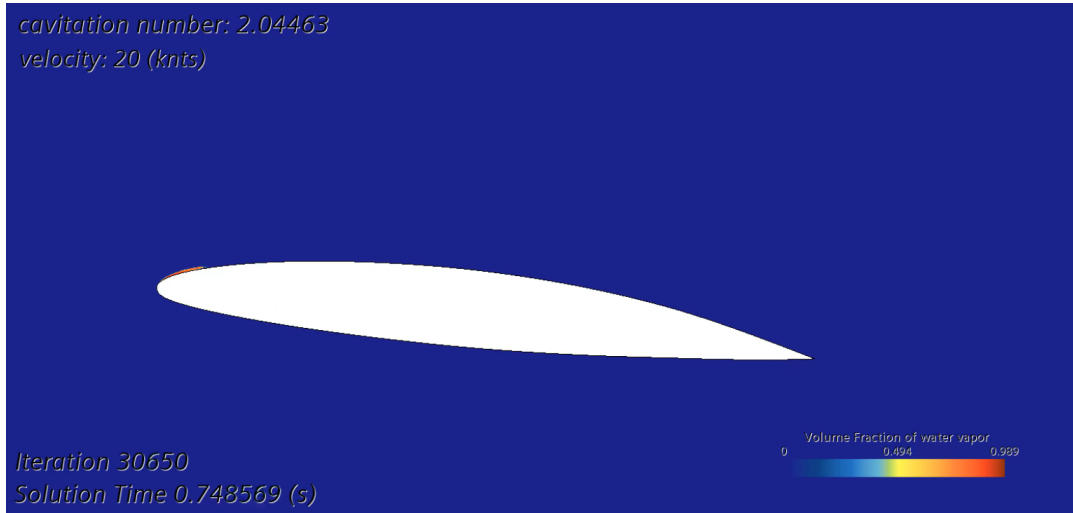
Figure 4.33: Simulation snapshot of the vapor volume fraction around the NACA-66(mod) at $\alpha = 6°$, $\sigma = 2.04$.

In figure 4.34 a snapshot of the converged simulation is shown for an angle of attack of $\alpha = 6°$, in a freestream velocity of $U_\infty = 5.33\,m/s$ with a cavitation number of $\sigma = 1.29$. The stability parameter results in $p_s = 4.33$ and the relative bubble length is about $l/c \approx 0.3$. For these conditions, the sheet cavitation bubble is quasi-stable, showing variations in the bubble length with $0.01 < RMS < 0.1$.
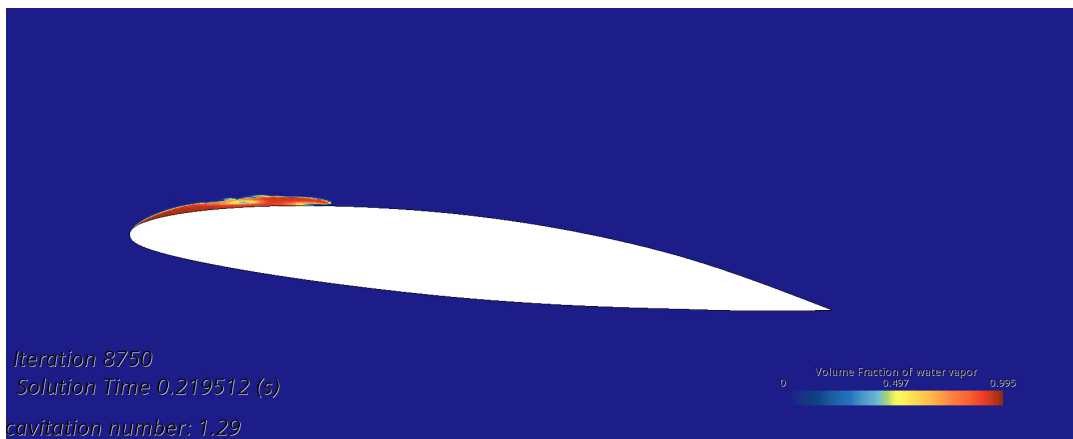
Figure 4.34: Simulation snapshot of the vapor volume fraction around the NACA-66(mod) at $\alpha = 6°$ and $\sigma = 1.29$.

In figure 4.35, a simulation snapshot of a run with unsteady cloud cavitation conditions is shown. The section is at an angle of attack of $\alpha = 4°$, in a freestream velocity of $15.4\,m/s$ (or $30\,knts$) with a cavitation number of about $\sigma = 0.9$. This results in a stability parameter of $p_s = 3.94$ and cavitation bubble shows a growing and shedding cycle. In figure 4.35, the shedding of a cavitation bubble is captured while the attached part of the cavitation bubble is shrinking towards the leading edge to begin a new cycle.

cavitation number: 0.908727

velocity: 30 (knts)

Volume Fraction of water vapor
0   0.496   0.991

Iteration 15050

Solution Time 0.364203 (s)
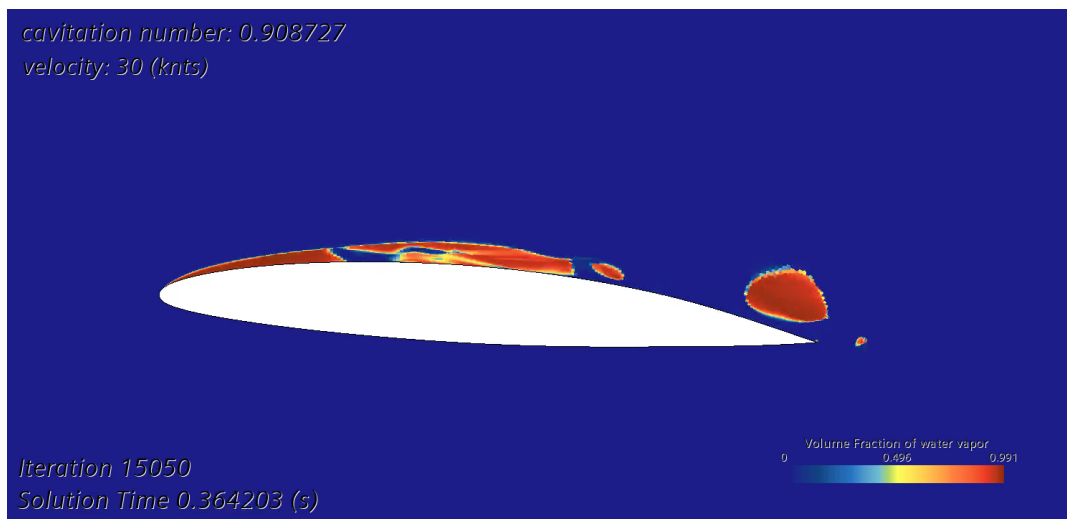
Figure 4.35: Simulation snapshot of the vapor volume fraction around the NACA-66(mod) at $\alpha = 4°$ and $\sigma = 0.9$.

In figure 4.36, a simulation snapshot of a run with supercavitation conditions is shown. The section is at an angle of attack of $\alpha = 8°$, in a freestream velocity of $U_\infty = 23.15\ m/s$ (or 45 $knts$) with a cavitation number of about $\sigma = 0.4$. The stability parameter results in a value of about $p_s = 1.09$ and the relative cavitation bubble length becomes stable at about $l/c = 1.56$.

Iteration 34044

Solution Time 0.800034 (s)

Volume Fraction of water vapor
0   0.499   0.998

cavitation number: 0.403878
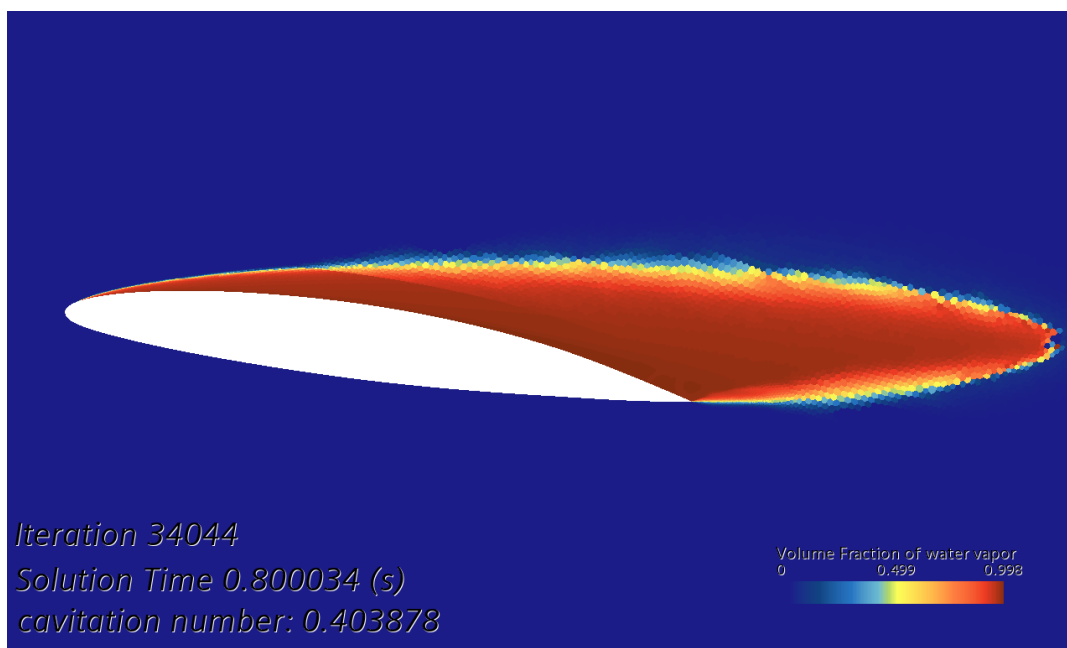
Figure 4.36: Simulation snapshot of the vapor volume fraction around the NACA-66(mod) at $\alpha = 8°$ and $\sigma = 0.4$

In figure 4.37, the bubble length l/c versus the stability parameter p_s is plotted again for the non-zero values of current CFD study using a NACA-66(mod) as well as experimental results from Arndt et. al. [4] using a NACA-0015. Assuming a proportional trend, a linear fit is plotted though the respective data points in order to make a rough estimate of the relation between the stability parameter and the cavitation bubble length. In the study from Arndt, the inception of sheet cavitation is stated to be at about $\frac{\sigma}{2\alpha} = 8.5$ ($a_0 = 0$ for symmetric section). These observation are also coherent with observations from Kjeldsen et. al. [18]. It can be seen that this observation is fairly coherent with the rough linear estimate in figure 4.37 with the inception of sheet cavitation at about $\frac{\sigma}{2\alpha} = 8$. In the current CFD study of the NACA-66(mod), following the linear estimate finds that sheet cavitation starts at about $p_s = 5.75$, suggesting that cavitation starts to form at higher values of sigma

(lower pressures and freestream velocities) and lower angles of attack. This would mean that the NACA-66(mod) section is more optimized to delay the formation of stable sheet cavitation compared to the NACA-0015 section.

Furthermore, Arndt observed a transition in the bubble length oscillation from high frequency with low spectral peaks to low frequency with high spectral peaks at about $\frac{\sigma}{2\alpha} = 4$. The transition towards the high spectral peaks with low frequency indicate the transition to cloud cavitation which is coherent with observations from Leroux [20] which also finds transition to cloud cavitation at about $p_s = 4$.
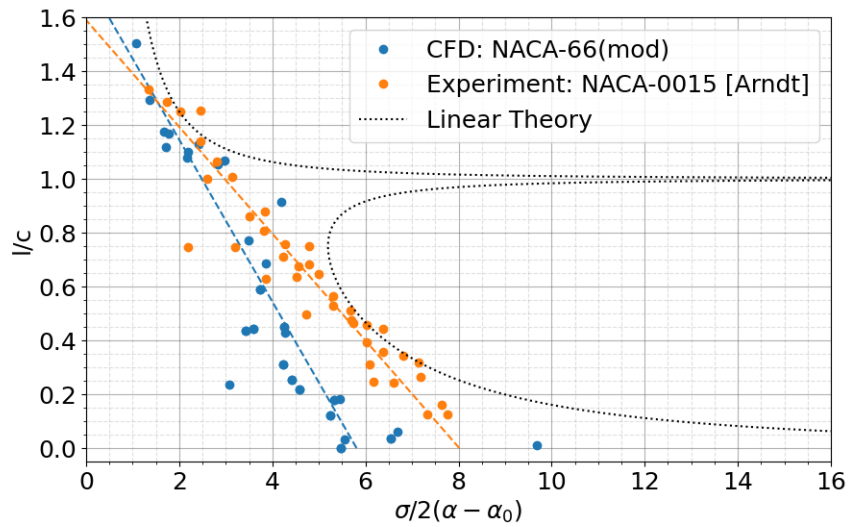
Figure 4.37: Cavitation length l/c as a function of $\sigma/2(\alpha - \alpha_0)$ from current CFD study with a NACA-66(mod) section compared to experimental results from Arndt et. al. [4] using a NACA-0015 section.

4.6. Polars

In this section, the lift coefficient C_L, drag coefficient C_D and Lift over Drag L/D (or performance) are studied as a function of the angle of attack. A series of simulations is run for the angles of attack $\alpha = [0, 2, 4, 6, 8]$ and for the cavitation numbers $\sigma = [1.6, 1.4, 1.35, 1.2, 1]$. First the results for the lift coefficient are presented and discussed, then the results for the drag coefficient, next the results for the performance and finally a literature comparison is made with experimental results from Leroux et. al. [20] and with potential flow results from *xFoil*.

Lift Coefficient C_L

In figure 4.38, the CFD results for the lift coefficient polars are shown. The CFD results are plotted for the chosen angles of attack and for the cavitation numbers. The error bars indicate the *RMS* of the lift coefficient over time for. The lines are connected while the data points, indicated with a dot, represent non cavitating or stable cavitation cases. When the data point represent unstable cavitation cases, the points are not connected to the rest of the graph and are indicated with an *x* symbol. Table 4.10 show an overview of the results of the average lift coefficient values and *RMS*. Table 4.11 shows the average bubble length and root mean square values.

Table 4.10: CFD results for lift coefficient polars of the NACA-66(mod) for $\sigma = [1, 1.2, 1.35, 1.4, 1.6]$: time average (left) and *RMS* fluctuation(right).

α	σ					α	σ				
	1	1.2	1.35	1.4	1.6		1	1.2	1.35	1.4	1.6
0°	0.203	0.203	0.203	0.203	0.203	0°	0.0012	0.0012	0.0012	0.0012	0.0012
2°	0.399	0.399	0.399	0.399	0.399	2°	0.0029	0.0029	0.0029	0.0029	0.0029
4°	0.639	0.603	0.591	0.591	0.591	4°	0.0179	0.0138	0.0040	0.0040	0.0040
6°	0.736	0.877	0.813	0.801	0.782	6°	0.1971	0.0196	0.0145	0.0142	0.0145
8°	0.869	0.982	1.192	0.916	1.088	8°	0.2469	0.2245	0.2231	0.2827	0.0985
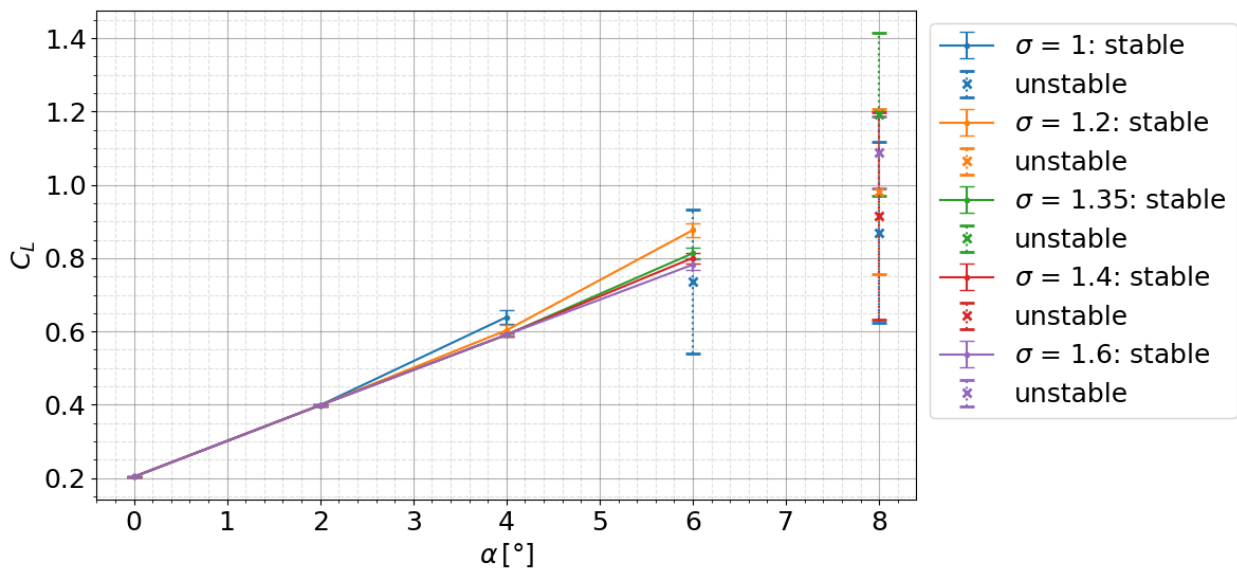
Figure 4.38: Lift coefficient polars from CFD results of the NACA-66(mod) for $\sigma = [1, 1.2, 1.35, 1.4, 1.6]$ with stable and unstable cavitation cases.

Table 4.11: CFD results for dimensionless Cavity Length l/c of the NACA-66(mod) for $\sigma = [1, 1.2, 1.35, 1.4, 1.6]$: time average (left) and *RMS* fluctuation(right).

α	σ 1.0	1.2	1.35	1.4	1.6	α	σ 1.0	1.2	1.35	1.4	1.6
0°	0	0	0	0	0	0°	0	0	0	0	0
2°	0	0	0	0	0	2°	0	0	0	0	0
4°	0.27	0.06	0	0	0	4°	0.036	0.015	0	0	0
6°	0.70	0.56	0.33	0.28	0.16	6°	0.280	0.028	0.016	0.014	0.010
8°	1.09	0.92	0.90	0.62	0.56	8°	0.127	0.252	0.181	0.344	0.132

At low angles of attack, i.e 0° and 2°, the CFD results give the same value for each cavitation number. At $\alpha = 0°$, a lift coefficient of $C_L = 0.203$ is found with a root mean square of $RMS = 0.001$. At $\alpha = 2°$, a lift coefficient of $C_L = 0.399$ is found with a root mean square of $RMS = 0.003$. For these operating conditions at low angles of attack, no cavitation has been formed yet and thus the lift coefficient has not been altered. A suggestion for a follow up study would be to chose the operating conditions such that at least one value for sigma is found for which cavitation occurs.

The results start diverging for $\alpha = 4$ and higher. For $\alpha = 4°$, stable sheet cavitation occurs for the CFD results for $\sigma = 1$ and $\sigma = 1.2$ resulting in the values for C_L showing slightly higher values than for the of the non cavitating runs. For the non cavitating runs, i.e. $\sigma = [1.6, 1.4, 1.35]$, the lift coefficient is found to be $C_L = 0.591$ with a root mean square of $RMS = 0.004$. For $\sigma = 1.2$, the lift coefficient is $C_L = 0.603$ with $RMS = 0.014$. The mean cavity length for this run is $l/c = 0.06$ giving a relative error in C_L of about 2.75% with respect to non-cavitating runs at this angle of attack. For $\sigma = 1$, the lift coefficient is found to be $C_L = 0.639$ with $RMS = 0.018$ giving a relative error in C_L of about 9.25% while having a mean cavity length of $l/c = 0.27$. The fact that the lift slightly increases can be explained as follows. The addition of a cavitation bubble at the leading edge on the suction side adds camber to the effective section shape experienced by the flow. This in turn increases the lift of the section.

For $\alpha = 6°$, cavitation occurs for all studied values of σ. For $\sigma = 1.6$ to 1.2, steady sheet cavitation is formed which is reflected in the error bars indicating relatively small *RMS*. For $\sigma = 1$, unsteady cavitation occurs resulting in a significantly larger *RMS*. It can be seen that the values in C_L increase for decreasing σ as long as stable cavitation is obtained. The mean value for the unstable cavitation case shows a large drop in the mean C_L. Since cavitation occurs at $\alpha = 6°$ for all measured cavitation numbers, no relative error can be taken w.r.t. non cavitating CFD results. Without non cavitating results, it cannot be determined with absolute certainty that the lift increases when the section starts to cavitate. However, the trend clearly shows that lift increases for larger cavitation bubbles. Also, the same behaviour is observed for $\alpha = 4°$ so it can be assumed with reasonable certainty that the lift actually starts increasing when the section starts to cavitate. For future research, it would be interesting to know for which values of σ the flow stops cavitating as well as higher values of σ should be tested in order to find the threshold at which cavitation starts. Furthermore, the averages for the unsteady cases should be considered with care since the duration of the simulation might not be long enough to have enough periods in the signal to get an accurate average from the unsteady time series.

For $\alpha = 8°$, all of the simulations show unsteady cavitation and hence have large root mean squares for all values of σ. All mean values for C_L fall between 0.85 and 1.2 although no distinct order is found between the values of σ and their corresponding results. Since all the simulations show unstable behaviour, the mean cavity length are unstable as well and periodically shed cloud cavitation into the flow. As mentioned before, a longer simulation run time would have given time series with enough periods to get a more representative average value for such unstable cavitation cases. For the purpose of the hydrofoil designs at *VPLP Design*, the angle of attack hardly ever need to exceed 6°. Although it is sensible to have an accurate characterisation of a wide range of angles of attack, these high angles of attack are less crucial to characterise to a very high accuracy as for lower angles of attack. Moreover, for future research, it would be interesting to investigate for which value of sigma the flow starts to cavitate and to find the range of σ for which stable sheet cavitation occurs.

Drag Coefficient C_D

In figure 4.39, the CFD results for the drag coefficient polars are shown. The CFD results are plotted for the chosen angles of attack and cavitation numbers. The error bars, line style and markers representation is the same as in previous section. In table 4.12, an overview is given of all the average values of the drag coefficients and its *RMS*.

Table 4.12: CFD results for drag coefficient polars of the NACA-66(mod) for $\sigma = [1, 1.2, 1.35, 1.4, 1.6]$: time average (left) and *RMS* fluctuation(right).

α	1	1.2	1.35	1.4	1.6	α	1	1.2	1.35	1.4	1.6
			σ						σ		
0°	0.0107	0.0107	0.0107	0.0107	0.0107	0°	6.4e-05	6.4e-05	6.4e-05	6.4e-05	6.4e-05
2°	0.0114	0.0114	0.0114	0.0114	0.0114	2°	0.00026	0.00026	0.00026	0.00026	0.00026
4°	0.0123	0.0119	0.0128	0.0128	0.0128	4°	0.00094	0.00108	0.00058	0.00058	0.00058
6°	0.0584	0.0314	0.0226	0.0213	0.0185	6°	0.04164	0.00385	0.00217	0.00178	0.00115
8°	0.1406	0.1345	0.1501	0.0919	0.0723	8°	0.04250	0.04962	0.05021	0.05064	0.02663
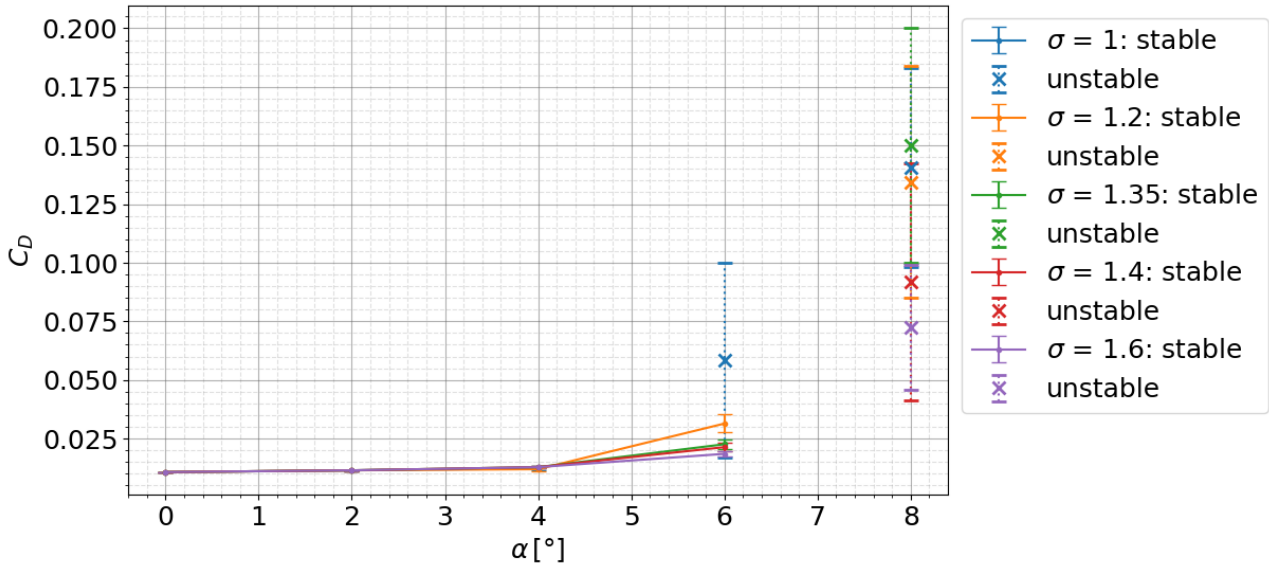
Figure 4.39: Drag coefficient polars from CFD results of the NACA-66(mod) for $\sigma = [1, 1.2, 1.35, 1.4, 1.6]$ with stable and unstable cases.

Again, at low angles of attack, i.e $0°$ and $2°$, the CFD results give the same value for each cavitation number. At $\alpha = 0°$, a drag coefficient of $C_D = 0.0107$ is found with a root mean square of $RMS = 6.4 \times 10^{-5}$. At $\alpha = 2°$, a drag coefficient of $C_L = 0.0114$ is found with a root mean square of $RMS = 0.00026$. For these operating conditions at low angles of attack, no cavitation has been formed yet and thus the drag coefficient has not been altered by a cavitation bubble. The same suggestion for a follow up study can be made as in previous section, i.e to chose operating conditions such that at least one value for sigma is found for which cavitation occurs.

For $\alpha = 4°$, stable sheet cavitation occurs for the CFD results for $\sigma = 1$ and $\sigma = 1.2$ altering the values for C_D w.r.t non cavitating runs. For the non cavitating runs, i.e. $\sigma = [1.6, 1.4, 1.35]$, the drag coefficient is found to be $C_D = 0.0128$ with a root mean square of $RMS = 0.00058$. For $\sigma = 1.2$, the drag coefficient is $C_D = 0.0119$ with $RMS = 0.00108$. The mean cavity length is $l/c = 0.06$ giving a relative error in C_L with respect to the non-cavitating runs of about 7.03%. For $\sigma = 1$, the lift coefficient is found to be $C_L = 0.0123$ with $RMS = 0.00094$ giving a relative error of about 3.91% for a cavity length of $l/c = 0.27$. It is surprising that the drag coefficient slightly decreases. Instead, one would rather expect the formation of a cavitation bubble at leading edge on the suction side the section to increase drag, since the effective thickness of the section increases (at the point where the cavitation bubble forms). Also, the fact that the drag decreases more for a cavity length of $l/c = 0.6$ than for a cavity length of $l/c = 0.27$ raises suspicion, since the opposite is expected. There might be some counter intuitive flow effect which causes this odd observation. Or some numerical error could be the cause of this this. Further study is needed to determine the origin of this observation.

Like mentioned in previous section, at $\alpha = 6°$ steady sheet cavitation is formed for $\sigma = 1.6$ to 1.2 and unsteady cloud cavitation for $\sigma = 1$. This is again reflected in the difference in *RMS* values. Slight increases are to be seen in the mean drag coefficient from $\sigma = 1.6$ to $\sigma = 1.4$ and to $\sigma = 1.35$. A higher increase is seen for $\sigma = 1.2$ as the cavity length l/c also increases significantly. Then as the cavitation becomes unstable, for $\sigma = 1$, the drag coefficient increases by a significant amount. For these results, it can be seen that the drag increases as the cavitation rate increases. This would be as expected since the the cavitation bubble the effective thickness

of the section experienced by the fluid. Also, the significant increase in drag from stable cavitation to unstable cavitation is as expected since the instabilities causes a very unstable flow around the section and in the wake increasing the pressure drag. Since cavitation occurs at $\alpha = 6°$ for all measured cavitation numbers, no relative error can be taken w.r.t. non cavitating CFD results. It would be interesting to know for which values of σ the flow ceases to show cavitation. For future research, values of σ should be tested in order to find the threshold at which cavitation starts.

Like mentioned in previous section, for $\alpha = 8°$ all of the simulations show unsteady cavitation and hence have large root mean squares for all values of σ. The values in mean C_D show a rough increasing trend for decreasing σ except for $\sigma = 1.35$ which has the highest value of mean C_D. The increase in cavitation rate can cause the drag to gradually increase. On the other hand, since the RMS values are so large, this order might well be by Again, a longer simulation run time would have given time series with enough periods to get a more representative average value for such unstable cavitation cases. Regardless, it is clear that all average drag values have increases significantly and the RMS are all very large for these measurements.

Performance L/D

In figure 4.40, the CFD results for the performance is shown as a function of angle of attack. The CFD results are plotted for angles of attack $\alpha = [0, 2, 4, 6, 8]$ and for the cavitation numbers $\sigma = [1.6, 1.4, 1.35, 1.2, 1]$. The error bars, line style and markers representation is the same as in previous sections. In table 4.13, an overview is given of all the average values of the performance and its RMS fluctuation.

Table 4.13: CFD results for performance L/D polars of the NACA-66(mod) for $\sigma = [1, 1.2, 1.35, 1.4, 1.6]$: time average (left) and *RMS* fluctuation(right).

α	1	1.2	1.35	1.4	1.6		α	1	1.2	1.35	1.4	1.6
			σ							σ		
0°	19.05	19.05	19.05	19.05	19.05		0°	0.0023	0.0023	0.0023	0.0023	0.0023
2°	34.92	34.92	34.92	34.92	34.92		2°	0.5438	0.5438	0.5438	0.5438	0.5438
4°	51.97	50.68	46.24	46.24	46.24		4°	2.5046	3.4339	1.7759	1.7759	1.7759
6°	12.61	27.94	36.07	37.56	42.38		6°	5.6181	2.7983	2.8217	2.4769	1.8547
8°	6.18	7.30	7.95	9.96	15.04		8°	0.1120	1.0255	1.1722	2.4131	4.1765
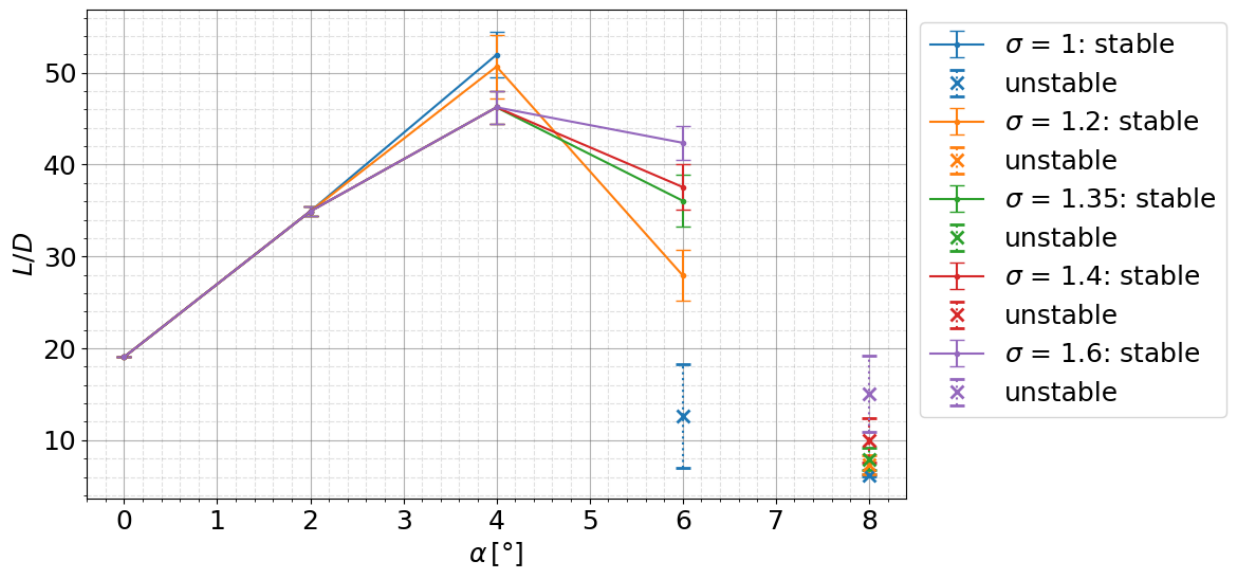
Figure 4.40: L/D as a function of α from CFD results of the NACA-66(mod) for $\sigma = [1, 1.2, 1.35, 1.4, 1.6]$ alongside reference data from Leroux and *xFoil*.

Again, at low angles of attack, i.e 0° and 2°, the performance results give the same value for each cavitation number. At $\alpha = 0°$, a drag coefficient of $L/D = 19.05$ is found with a root mean square of $RMS = 0.0023$. At $\alpha = 2°$, a performance of $L/D = 34.92$ is found with a root mean square fluctuation of $RMS = 0.5438$. As

mentioned in previous sections, for these operating conditions at low angles of attack, no cavitation has been formed yet and thus the performance has not been altered by a cavitation bubble.

For $\alpha = 4°$, stable sheet cavitation occurs for the CFD results for $\sigma = 1$ and $\sigma = 1.2$ altering the performance values w.r.t non cavitating runs. For the non cavitating runs, i.e. $\sigma = [1.6, 1.4, 1.35]$, the performance is found to be $L/D = 46.24$ with a root mean square of $RMS = 1.7759$. For $\sigma = 1.2$, the performance is $L/D = 50.68$ with $RMS = 3.4339$. The mean cavity length is $l/c = 0.06$ giving a relative error in L/D with respect to the non-cavitating runs of about 9.6%. For $\sigma = 1$, the performance is found to be $L/D = 51.97$ with $RMS = 2.5046$ giving a relative error of about 12.39% for a cavity length of $l/c = 0.27$. An increase is found in the performance for the measurements with a developed cavitation bubble. Again, this is a surprising observation. The reason for this is is the small decrease in the drag coefficient for these two measurements. Hence, as discussed in previous section, there might be some counter intuitive flow effect which causes this effect. Or some numerical error could be the cause of this this odd observation. Further study is needed to determine the reason for this.

As mentioned in previous sections, at $\alpha = 6$ steady sheet cavitation is formed for $\sigma = 1.6$ to 1.2 and unsteady cloud cavitation for $\sigma = 1$. The performance has dropped for all measured values of σ since the drag has significantly increased at this angle of attack. The lower the value for σ, the higher the drag (see previous section), the lower the performance. Again, the performance of the unstable case ($\sigma = 1$) is much lower since the pressure drag is significantly higher for cases with cloud cavitation. Since cavitation occurs at $\alpha = 6°$ for all measured cavitation numbers, no relative error can be taken w.r.t. non cavitating CFD results.

As mentioned in previous sections, for $\alpha = 8°$ all of the simulations show unsteady cavitation and hence have large root mean squares for all values of σ. The L/D values all fall between 5 and 16 and decrease as the value of sigma decreases. This corresponds to the increasing trend in the drag coefficient for this angle of attack setting. As mentioned before, a longer simulation run time would have given time series with enough periods to get a more representative average value for such unstable cavitation cases. Regardless, it is clear that all average drag values have increased significantly and the RMS are all very large for these measurements.

The slight increase in performance at $\alpha = 4°$ is also visible when looking at the lift vs drag plot in figure 4.41 where the tangent line of the lift versus drag plot through the origin is steeper for the two data points for $\sigma = 1.2$ and 1 compared to the non cavitating cases.
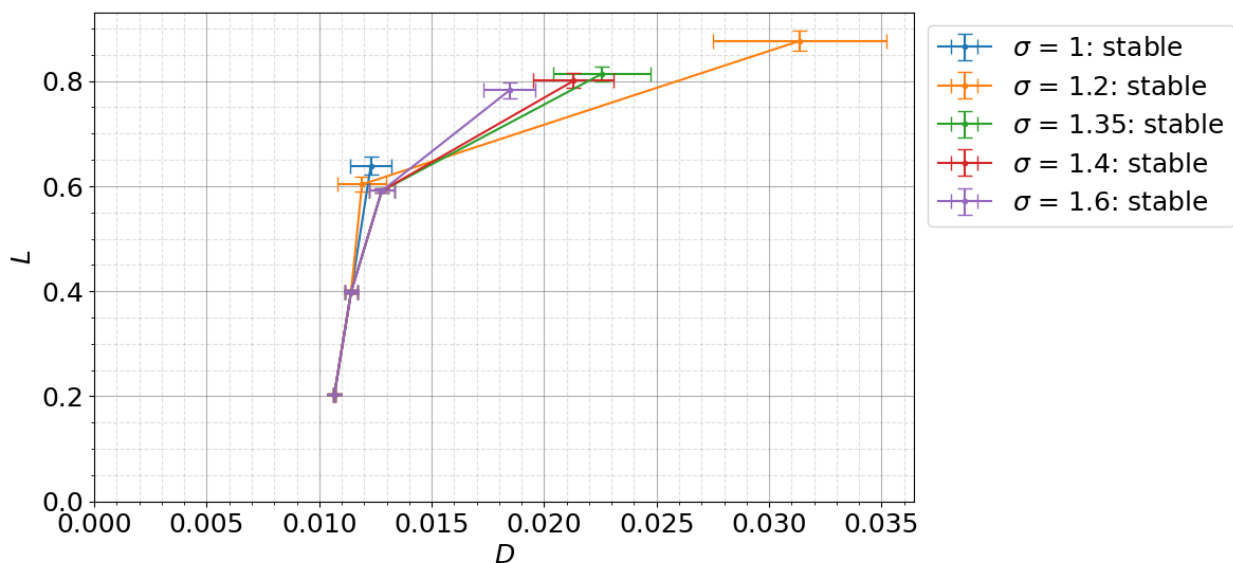
Figure 4.41: L as a function of D from CFD results (stable cases) of the NACA-66(mod) for $\sigma = [1, 1.2, 1.35, 1.4, 1.6]$.

Literature Comparison

In this section, a comparison is made between the results of current study for the highest and lowest measured values of σ ($\sigma = 1$ and $\sigma = 1.6$), as well as experimental results from Leroux et. al. [20] and from potential flow solver *xFoil*. The results from Leroux and *xFoil* are all for non cavitating conditions. The comparison will mainly be focused on the experimental values from Leroux. The *xFoil* data gives an interesting insight about what values are obtained by potential flow w.r.t. to the experimental values and the current CFD studies.

Figure 4.42 shows the CFD results from current study, *xFoil* and Leroux for the lift coefficient. It can be seen that for the low angles of attack, i.e. $0°$ and $2°$, the results from current study underestimate the experimental results from Leroux. These results are expected to be coherent since the CFD results do not show cavitation for these low angles of attack. The validation of the cavitating test case (see section 4.2)has been done with the NACA-66(mod) at $\alpha = 6.5°$ at $Re = 8 \times 10^5$ for multiple values of σ since extensive amounts of reference material was available for these cases. However, no polars are studied during for non cavitating cases with the simulation of the cavitating test cases. Polars for non cavitating cases have been studied during the validation for the non cavitating test case (see section 4.1). Because of this, is seems that the simulation validated for cavitating test cases does not obtain coherent values w.r.t. experimental values for all operating conditions. This seems to be the case for the CFD results for $\alpha = 0°$ and $\alpha = 2°$. The relative error for $\alpha = 0°$ between current CFD results and the experimental result is about 12.43%. For $\alpha = 2°$ this is about 15.28%. For $\alpha = 4°$ the non cavitating cases ($\sigma = 1.6$ up to 1.35) has a relative error with the experimental value of about 17.76%. As discussed in previous section, the rate of cavitating for the cavitating case $\sigma = 1$ increases the lift coefficient by 9.25%. For a similar cavitation rate and cavity length, the lift is likely to increase by similar amounts w.r.t. the experimental values. However, no data is available to verify this claim. For $\alpha = 6°$, no comparison can be made for non cavitating cases since cavitating occurs for all CFD results. For $\sigma = 1.6$ the lift coefficient is $C_L = 0.782$ and the experimental value is $C_L = 0.789$, which is a small difference. Assuming the C_L values of the stable cavitation increases the lift (which is coherent with all observations), the C_L value for non cavitating flow given by the CFD simulation would likely come out a bit lower than the experimental value. As discussed in previous sections, the unstable cases have mean values that are not very accurate and have very large *RMS* values. It does not make much sense to compare them with the experimental values.

Figure 4.42: Lift coefficient polars from CFD results of the NACA-66(mod) for $\sigma = 1$ and $\sigma = 1.6$ as well al well as results from Leroux and xFoil.

In figure 4.43, the drag coefficient results are shown for current CFD study, *xFoil* and experimental data from Leroux. It can be seen that the the CFD data slightly underestimates the experimental results for the non cavitating and stable cavitating cases. For $\alpha = 0°$, the CFD results (for all σ) are underestimating the experimental data by 26.62%. For $\alpha = 2°$, the CFD results (for non cavitating σ) are underestimating the experimental data by 27.38%. Although the CFD results for $\alpha = 4°$ and $\alpha = 6°$ do not contain runs without cavitation, it can be clearly seen that the difference between the stable CFD results and experimental data only gets larger. For the unstable cavitation cases however, the drag becomes much larger than the experimental results.

Figure 4.43: Drag coefficient polars from CFD results of the NACA-66(mod) for $\sigma = 1$ and $\sigma = 1.6$ as well al well as results from Leroux and xFoil.

In figure 4.44, the performance results are plotted for current CFD study, *xFoil* and experimental data from Leroux. Due to the underestimation of the drag coefficient, the performance of in the CFD results are higher than for the experimental results for the stable cases. Like observed with the drag coefficient, this difference is highest for the stable cases at $\alpha = 4°$ and $6°$. The performance in the unstable cases drops below the experimental values since the drag increases above the experimental values.
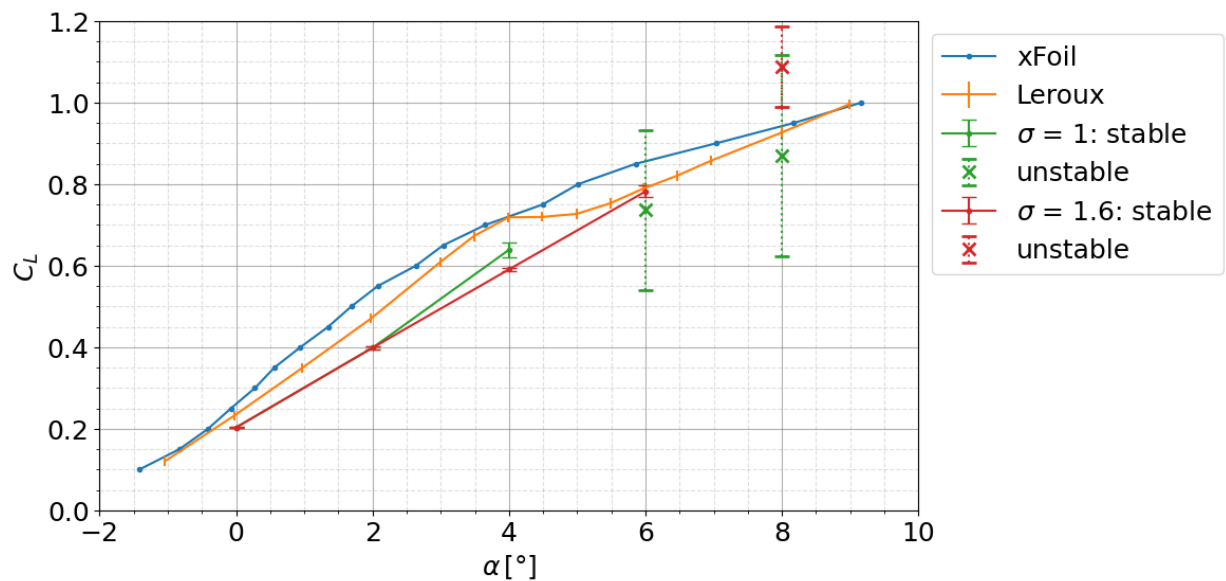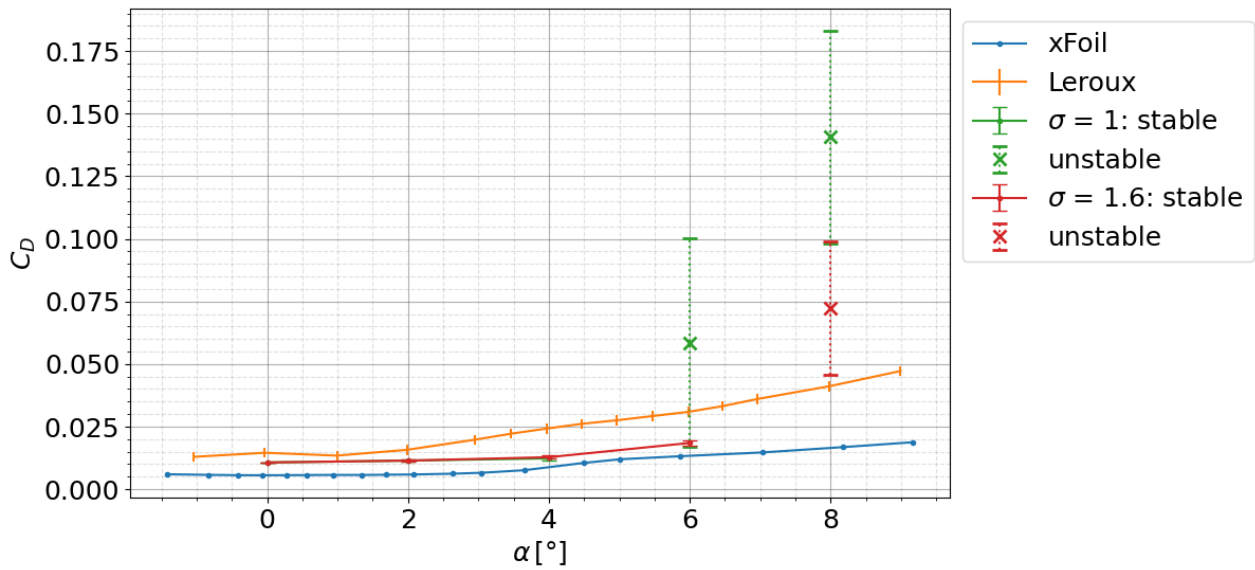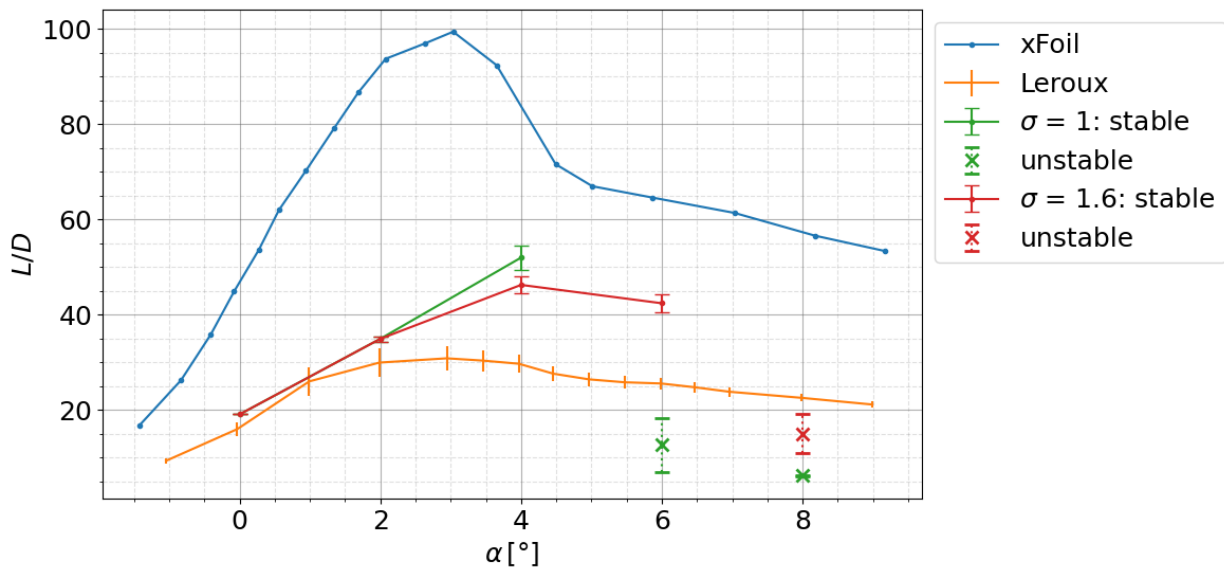

Figure 4.44: L/D polars from CFD results of the NACA-66(mod) for $\sigma = 1$ and $\sigma = 1.6$ as well al well as results from Leroux and xFoil.

5

Conclusion

This work is concluded by reviewing the main research objective and sub questions stated in the introduction. The main objective of this project is stated as follows:

> *Assessment of using CFD to improve analysis and performance prediction of cavitating hydrofoil sections within an industrial setting, compared to current design practice.*

This objective is pursued by using a Schnerr-Sauer cavitation model in a URANS CFD framework which is validated for two dimensional flow around hydrofoil sections. The following research questions have been posed to address the main objective:

- *How does cavitation analysis on a hydrofoil section using CFD with a cavitation model compare to analysis without cavitation model?*
- *How can the transition from stable to unstable cavitation on a hydrofoil section be predicted?*
- *How do the lift and drag coefficient and performance polars of a cavitating hydrofoil section depend on the cavitation number?*
- *What are the limitations of the final setup?*

These research questions are studied with the use of the validated CFD setup with cavitation model. The setup and execution of the simulations are feasible within the computational restrictions of a maximum simulation run time of about 8 hours per simulation on a machine with 20 CPU cores. For the validation, first a non-cavitating test case simulation of a NACA-0012 section is built and validated providing a solid base for the cavitating test case simulation of a modified NACA-66 section. Next, a test case for a cavitating flow around the NACA-66(mod) is set up (section 4.2). For the validation of this test case, the *SST* turbulence model has been chosen and the turbulent viscosity modification has been implemented and studied for which the exponent $n = 2.3$ provided sufficiently accurate results. For unsteady cavitation cases, the cloud cavitation shedding behaviour did not match the reference data. This setup has been used to investigate the sub research questions which are concluded in the following paragraphs.

To evaluate how results from cavitation analysis on a hydrofoil section using a cavitation model compares to results from analysis without a cavitation model a comparison is made with steady cavitation operating conditions on the NACA-66(mod) section. For these conditions, it has been found that cavitation analysis without cavitation model vastly underestimates the length of the cavitation bubble with a relative error of about 83%. As a result the lift and drag coefficient are also underestimated with about 1.1% and 44% respectively, resulting in a relative error in L/D of about 75%. The underestimates in cavitation length, lift, drag and L/D are substantial and should be considered in the design of sections.

Moreover, a comparison is done with the *BPX1* section for unsteady cloud cavitating conditions. For these conditions, the simulation with cavitation model clearly shows cloud cavitation which is not captured in the analysis without cavitation model. This is also in line with the fact that the cavitation bubble length is vastly underestimated in the analysis without cavitation model, since the cavitation regime is found to be dependent on the cavitation bubble length. Meaning that the potentially problematic cloud cavitation regime could easily be

overlooked when performing cavitation analysis without cavitation model.

To study the transition from stable to unstable cavitation, a series of simulations is carried out with the modified NACA-66 geometry for a range of ambient pressures and freestream velocities. The cavitation length l/c and corresponding root mean squared values are studied as a function of the stability parameter $p_s = \frac{\sigma}{2(\alpha - \alpha_0)}$. The different cavitation regimes are reflected in the cavitation lengths and their root mean squared. The study shows that stable sheet cavitation starts around $p_s = 7$ and remains stable up to about $p_s = 4$ with a cavitation length growing up to about $l/c = 0.45$. For $3 < p_s < 4$, the root mean squared of the cavitation length is large indicating unstable cavitation. Cloud cavitation behaviour is confirmed for this range of p_s by looking at simulation visuals. For $p_s < 3$ the cavity length becomes larger than the chord length with relatively small root mean squared values w.r.t the cavity length. As confirmed by the simulation images, the cavitation bubble is stable and encloses the suction side of the section which characterises the supercavitation regime.

These results show that the cavitation regimes are distinguished by ranges in the stability parameter as described above. Hence the stability parameter serves as an indicator for the prediction of the cavitation regimes. Results from studies by Leroux et. al. [20] and Arndt et. al. [4] find similar results for the transition from sheet to cloud cavitation at $p_s = 4$. However, the inception of sheet cavitation for the modified NACA-66 section is found at $p_s = 7$ compared to 8.5 found by Arndt for the NACA-0015 section. Hence, the obtained ranges of p_s do not generally indicate the cavitation regimes as found in current study for all geometries. Furthermore, the lower value for the stability parameter shows that sheet cavitation is retarded to form at higher velocities (or lower ambient pressures) for the NACA-66(mod) and thus can the NACA-66(mod) be considered to be a more optimized geometry compared to the NACA-0015 section.

To see how the lift and drag coefficient and performance polars of cavitating hydrofoil sections depend on the cavitation number, a series of simulations is carried out to obtain lift and drag polars at several rates of cavitation. It is found that lift increases when stable cavitation bubbles form compared to non cavitating cases. Also, the higher the cavitation rate (higher σ, for stable cavitation cases), the larger the cavitation bubble, the larger the increase in lift. As a result, the polars for lower σ show a stronger increase in lift as the angle of attack increases.

On the other hand, the drag coefficient also increases as the cavitation rate increases and cavitation bubbles grow. Again, the drag increase is stronger for larger cavitation bubbles, hence the increase in drag as a function of angle of attack is larger as the cavitation number decreases.

The performance, i.e. lift over drag, shows an increase at $\alpha = 4°$ for $\sigma = 1.2$ and a further increase for $\sigma = 1$. At this angle of attack, the cavitation bubbles are sufficiently small such that the increase in lift is larger than the increase in drag. At higher angles of attack however, drag becomes proportionally larger which makes the performance decrease for lower values of σ.

These findings only apply to the stable cavitation cases, as for the unstable ones, the results are inconclusive due to incomplete data. More on this in the next section on follow up studies.

Furthermore, the findings should be taken with care since the polars (for non-cavitating cases) at the lower angles of attack are not coherent with the reference values. However, the effect of the change in cavitation number on the general behaviour in lift and drag is likely to be correct regardless of the specific values.

In the validation phase of this project, the results have shown to be coherent with reference values for the stable cavitation cases. Also, the transition point from stable to unstable cavitation found in current study is coherent with reference data. However, for the unsteady cavitation cases, the results of the shedding behaviour does not match the reference values. The cavitation bubble shedding in the cloud cavitation regime can be an important source of vibrations. Capturing the shedding frequency of cloud cavitation would help in predicting vibrations and its resulting loads. Therefore, this shortcoming is considered to be the main limitation of the current setup. In other words, the current CFD setup developed in this project is able to predict stable cavitation cases and theirs loads as well as predict the transition from stable to unstable cavitation within reasonable accuracy. The setup is not able to predict unsteady cavitation shedding behaviour within reasonable accuracy. This limitation is further addressed in the following section.

Outlook

For the design process of *VPLP Design*, the CFD setup developed in this project can be useful when several foil section candidates are designed. These sections can be analysed and compared for a range of conditions to compare the sections for when cavitation is induced, how the cavitation bubble and loads develop with respect to the conditions and when unstable cavitation occurs. Still, for such a comparison several extensive series of simulations should be executed which is not feasible at the moment with the current computational resources at *VPLP*. For such a study to be feasible, the computational capabilities need to be enhanced first.

A follow-up step in extension of current project would be to make a 3D setup so that full three dimensional hydrofoil geometries can be analysed and compared in a similar way.

The ultimate long term goal would be to optimize three dimensional hydrofoils geometries to delay the inception of cavitation and delay the transition from stable to unstable cavitation as much as possible. For this, an optimization framework like OpenMDAO [12] can be used to serve as a computing platform for the geometry optimization.

As mentioned in previous section, the main limitation of the setup is the fact that the shedding behaviour of cloud cavitation is not well captured. To find the reason behind this inconsistency, the following issues can be discussed. The general cavitation behaviour in the CFD simulation is dependent of several factors. The choice in turbulence model has an important influence on the cavitation behaviour. This has been studied in the validation part of current study, although choosing a suited turbulence model was not sufficient for the validation of the simulation setup. For this, a modification in another important factor had to be introduced; the turbulent viscosity exponent n. The modification in this parameter eventually lead to the validation of the setup. However, the chosen value of the exponent n is not based on any measurable physical quantity and is thus chosen to fit the reference data. Finding such a sweet spot in a parameter is a tricky thing to do and impacts the robustness of the simulation setup as it does not guarantee the desired behaviour for a different case. Another important factor in the cavitation behaviour is, of course, the cavitation model used in the simulation. In current study, only the Schnerr-Sauer cavitation model has been used. However, other simplified cavitation models are known (although not usable in Star-CCM+), as well as the more computationally expensive full Rayleigh-Plesset model. A combination of the right cavitation model, turbulent viscosity exponent and turbulence model might be the answer to validating the cloud cavitation behaviour.

Another improvement to current study would be to make a three dimensional CFD simulation. As mentioned in the methodology section, cavitation and turbulence are intrinsically three dimensional phenomena. Hence, choosing for a two dimensional computational domain may cause some flow effects not to be included and therefore mismatch the results with the reference data. For this however, much more computational resources are needed as a three dimensional computational domain increases the number of mesh elements by several orders of magnitude.

Furthermore, Large Eddy Simulation (LES) or Detached Eddy Simulations (DES) could be used instead of URANS. These simulations are able to resolve unsteady turbulent flow phenomena with higher accuracy. Hence, the important unsteady flow and turbulent structures in cloud cavitation would be reproduced more accurately, making LES and/or DES a good candidate to be used for cloud cavitation. However, this again comes at a computational cost.

For the study on the polars dependency on the cavitation number, several remarks can be made. First, although the results were sufficient to give some insight on the effect of the cavitation rate on the polars, a full validation of the polars for non-cavitating conditions should be made in order for such a study to be fully conclusive. Also, in order to get detailed polar data, the increments in α should be smaller, ideally at $0.5°$ or at least $1.0°$. Furthermore, it would be insightful if the studied sigmas are chosen such that for each angle of attack, at least one non-cavitating, one stable cavitating and one unstable cavitating case would be simulated. This would allow for the polar quantities for each cavitating case to be compared to the non-cavitating case at each angle of attack and see what the gain or loss in lift or drag would be. In current study, this is only done for a few values of α. The addition unstable cavitating cases for each angle of attack would give a broader overview of the range of cavitation regimes at each angle of attack. This brings up another point, order to have a sensible lift or polar measurement for unstable cavitation cases, the simulation runtime should be long enough in order to capture the average value of the measured polar quantity. In order for these remarks to be implemented in a future study, the values for σ have to be picket out carefully. Furthermore, much more computational resources are needed as

many more simulations should be run for the smaller increments in α, additional values of σ and for the longer simulation times for the unsteady cases.

References

[1] J Acosta. "A Note on Partial Caviation of Flat Plate Hydrofoils". en. *Office of Naval Research Department of the Navy* Contract N6onr-244, Task Order 11.Report No. E - 19.9 (Oct. 1955), p. 13. URL: `https://resolver.caltech.edu/CaltechAUTHORS:AC0hydrolabE19-9`.

[2] Byoung-Kwon Ahn, Tae Kwon Lee, Hyoung Kim, and Chang-Sup Lee. "Experimental investigation of supercavitating flows". *International Journal of Naval Architecture and Ocean Engineering* 4 (June 2012), pp. 123–131. DOI: `10.3744/JNAOE.2012.4.2.123`.

[3] Edward Alyanak, Ramana Grandhi, and Ravi Penmetsa. "Optimum design of a supercavitating torpedo considering overall size, shape, and structural configuration". en. *International Journal of Solids and Structures* 43.3 (Feb. 2006), pp. 642–657. ISSN: 0020-7683. DOI: `10.1016/j.ijsolstr.2005.05.040`. URL: `https://www.sciencedirect.com/science/article/pii/S0020768305003057`.

[4] R. Arndt, C. C. S. Song, M. Kjeldsen, J. He, and A. Keller. "Instability of partial cavitation: A numerical/-experimental approach". en. In: *23rd Symposium on Naval Hydrodynamics*. P2000-14 Proceedings. Val de Reuil, France: National Academy Press, Washington DC, 2000. URL: `https://repository.tudelft.nl/islandora/object/uuid%3A16269ef2-6909-496b-a571-eb43870162a1`.

[5] J. Baltazar and J. Campos. *An Iteratively Coupled Solution Method for Partial and Super-Cavitation Prediction on Marine Propellers Using BEM*. Marine Environment and Technology Center (MARETEC), Department of Mechanical Engineering Instituto Superior Tťecnico (IST). Technical University of Lisbon, Portugal, Oct. 2012. URL: `https://www.researchgate.net/profile/J-Baltazar-2/publication/346443385_An_Iteratively_Coupled_Solution_Method_for_Partial_and_Super-Cavitation_Prediction_on_Marine_Propellers_Using_BEM/links/5fc23cce928 51c933f6ac78b/An-Iteratively-Coupled-Solution-Method-for-Partial-and-Super-Cavitation-Prediction-on-Marine-Propellers-Using-BEM.pdf`.

[6] J. Baltazar and J. F. D. Campos. "Prediction of Unsteady Sheet Cavitation on Marine Current Turbines with a Boundary Element Method". In: *Proceedings of the 6th International Conference on Mechanics and Materials in Design*. 2015. URL: `https://www.semanticscholar.org/paper/PREDICTION-OF-UNSTEADY-SHEET-CAVITATION-ON-MARINE-A-Baltazar-Campos/2db8898a57a086d2181facc6a 7fc39caa0d93809`.

[7] J. Baltazar and J. a. C. Falcão de Campos. "Prediction of Sheet Cavitation on Marine Current Turbines With a Boundary Element Method". en. In: American Society of Mechanical Engineers Digital Collection, Aug. 2013, pp. 249–257. DOI: `10.1115/OMAE2012-83331`. URL: `https://asmedigitalcollection.asme.org/OMAE/proceedings-abstract/OMAE2012/44946/249/270279`.

[8] Hannah C Buckland, Ian Masters, James AC Orme, and Tim Baker. "Cavitation inception and simulation in blade element momentum theory for modelling tidal stream turbines". en. *Proceedings of the Institution of Mechanical Engineers, Part A: Journal of Power and Energy* 227.4 (June 2013). Publisher: IMECHE, pp. 479–485. ISSN: 0957-6509. DOI: `10.1177/0957650913477093`. URL: `https://doi.org/10.1177/0957650913477093`.

[9] O. Coutier-Delgosha, Regiane Fortes Patella, and Jean-Luc Reboud. "Evaluation of the Turbulence Model Influence on the Numerical Simulations of Unsteady Cavitation". In: *Proceedings of 2001 ASME FEDSM*. Vol. 125. Journal of Fluids Engineering, June 2001.

[10] J.P. Franc and J.M. Michel. *Fundamentals of Cavitation*. Fluid Mechanics and Its Applications. Springer Netherlands, 2006. ISBN: 978-1-4020-2233-3. URL: `https://books.google.fr/books?id=QJOQYa%5C_oo24C`.

[11] K. Graf, A. V. Hoeve, and S. Watin. "Comparison of full 3D-RANS simulations with 2D-RANS/lifting line method calculations for the flow analysis of rigid wings for high performance multihulls". en. *Ocean Engineering, Volume 90, 1 November 2014, pp. 49-61.* (2014). URL: `https://repository.tudelft.nl/islandora/object/uuid%3Ab7f4cd55-81d7-4436-9b32-f0c65ac26865`.

[12] Justin S. Gray, John T. Hwang, Joaquim R. R. A. Martins, Kenneth T. Moore, and Bret A. Naylor. "OpenM-DAO: an open-source framework for multidisciplinary design, analysis, and optimization". en. *Structural and Multidisciplinary Optimization* 59.4 (Apr. 2019), pp. 1075–1104. ISSN: 1615-147X, 1615-1488. DOI: 10.1007/s00158-019-02211-z. URL: http://link.springer.com/10.1007/s00158-019-02211-z.

[13] Stefan Hickel. "Powerpoint 05 RANS". *Computational Fluid Dynamics for Aerospace Engineers* (2020).

[14] C. W Hirt and B. D Nichols. "Volume of fluid (VOF) method for the dynamics of free boundaries". en. *Journal of Computational Physics* 39.1 (Jan. 1981), pp. 201–225. ISSN: 0021-9991. DOI: 10.1016/0021-9991(81)90145-5. URL: https://www.sciencedirect.com/science/article/pii/0021999181901455.

[15] W. P Jones and B. E Launder. "The prediction of laminarization with a two-equation model of turbulence". en. *International Journal of Heat and Mass Transfer* 15.2 (Feb. 1972), pp. 301–314. ISSN: 0017-9310. DOI: 10.1016/0017-9310(72)90076-2. URL: https://www.sciencedirect.com/science/article/pii/0017931072900762.

[16] Suraj R. Kashyap and Rajeev K. Jaiman. *Unsteady cavitation dynamics and frequency lock-in of a freely vibrating hydrofoil at high Reynolds number*. 2022. DOI: 10.48550/ARXIV.2202.11227. URL: https://arxiv.org/abs/2202.11227.

[17] Joseph Katz and Allen Plotkin. *Low-Speed Aerodynamics*. 2nd ed. Cambridge University Press, Feb. 2001. ISBN: 978-0-521-66552-0 978-0-521-66219-2 978-0-511-81032-9. DOI: 10.1017/CBO9780511810329. URL: https://www.cambridge.org/core/product/identifier/9780511810329/type/book.

[18] Morten Kjeldsen, Roger Arndt, and Mark Effertz. "Spectral Characteristics of Sheet/Cloud Cavitation". *Journal of Fluids Engineering-transactions of The Asme - J FLUID ENG* 122 (Sept. 2000). DOI: 10.1115/1.1287854.

[19] Charles L. Ladson. *Effects of independent variation of Mach and Reynolds numbers on the low-speed aerodynamic characteristics of the NACA 0012 airfoil section*. Tech. rep. L-16472. NTRS Author Affiliations: NASA Langley Research Center NTRS Document ID: 19880019495 NTRS Research Center: Legacy CDMS (CDMS). Oct. 1988. URL: https://ntrs.nasa.gov/citations/19880019495.

[20] Jean-Baptiste Leroux, Jacques Andreť Astolfi, and Jean Yves Billard. "An Experimental Study of Unsteady Partial Cavitation". *Journal of Fluids Engineering* 126.1 (Feb. 2004). _eprint: https://asmedigitalcollection.asme.org/fluids pdf/126/1/94/5901913/94_1.pdf, pp. 94–101. ISSN: 0098-2202. DOI: 10.1115/1.1627835. URL: https://doi.org/10.1115/1.1627835.

[21] Jean-Baptiste Leroux, Olivier Coutier-Delgosha, and Jacques André Astolfi. "A joint experimental and numerical study of mechanisms associated to instability of partial cavitation on two-dimensional hydrofoil". en. *Physics of Fluids* 17.5 (May 2005), p. 052101. ISSN: 1070-6631, 1089-7666. DOI: 10.1063/1.1865692. URL: http://aip.scitation.org/doi/10.1063/1.1865692.

[22] Ziru Li and Tom van Terwisga. "On the capability of multiphase RANS code to predict cavitation erosion". en. *Proceedings of the Second International Symposium on Marine Propulsors, smp'11, Hamburg, Germany.* (2011). URL: https://repository.tudelft.nl/islandora/object/uuid%3A1e4ec289-ecd0-4b71-bcce-71e19550b201.

[23] Laura Marimon Giovannetti, Ali Farousi, Fabian Ebbesson, Alois Thollot, Alex Shiri, and Arash Eslamdoost. "Fluid-Structure Interaction of a Foiling Craft". en. *Journal of Marine Science and Engineering* 10.3 (Mar. 2022). Number: 3 Publisher: Multidisciplinary Digital Publishing Institute, p. 372. ISSN: 2077-1312. DOI: 10.3390/jmse10030372. URL: https://www.mdpi.com/2077-1312/10/3/372.

[24] Themistoklis Melissaris. "Simulation of Cavitation and Surface Erosion on Marine Propellers". Ship Hydromechanics and Structures. Phd Dissertation. Tu Delft, Jan. 2023. URL: https://repository.tudelft.nl/islandora/object/uuid%3A68eaa272-e222-4216-aba8-42c86fdf12fb?collection=research.

[25] F. R. Menter. "Two-equation eddy-viscosity turbulence models for engineering applications". en. *AIAA Journal* 32.8 (Aug. 1994), pp. 1598–1605. ISSN: 0001-1452, 1533-385X. DOI: 10.2514/3.12149. URL: https://arc.aiaa.org/doi/10.2514/3.12149.

[26] John Meyer. *Ships That Fly*. Hydrofoil Technology, Inc, 1990. URL: https://themeyers.org/ShipsThatFly/.

[27]   Samir Muzaferija, Dimitrios Papoulias, and Milovan Peric. "VOF Simulations Of Hydrodynamic Cavita-
       tion Using The Asymptotic And Classical Rayleigh-Plesset Models". In: *Fifth International Symposium
       on Marine Propulsion*. Espoo, Finland, June 2017.

[28]   U. S. Navy. *Cavitating propeller in a water tunnel experiment at the David Taylor Model Basin.* 1940.
       URL: https://commons.wikimedia.org/wiki/File:Cavitating-prop.jpg.

[29]   M S Plesset and A Prosperetti. "Bubble Dynamics and Cavitation". *Annual Review of Fluid Mechanics*
       9.1 (1977). _eprint: https://doi.org/10.1146/annurev.fl.09.010177.001045, pp. 145–185. DOI: 10.1146/
       annurev.fl.09.010177.001045. URL: https://doi.org/10.1146/annurev.fl.09.010177.
       001045.

[30]   Matthieu Sacher, Mathieu Durand, Élisa Berrini, Frédéric Hauville, Régis Duvigneau, Olivier Le Maître,
       and Jacques-André Astolfi. "Flexible hydrofoil optimization for the 35th America's Cup with constrained
       EGO method". en. *Ocean Engineering* 157 (June 2018), pp. 62–72. ISSN: 00298018. DOI: 10.1016/j.
       oceaneng.2018.03.047. URL: https://linkinghub.elsevier.com/retrieve/pii/S002980181
       8303123.

[31]   Michael S Selig. *UIUC airfoil data site*. Urbana, Ill. : Department of Aeronautical and Astronautical
       Engineering University of Illinois at Urbana-Champaign, 1996-, 1996. URL: https://search.library.
       wisc.edu/catalog/999919007002121.

[32]   Jung Hee Seo and Sanjiva Lele. "Numerical investigation of cloud cavitation and cavitation noise on a
       hydrofoil section" (May 2011). DOI: https://hdl.handle.net/2027.42/84259.

[33]   Konstantina Sfakianaki and George Tzabiras. "Development of forces around a hydrofoil appendage of a
       sailing boat". In: Sept. 2015, pp. 193–202. ISBN: 978-1-138-02887-6. DOI: 10.1201/b18855-27.

[34]   Siemens Digital Industries Software. "Simcenter \uppercaseSTAR-CCM+ User Guide, version 2021.1".
       In: *Scale-Resolving Simulations*. Siemens, 2021, pp. 3067–3070. URL: https://docs.sw.siemens.
       com/documentation/external/PL20200227072959152/en-US/userManual/userGuide/html/
       index.html#page/STARCCMP%2FGUID-C6C44B9E-0757-47B9-B726-6D459760EDD7.html%23.

[35]   Siemens Digital Industries Software. "Simcenter \uppercaseSTAR-CCM+ User Guide, version 2021.1". In:
       Detached Eddy Simulation (DES). Siemens, 2021, pp. 3067–3070. URL: https://docs.sw.siemens.
       com/documentation/external/PL20200227072959152/en-US/userManual/userGuide/html/
       index.html#page/STARCCMP%2FGUID-34DAAB4B-8CA1-44A3-9238-E9A122E66E61.html%23.

[36]   Siemens Digital Industries Software. "Simcenter \uppercaseSTAR-CCM+ User Guide, version 2021.1".
       In: *Detached Eddy Simulation (DES) Theory*. Siemens, 2021, pp. 3067–3070. URL: https://docs.sw.
       siemens.com/documentation/external/PL20200227072959152/en-US/userManual/userGu
       ide/html/index.html#page/STARCCMP%2FGUID-53D8E311-F1AB-429D-BAAD-B3B9A9A2979F.
       html%23.

[37]   Siemens Digital Industries Software. "Simcenter \uppercaseSTAR-CCM+ User Guide, version 2021.1".
       In: *Volume of Fluid Method*. Siemens, 2021, pp. 3067–3070. URL: https://docs.sw.siemens.com/d
       ocumentation/external/PL20200227072959152/en-US/userManual/userGuide/html/index.
       html#page/STARCCMP/GUID-11CD4B05-2045-4FFB-9BCA-F31DD3C59599.html#wwID0EN26ED.

[38]   Tan-Dung Tran, Bernd Nennemann, Thi Vu, and Francois Guibault. "Investigation of Cavitation Models
       for Steady and Unsteady Cavitating Flow Simulation". *International Journal of Fluid Machinery and
       Systems* 8 (Oct. 2015), pp. 240–253. DOI: 10.5293/IJFMS.2015.8.4.240.

[39]   M. P. Tulin and David W. Taylor Model Basin. *Steady two-dimensional cavity flows about slender bodies*.
       Report, 834. Pages: 1-40. Washington, D.C: Navy Dept, 1953. DOI: 10.5962/bhl.title.47277. URL:
       https://www.biodiversitylibrary.org/bibliography/47277.

[40]   RAY VELLINGA. *Hydrofoil-Development-and-Applications - THE INTERNATIONAL HYDROFOIL SO-
       CIETY - ESTABLISHED 1970*. en-US. Dec. 2017. URL: https://foils.org/hydrofoil-developme
       nt-and-applications/.

[41]   Satoshi Watanabe, Yoshinobu Tsujimoto, and Akinori Furukawa. "Theoretical Analysis of Transitional
       and Partial Cavity Instabilities". *Journal of Fluids Engineering* 123.3 (Mar. 2001), pp. 692–697. ISSN:
       0098-2202. DOI: 10.1115/1.1378295. URL: https://doi.org/10.1115/1.1378295.

[42] E. A. Weitendorf. *On the History of Propeller Cavitation and Cavitation Tunnels*. conference. California Institute of Technology, Pasadena, CA USA, Jan. 2001. URL: https://resolver.caltech.edu/CAV2001:sessionB9.001.

[43] Wu. "A Free Streamline Theory for TwoDimensional Fully Cavitated Hydrofoils". *Journal of Mathematics and Physics* (1956). URL: https://onlinelibrary.wiley.com/doi/10.1002/sapm1956351236.

[44] Q. Wu, G. Y. Wang, and B. Huang. "Physical and numerical investigation of the flow induced vibration of the hydrofoil". *IOP Conference Series: Earth and Environmental Science* 49 (Nov. 2016). Publisher: IOP Publishing, p. 072002. DOI: 10.1088/1755-1315/49/7/072002. URL: https://doi.org/10.1088/1755-1315/49/7/072002.

[45] Qin Wu, Yana Wang, and Guoyu Wang. "Experimental investigation of cavitating flow-induced vibration of hydrofoils". *Ocean Engineering* 144 (2017), pp. 50–60. ISSN: 0029-8018. DOI: https://doi.org/10.1016/j.oceaneng.2017.08.005. URL: https://www.sciencedirect.com/science/article/pii/S0029801817304584.

[46] Lingjiu Zhou and Zhengwei Wang. "Numerical Simulation of Cavitation Around a Hydrofoil and Evaluation of a RNG k-epsilon Model". en. *Journal of Fluids Engineering* 130.1 (Jan. 2008), p. 011302. ISSN: 0098-2202, 1528-901X. DOI: 10.1115/1.2816009. URL: https://asmedigitalcollection.asme.org/fluidsengineering/article/doi/10.1115/1.2816009/411966/Numerical-Simulation-of-Cavitation-Around-a.